Copyright Warning & Restrictions

The copyright law of the United States (Title 17, United States Code) governs the making of photocopies or other reproductions of copyrighted material.

Under certain conditions specified in the law, libraries and archives are authorized to furnish a photocopy or other reproduction. One of these specified conditions is that the photocopy or reproduction is not to be "used for any purpose other than private study, scholarship, or research." If a, user makes a request for, or later uses, a photocopy or reproduction for purposes in excess of "fair use" that user may be liable for copyright infringement,

This institution reserves the right to refuse to accept a copying order if, in its judgment, fulfillment of the order would involve violation of copyright law.

Please Note: The author retains the copyright while the New Jersey Institute of Technology reserves the right to distribute this thesis or dissertation

Printing note: If you do not wish to print this page, then select
"Pages from: first page # to: last page #" on the print dialog screen

The Van Houten library has removed some of the personal information and all signatures from the approval page and biographical sketches of theses and dissertations in order to protect the identity of NJIT graduates and faculty.

ABSTRACT

SOME CONTRIBUTIONS ON MIMO RADAR

by
Nikolaus Lehmann

Motivated by recent advances in Multiple Input Multiple Output (MIMO) wireless communications, this dissertation aims at exploring the potential of MIMO approaches in the radar context. In communications, MIMO systems combat the fading effects of the multi-path channel with spatial diversity. Further, the scattering environment can be used by such systems to achieve spatial multiplexing. In radar, a complex target consisting of several scatterers takes the place of the multi-path channel of the communication problem. A target's radar cross section (RCS), which determines the amount of returned power, greatly varies with the considered aspect. Those variations significantly impair the detection and estimation performance of conventional radar employing closely spaced arrays on transmit and receive sides. In contrast, by widely separating the transmit and receive elements, MIMO radar systems observe a target simultaneously from different aspects resulting in spatial diversity. This diversity overcomes the fluctuations in received power. Similar to the multiplexing gain in communications, the simultaneous observation of a target from several perspectives enables resolving its features with an accuracy beyond the one supported by the bandwidth. The dissertation studies the MIMO concept in radar in the following manner. First, angle of arrival estimation is explored for a system applying transmit diversity on the transmit side. Due to the target's RCS fluctuations, the notion of ergodic and outage Cramer Rao bounds is introduced. Both bounds are compared with simulation results revealing the diversity potentials of MIMO radar. Afterwards, the detection of targets in white Gaussian noise is discussed including geometric considerations due to the wide separation between the system elements. The detection performance of MIMO radar is then compared to the one achieved by conventional phased array radar systems. The discussion is extended to include returns from homogeneous clutter. A

Doppler processing based moving target detector for MIMO radar is developed in this context. Based on this detector, the moving target detection capabilities of MIMO radar are evaluated and compared to the ones of phased array and multi-static radar systems. It is shown, that MIMO radar is capable of reliably detecting targets moving in an arbitrary direction. The advantage of using several transmitters is illustrated and the constant false alarm rate (CFAR) property of adaptive MIMO moving target detectors is demonstrated. Finally, the high resolution capabilities of MIMO radar are explored. As noted above, the several individual scatterers constituting a target result in its fluctuating RCS. The high resolution mode is aimed at resolving those scatterers. With Cramer Rao bounds and simulation results, it is explored how observing a single isotropic scatterer from several aspects enhances the accuracy of estimating the location of this scatterer. In this context a new, two-dimensional ambiguity function is introduced. This ambiguity function is used to illustrate that several scatterers can be resolved within a conventional resolution cell defined by the bandwidth. The effect of different system parameters on this ambiguity function is discussed.

SOME CONTRIBUTIONS ON MIMO RADAR

by
Nikolaus Lehmann

A Dissertation
Submitted to the Faculty of
New Jersey Institute of Technology
in Partial Fulfillment of the Requirements for the Degree of
Doctor of Philosophy in Electrical Engineering

Department of Electrical and Computer Engineering

January 2007

Copyright © 2007 by Nikolaus Lehmann

ALL RIGHTS RESERVED

APPROVAL PAGE

SOME CONTRIBUTIONS ON MIMO RADAR

Nikolaus Lehmann

Dr. Alexander M. Haimovich, Dissertation Advisor — Date
Professor, Department of Electrical and Computer Engineering, NJIT

Dr. Yeheskel Bar-Ness, Committee Member — Date
Distinguished Professor, Department of Electrical and Computer Engineering, NJIT

Dr. Ali Abdi, Committee Member — Date
Assistant Professor, Department of Electrical and Computer Engineering, NJIT

Dr. Rick S. Blum, Committee Member — Date
Professor, Department of Electrical and Computer Engineering, Lehigh University

Dr. Leonard J. Cimini, Jr., Committee Member — Date
Professor, Department of Electrical and Computer Engineering, University of Delaware

BIOGRAPHICAL SKETCH

Author: Nikolaus Lehmann

Degree: Doctor of Philosophy

Date: January 2007

Undergraduate and Graduate Education:

- Doctor of Philosophy in Electrical Engineering,
  New Jersey Institute of Technology, Newark, NJ, 2007
- Diplom Ingenieur in Electrical Engineering,
  Universität Karlsruhe, Karlsruhe, Germany, 2003

Major: Electrical Engineering

Presentations and Publications:

N. H. Lehmann, A.M. Haimovich, R.S. Blum, L. J. Cimini, "High Resolution Capabilities of MIMO-Radar", to appear, *Asilomar Conference on Signals, Systems and Computers 2006*, October 2006.

N. H. Lehmann, A.M. Haimovich, R.S. Blum, L. J. Cimini, "Comparison between MIMO, Multi-Static and Phased Array Radar Systems for Moving Target Detection in Homogenous Clutter", to be submitted, *IEE Proceedings Radar, Sonar and Navigation*, 2006.

N. H. Lehmann, A.M. Haimovich, R.S. Blum, L. J. Cimini, R. Valenzuela "MIMO-Radar Application to Moving Target Detection in Homogenous Clutter" *Adaptive Sensor Array Processing Workshop 2006 (ASAP 2006)*, June 2006.

N. H. Lehmann, E. Fishler, A.M. Haimovich, R.S. Blum, D. Chizhik, L. J. Cimini, R. Valenzuela "Evaluation of Transmit Diversity in MIMO-radar Direction Finding", to appear, *IEEE Transaction on Signal Processing*, 2006.

N. H. Lehmann, A.M. Haimovich, "The Power Spectral Density of a Time Hopping UWB Signal: A Survey," *in Proceedings of IEEE 2003 Conference on Ultra Wideband Systems and Technology (UWBST)*, November 2003.

N. H. Lehmann, A.M. Haimovich, “New Approach to control the Power Spectral Density of a Time Hopping UWB Signal,” *in Proceedings of Conference on Information Sciences and Sytems (CISS)*, March 2003.

To Constanza, Gwendoline,
Katinka, and Lutz.

ACKNOWLEDGMENT

First, I would like to express my deepest gratitude to my advisor, Dr. Alexander Haimovich. He made it possible four years ago, that I could come to NJIT as research scholar during my diploma thesis in 2002, and that I could return to NJIT as a PhD candidate after graduating in Germany in 2003. Throughout my diploma thesis and my doctoral studies he guided and motivated me with an incredible dedication. I would also like to thank Dr. Rick Blum and Dr. Len Cimini for serving on my dissertation committee and working with Dr. Haimovich and me on MIMO–radar. One result of this joint research effort is this dissertation. I would like to extend my special thanks to Dr. Yeheskel Bar-Ness for heading CCSPR, which is the research center I spend the last four years at, and for serving on my committee. I am also very grateful to Dr. Ali Abdi for serving on my committee.

Further thanks go to Dr. Ronald Kane, the staff of the graduate studies office of NJIT, Mr. Jeffrey Grundy, and the staff of the office for international students and faculty for their advice, help and support with administrative matters during my PhD studies. Special thanks go to Dr. Kane and the Ross Memorial Fellowship fund for the financial support during my doctoral studies.

Ms. Marlene Toeroek deserves a very special acknowledgment from all who work at CCSPR and, in particular, me. She is the heart and soul of life at this research center.

Finally, I would like to thank all my colleagues at CCSPR for all the great and unforgettable moments we shared. Especially, I would like to thank Dr. Osvaldo Simeone and Dr. Jordi Diaz for their support during the last year.

TABLE OF CONTENTS

TABLE OF CONTENTS
(Continued)

Chapter **Page**

LIST OF TABLES

LIST OF FIGURES

LIST OF FIGURES
(Continued)

Figure **Page**

CHAPTER 1

INTRODUCTION

The introduction of the Multiple Input Multiple Output (MIMO) concept revolutionized wireless communications over the last decade, [1, 2]. MIMO communication systems overcome the effect of fading in the wireless channel by transmitting redundant streams of data from several decorrelated transmitters and or employing several receive elements [3]. For independent fading paths, the receiver of a MIMO system enjoys the fact that the average (over all information streams) signal to noise ratio (SNR) is more or less constant, as the number of paths increases, whereas in conventional systems, which transmit and receive all signals over a single path, the received SNR varies considerably. Commonly this is referred to as *diversity gain*.

Further, the rich scattering environment can be used by such systems to achieve to transmit information via orthogonal paths. This is equivalent to additional bandwidth and referred to as *multiplexing gain*. In [4] a concise, but extensive treatment is given to both kind of gains.

The success of the MIMO concept in communications partly served as motivation to apply this concept to the radar problem. In radar, the complex targets consisting of several scatterers take the place of the multi-path channel. A target's radar cross section (RCS), which determines the amount of returned power, greatly varies with the considered aspect, [5]. Both experimental measurements and modeling results demonstrate that variations in reflected power of 20 dB or more can occur by changing the target aspect by as little as one milliradian. Those variations significantly impair the detection and estimation performance of conventional radar. The similarity between these RCS variations and what is commonly called the fading channel in communications is obvious.

Figure 1.1 shows a typical monostatic RCS of a radar target in dependency of the target aspect. The returned power has been normalized to a unit mean. In [6] it is shown that already five equal gain scatterers constituting a target lead to a Rayleigh fading effect due to their different positions.

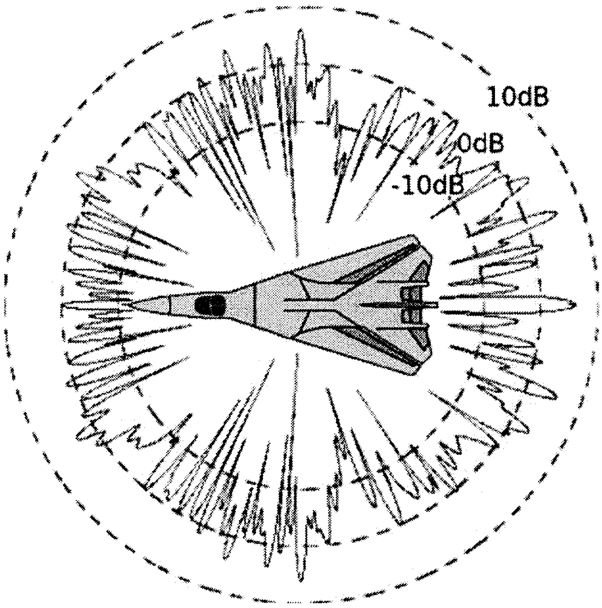

Figure 1.1 Reflected power in dB at $\theta = 0$ when illuminating from different angles.

In this dissertation spatial MIMO radar systems are considered. Such radar systems observe a target simultaneously from different uncorrelated aspects resulting in spatial diversity. This diversity overcomes the fluctuations in received power. The first studies discussing spatial MIMO radar were published by Fishler et al. [7, 8], and served as a starting point of the here presented work. In [8], the improvements in detection performance, which MIMO radar can achieve with spatial diversity, for targets in white Gaussian noise are discussed. In [7], the improvements in angle of arrival estimation are explored. Chapters 2 and 3 are extensions of these two publications. It should be noted, that this dissertation discusses only spatial diversity. Time and frequency diversity can be and are also used in radar. For example, target models according to the Swerling cases 2 and 4 inherently contain a time diversity component, [5].

It should be mentioned that the acronym MIMO has been used in the radar context in a different way, too, e.g. [9, 10]. The systems discussed generally in those publications consist of closely spaced elements, which therefore, do not capitalize on the spatial diversity. Rather, spatial filtering is achieved similar to regular beamforming.

As noted above, as long as the details of the target should not be resolved MIMO-radar relies for detection and estimation on non-coherent processing. In contrast phased array radars, which use arrays consisting of closely spaced elements on transmit and receive side, can process the signal coherently in such endeavor, but do not enjoy diversity. Particularly, in Chapter 3 and 4, it is shown that in several situations the gains achieved with diversity outweigh the drawbacks of non-coherent processing. Thus, a question analyzed in this dissertation is, whether one should place all transmit and receive elements in a small array to employ beamforming and exploit the coherent processing gain or eventually distribute those elements in space to achieve diversity.

Chapter 2 discusses transmit diversity in the context of direction finding in radar. Ergodic and outage Cramer Rao bounds for the best possible accuracy of angle of arrival estimations are introduced. Furthermore, the effect of correlations between the target's returns in different diversity branches are explored with simulation results. It is noted that the in [11] introduced outage Cramer Rao bound is used by Li et al. in [12], too.

Chapter 3 extends the studies presented in [7] considering diversity on transmit and receive side to models that include eventual different path losses across the diversity branches due to the widely separated system elements. Further, correlations between the target aspects are considered, too. Furthermore, a trade off between the extends of diversity gain and coherent processing gain are desirable is developed.

Chapter 4 is extending the spatial diversity considerations to include moving targets and clutter returns. Particularly, this chapter shows, that, as the Doppler introduced by the target's movement is crucial for distinguishing between target and clutter, a target moving with an arbitrary direction may already due to its eventual low radial velocity appear as a fading target even without RCS fluctuations. The impairment imposed by this effect can also be overcome with spatial diversity.

In [13], it is argued that multi-static radar systems are capable of circumventing this obstacle, as they observe a target from different aspects and the target cannot have vanishing velocity components towards all of these aspects. However, in [13] no definite results are provided. In general, MIMO radar can be viewed a generalization of multi-static radar setups. However, multi-static systems, which are commonly treated as a network of radar systems, [14], do normally some local processing at each receive station before the central station yields the final decision or estimation. In contrast, in MIMO radar all signals are processed *jointly* in one central entity. In Chapter 4, the difference between this two approaches is discussed and evaluated for the moving target scenario. It is shown that MIMO systems outperform the multi-static ones because of information losses in the distributed processing. The fusion of locally pre-processed data in multi-static systems is commonly done to limit the amount of data transmitted from the individual stations to the central one. Given the advances in wired and wireless communications over the last two decades, one may argue that it is time to drop the data link constraint for an application as crucial as radar.

For completeness, a brief overview over multi-static radar and sonar publications is provided here. Transmit diversity for multistatic sonar is, for example, analyzed in [15]. But the diversity is discussed with respect to different types of background noise and different propagation paths and not with respect to target aspects. Using several separated transmitters in a multistatic radar is proposed in e.g. [16]. However, the motivation to distribute the illumination sources is to hide them rather than achieve diversity. Another motivation for multi-static radars found in the literature is the rejection of false targets due to reflections of a real target on some clutter, e.g. [17]. An extensive treatment of multi-static systems can be found in [13].

In Chapter 4, the statistics of the clutter returns are initially assumed to be known for simplicity. However, towards the end of the chapter an adaptive MIMO moving target detector is introduced and its constant false alarm rate (CFAR) features are illustrated.

A difference between communications and radar should be brought to the reader's attention here. In communications the channel is assumed to be known or sufficiently estimated. Further, commonly the phase and frequency offsets are assumed to be limited. Therefore, diversity in MIMO communications is mainly discussed for coherent systems. In contrast, in radar the target, which is to be detected or parameters of which have to be estimated, is the main part of the channel. Accordingly, detection and target location estimation is done *non-coherently*. Chapter 3 is discussing the drawbacks of this kind of processing.

In Chapter 5, *coherent* processing is introduced for resolving the dominant scatterers contributing to a target's return or several closely spaced targets. The capability of a radar system to resolve scatterers is normally determined by the used bandwidth. In Chapter 5, it is argued that with coherent spatial processing this limitations can be overcome. This represents a similarity to the multiplexing capabilities enjoyed by MIMO systems in communications. The high resolution abilities of coherent MIMO radar are explored with a 2-dimensional ambiguity function and Cramer Rao bounds for the location estimation accuracy possible for a single isotropic reflector. The importance of the employed signal bandwidth for limiting possible ambiguities in the location estimates is analyzed for random sensor locations.

CHAPTER 2

TRANSMIT DIVERSITY IN MIMO-RADAR DIRECTION FINDING

This chapter explores the diversity gain which can be achieved with diversity on the transmit side for angle of arrival (AOA) estimation. For simplicity, target range and velocity and focus are ignored. The advantages of MIMO radar are demonstrated by comparing the possible and achieved precision of direction finding approaches. For the purpose of this analysis, the problem of estimating the AOA of a single target illuminated by one or several sources is considered. This may be viewed as an extension of the classical active direction finding (DF) problem in radar or sonar, [18, 19]. For direction finding, an array of closely spaced antennas is employed at the receive side to enable unambiguous angle estimation, [20, 21, 22].

2.1 MIMO Radar Signal Model

In this section, a general signal model for the MIMO radar is described. The model focuses on the effect of the target spatial properties ignoring range and Doppler effects. The signal model separates the target's effect from the effects of the antenna layouts and of the propagation between transmitters and target and between target and receivers. By doing so, it provides insight into the principles of MIMO radar. Especially, the model reflects how the target properties, its size etc., contribute to the dependency of the RCS on the aspect. This allows to derive a condition for the separation among the MIMO antennas necessary to achieve independent fading across the different target aspects.

2.1.1 General Signal Model

Not surprisingly, the radar MIMO signal and channel models are related to MIMO channel models for communications, for example [23]. The signal model developed here is sufficiently general that it can be used to describe both, conventional radar systems and MIMO radar systems. In this chapter, a MIMO radar system with two uniform linear arrays of M antennas at the transmitter and N antennas at the receiver is assumed. The transmitter and the receiver arrays are not necessarily collocated (bistatic radar). Further, a far field complex target consisting of many, Q, independent scatterers is assumed. The target is illuminated by narrowband signals, whose amplitudes do not change appreciably across the target. This means roughly a bandwidth smaller than c/D, where c is the speed of light and D is the target length. Each scatterer is assumed to have isotropic reflectivity modeled by zero-mean, unit-variance per dimension, independent and identically distributed (i.i.d.) Gaussian complex random variables ζ_q. The target is then modeled by the diagonal matrix

$$\Sigma = \frac{1}{\sqrt{2Q}} \begin{pmatrix} \zeta_0 & 0 & \cdots & 0 \\ 0 & \zeta_1 & \ddots & \vdots \\ \vdots & \ddots & \ddots & 0 \\ 0 & \cdots & 0 & \zeta_{Q-1} \end{pmatrix}, \tag{2.1}$$

where the normalization factor makes the target average RCS $E[\text{trace}(\Sigma\Sigma^H)] = 1$ independent of the number of scatterers in the model[1]. If the RCS fluctuations are fixed during an antenna scan, but vary independently from scan to scan, the target model represents a classical Swerling case 1, which represents a target in slow motion, [5].

For simplicity, it is assumed in this chapter that the target scatterers are laid out as a linear array, and that this array and the arrays at the transmitter and receiver are parallel. Figure 2.1 illustrates the model.

The signals radiated by the M transmit antennas impinge on the Q scatterers at angles $\phi_{m,q}$, $q = 0, \dots, Q-1$ and $m = 0, \dots, M-1$ (measured with respect to the normal to the arrays). Assuming that the length of the target array is small compared to the distance, the signal transmitted by the m-th transmit antenna arrives as a planewave at the target. Thus,

---

[1] The superscript H, as in Σ^H, denotes the Hermitian transposed.

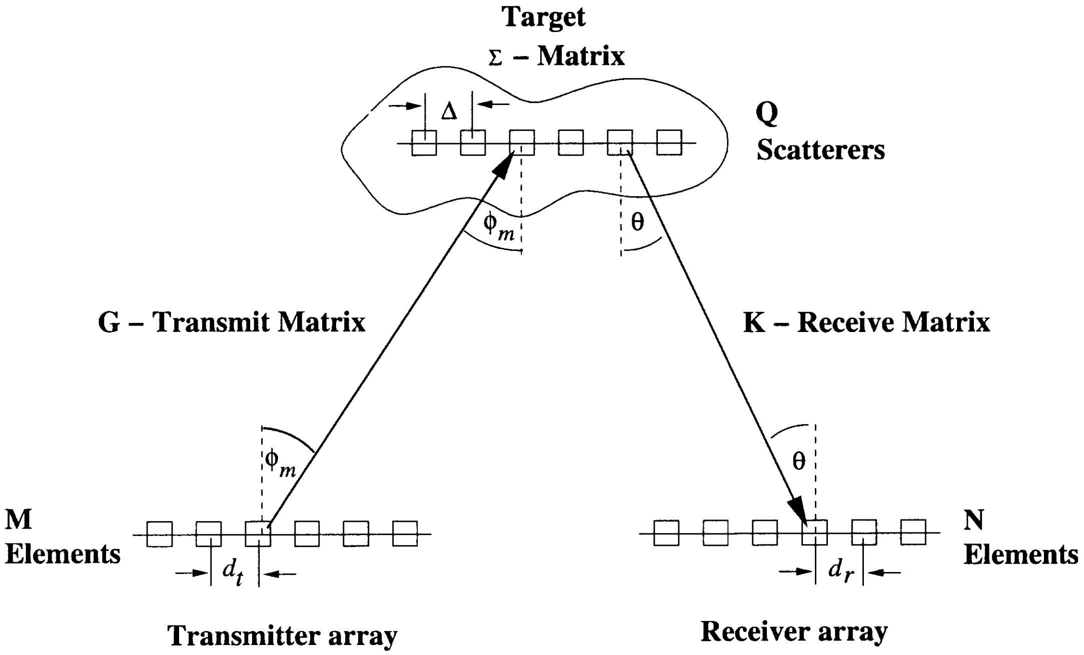

Figure 2.1 Bistatic radar scenario. The target consists of multiple scatterers organized in the form of a linear array.

the angle of arrival at the target is identical for all scatterers, $\phi_{m,q} = \phi_m, \quad \forall q$. The signal vector induced by the m-th transmit antenna is given by

$$\mathbf{g}_m = \left[1, e^{-j2\pi \sin\phi_m \Delta_2/\lambda}, \ldots, e^{-j2\pi \sin\phi_m \Delta_Q/\lambda}\right]^T, \tag{2.2}$$

where Δ_q is the spacing between the first and $(q+1)$-th scatterer, λ is the carrier wavelength, and the superscript T denotes vector/matrix transposition. Further it is assumed in this chapter, that the target scatterers are uniformly spaced, i.e., $\Delta_q = q \cdot \Delta$. Therefore, the vector $\mathbf{g}_m$ describes the different phase-shifted versions of the signal transmitted by the m-th transmitter arriving at the different scatterers.

The signals are reflected by the target scatterers towards the receiver array elements at angles $\theta_{n,q}$, $n = 0, \ldots, N-1$ and $q = 0, \ldots, Q-1$. Assuming that both the sizes of the target and the receiver arrays are small compared to the distance between them, it is found that $\theta_{n,q} = \theta$. The signals reflected by the scatterers have in the far field, relative phase shifts described by the vector $\mathbf{k}(\theta)$,

$$\mathbf{k}(\theta) = \left[1, e^{j2\pi \sin\theta\Delta/\lambda}, \ldots, e^{j2\pi \sin\theta(Q-1)\Delta/\lambda}\right]^T. \tag{2.3}$$

A planewave signal arriving at the array at the angle θ excites the elements of the array with phase shifts given by the vector $\mathbf{a}(\theta)$,

$$\mathbf{a}(\theta) = \left[1, e^{-j2\pi \sin\theta d_r/\lambda}, \ldots, e^{-j2\pi \sin\theta(N-1)d_r/\lambda}\right]^T, \tag{2.4}$$

where d_r denotes the inter element spacing at the receiver. In this chapter, a spacing of $d_r = \lambda/2$ is assumed to enable unambiguous direction finding.

With the vectors and the target matrix defined above, the received signals originating from the m-th transmitter and reflected by the target can be expressed as

$$\mathbf{r}'_m = \mathbf{a}(\theta)\mathbf{k}^T(\theta)\Sigma\mathbf{g}_m b_m s_m. \tag{2.5}$$

The terms b_m are complex variables representing the phase shifts between the signals coming from different transmitters due to the different propagation delays. Without loss of generality, these phase shifts can be embedded in $\mathbf{g}_m$. The complex scalar s_m represents the component of the sampled receive filter output due to the waveform transmitted by the m-th transmitter. Organizing those scalars in the vector $\mathbf{s} = [s_0, \ldots, s_M]^T$, the received signal can be described as

$$\begin{aligned}\mathbf{r} &= \mathbf{a}(\theta)\mathbf{k}^T(\theta)\Sigma\sum_{m=0}^{M-1}\mathbf{g}_m s_m + \mathbf{v}\\ &= \mathbf{K}\Sigma\mathbf{G}\mathbf{s} + \mathbf{v}\\ &= \mathbf{H}\mathbf{s} + \mathbf{v}.\end{aligned} \tag{2.6}$$

The vector $\boldsymbol{r} = [r_1, \ldots, r_{N-1}]^T$ contains the sampled output of the filters at the N receiver elements, $\mathbf{v}$ represents the additive Gaussian noise terms at the receivers after the receive filters. The noise components among the receive elements are assumed i.i.d. .

Further, the matrix $\mathbf{K} = \mathbf{a}(\theta)\mathbf{k}^T(\theta)$ represents the propagation paths from the scatterers to the receivers, and the matrix $\mathbf{G} = [\mathbf{g}_0, \ldots, \mathbf{g}_{M-1}]$ the ones from the transmitters to the individual target scatterers. The $N \times M$ matrix $\mathbf{H}$ incorporates the paths from all transmitters to all receivers. The effect of the vector $\mathbf{k}(\theta)$ is to combine the signals coming from the individual scatterers in the far field. As it is assumed that Σ consists of complex-valued random scatterers, the effect of $\mathbf{k}(\theta)$ can be embedded in Σ and $\mathbf{k}(\theta)$ can be replaced with $\mathbf{1}_Q = [1, \ldots, 1]^T$, without loss of generality.

To achieve spatial diversity, it is required that different transmit antennas see uncorrelated aspects of the target. To analyze the condition under which this is the case, the received signal components due to the m-th transmitter are considered again:

$$\mathbf{r}'_m = \frac{1}{\sqrt{2}}\mathbf{a}(\theta)\alpha_m s_m \tag{2.7}$$

Here, the target fading effect is summarized in the fading coefficient α_m given by $\alpha_m = \sqrt{2}\mathbf{1}_Q^T\Sigma\mathbf{g}_m$. The factor $\sqrt{2}$ is introduced here so that the $|\alpha_m|^2$ random variables have a χ_2^2 distribution, which will ease later considerations. The previously mentioned uncorrelated target aspects result in uncorrelated fading coefficients. As the fading coefficients are modeled as zero mean and independent, it is found $E\{\alpha_m^*\alpha_{m+1}\} = 0$, which leads to

$$\begin{aligned} E\{\alpha_m^*\alpha_{m+1}\} &= E\{\mathbf{g}_m^H\Sigma^H\mathbf{1}_Q\mathbf{1}_Q^T\Sigma\mathbf{g}_{m+1}\} \\ &= \mathbf{g}_m^H E\{\Sigma^H\mathbf{1}_Q\mathbf{1}_Q^T\Sigma\}\mathbf{g}_{m+1} \\ &= \frac{1}{2Q}\mathbf{g}_m^H\mathbf{I}_Q\mathbf{g}_{m+1} = 0. \end{aligned} \tag{2.8}$$

Thus, the fading constants for the different transmitters are uncorrelated if the columns of G are orthogonal:

$$\mathbf{g}_m^H\mathbf{g}_{m+1} = \sum_{q=0}^{Q-1} e^{j2\pi[(\sin\phi_{m+1} - \sin\phi_m)q\Delta/\lambda]} = 0 \tag{2.9}$$

For small angles ϕ_m and ϕ_{m+1} expressed in radians, the difference of the sine terms in (2.9) can be approximated with

$$\sin\phi_{m+1} - \sin\phi_m \approx d_t/R, \tag{2.10}$$

where d_t is the inter-element spacing at the transmitter and R is the distance between the target and the transmitter. Using this in (2.9) leads to

$$\sum_{q=0}^{Q-1} e^{j2\pi(d_t/R)q\Delta/\lambda} = 0. \tag{2.11}$$

Thus, orthogonality is achieved when the angles complete one turn in the complex plane:

$$\frac{d_t\Delta}{\lambda R} = \frac{1}{Q} \tag{2.12}$$

However, for large values of Q and for

$$\frac{d_t\Delta}{\lambda R} \geq \frac{1}{Q} \tag{2.13}$$

the orthogonality condition (2.11) is approximately met. A similar argument is made in [23]. This condition obtained solely from geometric considerations has an appealing intuitive physical interpretation. The beamwidth of the energy backscattered from the target towards the transmitter is approximately given by λ/D, where $D = Q \cdot \Delta$ is the target size. The target presents different aspects to adjacent transmit antennas if the inter-element spacing at the transmitter is greater than the target beamwidth coverage at distance R, namely

$$d_t \geq \frac{\lambda R}{D}, \tag{2.14}$$

which turns out to be the same as (2.13). It is noted, that the here presented target model is rather simple. However, its main purpose is to derive a condition for independent fading coefficients over the target. In [8] a more sophisticated model with a continuous

2-dimensional scatterer distribution is discussed, which results in the same condition, (2.14). In contrast to [8], in this and the next chapter the effect of correlated fading coefficients and target aspects are discussed, too.

2.1.2 Classification of Different Radar Systems within the General Model

MIMO radar systems can be classified within the above described general model into three different groups:

- Conventional radar array modeled with an array at the receiver and a single antenna or an array at the transmitter. The array elements are spaced at half-wavelengths to enable beamforming and DF.
- MIMO radar for DF. Transmit antenna elements are widely spaced to support spatial diversity with respect to the aspects of the target. The receiver array performs DF.
- MIMO radar with widely separated antennas at both the transmitter and the receiver.

This chapter discusses the first two signal models, whereas the third one is discussed in is introduced in the next chapter.

Conventional Radar Array Conventional radar arrays are systems, in which the elements of the transmitting and receiving arrays are closely spaced. At the transmitter, that means that the inter-element spacing does not meet (2.13) or, equivalently, that multiple elements are contained within one target beamwidth. At the receiver, the spacing is $d_r \leq \lambda/2$ to enable unambiguous estimation of the angle of arrival.

The target bearings with respect to the transmit and receive arrays are ϕ and θ, respectively. The term b_m in (2.5) is given by $b_m = e^{-2\pi \sin\phi \, m d_t/R}$. As mentioned before, those phase shifts can be neglected in the MIMO scenario. However for conventional radar they have to be included in the related expression to accommodate the eventual use of ESAs at the transmitter site. The phase shifts are collected in the vector $\mathrm{b}(\phi)$. The transmit matrix is given by $\mathbf{G} = \mathbf{1}_Q \mathrm{b}^T(\phi)$. The receive matrix is given by $\mathbf{K} = \mathrm{a}(\theta)\mathbf{1}_Q^T$. It is noted, that actually $\mathbf{G}$ and $\mathbf{K}$ should both contain the vectors $\mathbf{g}(\phi)$ and $\mathbf{k}(\theta)$, respectively. However, as those vectors are constant for all receiver and transmitter elements and because of the randomness of the Σ matrix, they can be replaced by $\mathbf{1}_Q$ without losing any insight. It follows that the channel matrix is given by

$$\begin{aligned}\mathbf{H} &= \mathbf{a}(\theta)\mathbf{1}_Q^T\Sigma\mathbf{1}_Q\mathbf{b}^T(\phi)\\ &= \frac{1}{\sqrt{2}}\alpha\mathbf{a}(\theta)\mathbf{b}^T(\phi),\end{aligned} \tag{2.15}$$

where the fading coefficient is $\alpha = \sqrt{2}\cdot\mathbf{1}_Q^T\Sigma\mathbf{1}_Q$. By assumption, the elements of Σ, ζ_q (see (2.1)), are zero-mean, unit-variance per dimension, i.i.d. Gaussian random variables. Hence, α is a zero-mean, complex Gaussian random variable, too. Accordingly, the target's RCS $|\alpha|^2$, follows a χ_2^2 chi-square distribution with 2 degrees of freedom. Note that with this model, there is no diversity "gain" in the target RCS.

The beamforming of a conventional radar array on the transmit side is represented by the vector $\mathbf{b}^*(\phi')$. As the transmitter elements radiate the same waveform with different phases, the received signal can be expressed as

$$\mathbf{r} = \frac{1}{\sqrt{2}}\mathbf{a}(\theta)\mathbf{b}^T(\phi)\mathbf{b}^*(\phi')\alpha s + \mathbf{v}, \tag{2.16}$$

where s is a scalar representing the filter outputs due to the single transmitted waveform. Now, if the receiver uses a beamformer to steer towards direction θ', then the output of the beamformer processing is

$$\begin{aligned}y &= \mathbf{a}^H(\theta')\mathbf{r} + \mathbf{v}'\\ &= \frac{1}{\sqrt{2}}\mathbf{a}^H(\theta')\mathbf{a}(\theta)\mathbf{b}^T(\phi)\mathbf{b}^*(\phi')\alpha s + \mathbf{v}'.\end{aligned} \tag{2.17}$$

This model represents a bistatic radar where $\mathbf{b}^T(\phi)\mathbf{b}^*(\phi')$ plays the role of the transmit antenna pattern, whereas $\mathbf{a}^H(\theta')\mathbf{a}(\theta)$ is the receive antenna pattern. The angle of arrival is estimated as the θ' which maximizes $|y|^2$. The target component, which maximizes $|y|^2$ at the estimated angle of arrival, is subject to fading due to the $|\alpha|^2$ multiplier. In the scenario considered here, which equals the Swerling I case, this fading gain has a χ_2^2 distribution (chi-square with 2 degrees of freedom).

MIMO Radar - Direction Finding In MIMO radar for direction finding (DF), the transmit antennas are sufficiently separated to meet the orthogonality condition (2.13) for targets of interest. Equivalently, the columns of the transmit matrix G meet the orthogonality condition in (2.9). In contrast, elements of the receive array are closely separated to enable DF measurements. The target is at angle θ with respect to the receive array normal. The receive matrix is given by $\mathbf{K} = \mathrm{a}(\theta)1_Q^T$. From (2.6), it follows that the channel matrix is given by

$$\mathrm{H} = \frac{1}{\sqrt{2}}\mathrm{a}(\theta)\boldsymbol{\alpha}^T, \tag{2.18}$$

where the components α_m of the $M \times 1$ vector $\boldsymbol{\alpha}$, are the previously introduced target fading coefficients for each target illuminating path, $\alpha_m = \sqrt{2} \cdot \mathbf{1}_Q^T\Sigma\mathrm{g}_m$. Thus, the vector $\boldsymbol{\alpha}$ is given as $\boldsymbol{\alpha} = \sqrt{2} \cdot (1_Q^T\Sigma\mathrm{G})^T$. Due to the orthogonality among the transmit vectors g_m, the variates α_m are uncorrelated. Moreover, the random variables α_m are zero-mean, unit-variance (per dimension), independent, identical distributed (i.i.d.) complex normal.

The signal model is given by

$$\begin{aligned}\mathrm{r} &= \frac{1}{\sqrt{2}}\left(\mathrm{a}(\theta)\boldsymbol{\alpha}^T\right)\mathrm{s}+\mathrm{v} \\ &= \frac{1}{\sqrt{2}}\mathrm{a}(\theta)\sum_{i=0}^{M-1}\alpha_i s_i + \mathrm{v}.\end{aligned} \tag{2.19}$$

Assuming that the total transmission power is independent of the number of transmitters, e.g. $\sum_{i=0}^{M-1} E\{|s_i|^2\} = 1$, the signal model, with all normalization factors specified so far, ensures that the average received power $E\Big\{\Big|(1/\sqrt{2})\sum_{i=0}^{M-1}\alpha_i s_i\Big|^2\Big\} = 1$. Conditioned on the fading constants vector $\boldsymbol{\alpha}$ and the signal vector s, the received vector r is complex, multivariate normal with correlation matrix $\frac{1}{2}\left\|\boldsymbol{\alpha}^T\mathrm{s}\right\|^2\mathrm{a}(\theta)\mathrm{a}^H(\theta) + 2\sigma^2\mathbf{I}_N$.

To illustrate how the considered system utilizes diversity, $M = 2$ is assumed here. First the properties of one signal and its power at a single receiver element are analyzed ignoring the phase shifts along the array:

$$\begin{aligned} r &= \frac{1}{\sqrt{2}}(\alpha_0 s_0 + \alpha_1 s_1) + v \\ |r|^2 &= \frac{1}{2}|\alpha_0 s_0 + \alpha_1 s_1 + v|^2 \end{aligned} \tag{2.20}$$

The diversity cannot be utilized in this manner, as the signal components s_i might destructively interfere with each other, since the fading coefficients α_i are unknown *a priori*. To prevent this effect, orthogonal waveforms can be employed. However, in this chapter, it is assumed that the transmitted waveforms result in random and mutually independent components, s_i, of the sampled receive filter outputs. Evaluating the expectation of the received signal power leads to

$$\begin{aligned} E\{|r|^2\} &= E\{|\frac{1}{\sqrt{2}}(\alpha_0 s_0 + \alpha_1 s_1) + v|^2\} \\ &= \frac{1}{4}(|\alpha_0|^2 + |\alpha_1|^2) + 2\sigma^2, \end{aligned} \tag{2.21}$$

where $E\{|s_i|^2\} = \frac{1}{2}$ has been used. In the considered scenario, the angle of arrival estimate is based on a sufficiently large number of snapshots during which the fading coefficients are assumed to be constant. The waveforms of each transmitter result in a different random output component for each snapshot. Thus, when the number of snapshots is sufficiently large, the sum over the received power may be approximated as

$$\begin{aligned} \sum_{i=0}^{L-1} |r_i|^2 &= \sum_{l=0}^{L-1} |\frac{1}{\sqrt{2}}(\alpha_0 s_{0,l} + \alpha_1 s_{1,l}) + v_l|^2 \\ &\approx \frac{1}{4}(|\alpha_0|^2 + |\alpha_1|^2)L\hat{s}^2 + 2L\hat{\sigma}^2, \end{aligned} \tag{2.22}$$

where $\hat{s}^2$ and $\hat{\sigma}$ indicate, that these values are estimates of the (single) signal and noise power, which are random variables. In the remainder of this chapter, it is assumed that a sufficiently large number of snapshots is processed, and that therefore the power of the target component is determined by the (scaled) sum of the squared absolute values of the fading coefficients. Including the array on the receive side, the vector of the received samples along the array can be expressed as

$$\mathbf{r} = \mathbf{a}(\theta)\frac{1}{\sqrt{2}}(\alpha_0 s_0 + \alpha_1 s_1) + \mathbf{v}. \tag{2.23}$$

To estimate the angle of arrival over several snapshots, the following expression is evaluated:

$$\begin{aligned}\xi(\theta') = \sum_{l=0}^{L-1} |\mathbf{a}(\theta')\mathbf{r}_l|^2 &= \sum_{l=0}^{L-1} |\mathbf{a}^H(\theta')\mathbf{a}(\theta)\frac{1}{\sqrt{2}}(\alpha_0 s_{0,l} + \alpha_1 s_{1,l}) + \mathbf{a}^H(\theta')\mathbf{v}_l|^2 \\ &\approx |\mathbf{a}^H(\theta')\mathbf{a}(\theta)|^2 \, \frac{1}{4}(|\alpha_0|^2 + |\alpha_1|^2) \; L\hat{s}^2 + LN\hat{\sigma}^2 \end{aligned} \tag{2.24}$$

The angle of arrival is estimated as the θ' which maximizes $\xi(\theta')$. For the correct estimate $\theta' = \theta$ the term $|\mathbf{a}^H(\theta')\mathbf{a}(\theta)|^2$ equals N^2. Again, the target component in this estimation is subject to fading. However, the fading is due to the *sum* of $|\alpha_0|^2$ and $|\alpha_1|^2$. As the random variables $|\alpha_i|^2$, $i = 0, 1$, have a χ_2^2 distribution, and are i.i.d. (due to the orthogonality between $\mathbf{g}_0$ and $\mathbf{g}_1$), their sum in (2.24) has a χ_4^2 (chi-square with 4 degrees of freedom) distribution. This is a consequence of the different, uncorrelated RCS's presented by the target to the different elements of the transmitting array. Due to the scaling in (2.24) and (2.17) the average signal power reflected by the target is in both cases 1. The reflected power is in the conventional radar case, (2.17), a scaled χ_2^2 random variable; whereas it is a scaled χ_4^2 random variable in the MIMO scenario, (2.24). The latter has a smaller variance than the first. Thus, the *diversity* results in a more advantageous distribution of the target component in the received signal. The resulting performance improvement is called *diversity gain* and is explored by different means in the following sections.

Assuming that the different transmit signals result in i.i.d. Gaussian random variables after the receive filters facilitates the mathematical analysis carried out in this chapter. Moreover, this assumption keeps the derived results general without limiting the discussion to particular transmit waveforms or signals. However, apart from the resulting analytical tractability and generality, the assumption applies to passive radar systems using *sources of opportunity*, e.g. [24, 25], to estimate the bearing of targets without knowledge of the specific transmitted signals and waveforms. Indeed, the analysis of this chapter may provide an answer to the question whether passive system based on triangulation should be based on, say, a broadcast medium, such as TV, or use a cellular network as illuminating source. However, this discussion is beyond the scope of this proposal. Instead the diversity gains for AOA in the MIMO context should be explored subsequently.

2.2 MIMO DF Analysis

In this section, the performance of a MIMO radar when used as a DF system is examined. The following assumptions are made for simplicity and mathematical tractability:

1. Several, independent snapshots of the target are available for processing.
2. The transmitted waveforms result in components of the receive filter output summarized in the vector s for each snapshot. The vector is modeled as Gaussian random with independent components. Thus, the effective illumination process is spatially white and its correlation matrix is $(1/M)\,\mathbf{I}_M$.
3. The antenna elements of both the transmitting and the receiving arrays are omnidirectional.
4. Since a DF application is to be explored, it is assumed, that the signals from the different transmitters arrive synchronized at the receiver.

A common figure of merit for comparing the performance of different systems is the estimators' mean square error (MSE). A system's MSE depends on the exact estimation method, e.g., ML, MUSIC, beamforming, used. In order to have a fair comparison between different systems the Cramer Rao bound is evaluated, which serves as a lower bound on the performance of all unbiased estimators.

2.2.1 Cramer Rao Bound

In what follows, the performance of a MIMO radar used as an active direction finder with $M \geq 1$ distributed transmitting elements is analyzed. The received signal is given by the model (2.19). In this model there are three unknown parameters, the direction parameter θ, the target's fading parameters contained in $\boldsymbol{\alpha} = [\alpha_0, \ldots, \alpha_{M-1}]^T$, and the noise power σ^2. The vector containing all the unknown parameters is $\boldsymbol{\psi} = [\theta, \sigma^2, \boldsymbol{\alpha}]$. In the subsequent, $f(\mathbf{r}|\boldsymbol{\psi})$ denotes the family of probability density functions (pdf) of the received signal parameterized by the vector of unknown parameters in $\boldsymbol{\psi}$ and $\mathbf{C}(\boldsymbol{\psi})$ the correlation matrix of the error in estimating $\boldsymbol{\psi}$ of any unbiased estimator. The Cramer-Rao lower bound for estimating $\boldsymbol{\psi}$ is given by

$$\mathbf{C}(\boldsymbol{\psi}) \geq \mathrm{CRB}(\boldsymbol{\psi}) = \mathbf{J}^{-1}(\boldsymbol{\psi}) = \left(-E\left\{ \frac{\partial^2 \ln f(\mathbf{r}|\boldsymbol{\psi})}{\partial \boldsymbol{\psi} \partial \boldsymbol{\psi}^T} \right\} \right)^{-1} . \tag{2.25}$$

The $\geq$ indicates in this context, that the result of $\mathbf{C}(\boldsymbol{\psi}) - \mathrm{CRB}(\boldsymbol{\psi})$ is a positive definite matrix. This particularly implies $\mathrm{C}_{1,1}(\boldsymbol{\psi}) \geq \mathrm{CRB}_{1,1}(\boldsymbol{\psi})$. For the AOA estimation only the direction θ is of interest and therefore the $[1,1]$ elements of $\mathbf{C}(\boldsymbol{\psi})$ and $\mathrm{CRB}(\psi)$, respectively. The other parameters are nuisance parameters. Particularly, it is noted that the problem decouples, which means that the estimation error of the AOA is independent of the estimation error of the signal and noise power. $\mathrm{CRB}(\theta|\boldsymbol{\alpha})$ denotes the $[1,1]$ element of the Cramer Rao bound matrix. This notation indicates the conditioning of the bound on the unknown parameters in $\boldsymbol{\alpha}$. Given that the signals from the M transmitters are unknown complex Gaussian random variables with the correlation matrix $(1/M)\mathbf{I}_N$ and conditioned on $\boldsymbol{\alpha}$, $\mathbf{r}$ is a complex normal random vector with correlation matrix $\mathbf{C}_\mathbf{r} = (2M)^{-1}||\boldsymbol{\alpha}||^2\mathbf{a}(\theta)\mathbf{a}^H(\theta) + 2\sigma^2\mathbf{I}_N$. Here, it is noted again, that $||\boldsymbol{\alpha}||^2$ is χ^2_{2M} distributed.

The CRB conditioned on the fading coefficients is derived in Appendix A. Further, the reader is refered to textbook derivations for more general expressions given in [26] or [27],

$$\mathrm{CRB}(\theta|\boldsymbol{\alpha}) = \frac{6}{L\pi^2\cos^2\theta(N^2-1)}\left(\frac{2\sigma^2 2M}{N||\boldsymbol{\alpha}||^2} + \frac{(2\sigma^2)^2 4M^2}{N^2||\boldsymbol{\alpha}||^4}\right) \tag{2.26}$$

where L is the number of snapshots used by the array for estimating θ. This expression is based on assuming an Uniform Linear Array (ULA) at the receiver with an inter element spacing of $\lambda/2$. Therefore, the elements of the vector $\mathrm{a}(\theta)$ are given by $[\mathrm{a}(\theta)]_k = e^{j\pi\sin\theta k}$.

2.2.2 Average CRB

An lower bound the *average* MSE of any unbiased estimator can be introduced by averaging the CRB with respect to $\boldsymbol{\alpha}$. This bound is denoted by $\mathrm{ACRB}(\theta) = E_{\boldsymbol{\alpha}}\{\mathrm{CRB}(\theta|\boldsymbol{\alpha})\}$. Using (2.26), the $\mathrm{ACRB}(\theta)$ is given by

$$\begin{aligned}\mathrm{ACRB}(\theta) &= E_{\boldsymbol{\alpha}}\{\mathrm{CRB}(\theta|\boldsymbol{\alpha})\}\\ &= \frac{6}{L\pi^2\cos^2\theta(N^2-1)}\left(\frac{2\sigma^2 2M}{N}E_{\boldsymbol{\alpha}}\left\{\frac{1}{||\boldsymbol{\alpha}||^2}\right\} + \frac{(2\sigma^2)^2 4M^2}{N^2}E_{\boldsymbol{\alpha}}\left\{\frac{1}{||\boldsymbol{\alpha}||^4}\right\}\right).\end{aligned} \tag{2.27}$$

Using

$$E_{\chi^2_{2M}}\left\{\frac{1}{X}\right\} = \int_0^\infty \frac{x^{M-2}e^{-x/2}}{\Gamma(M)\,2^M}dx = \frac{1}{2(M-1)} \qquad \forall M > 1$$

and

$$E_{\chi^2_{2M}}\left\{\frac{1}{X^2}\right\} = \int_0^\infty \frac{x^{M-2}e^{-x/2}}{\Gamma(M)\,2^M}dx = \frac{1}{2^2(M-1)(M-2)}, \qquad \forall M > 2$$

it can be realized, that the ACRB is given by

$$\mathrm{ACRB}(\theta) = \frac{6}{L\pi^2\cos^2\theta(N^2-1)}\left(\frac{2\sigma^2 M}{N(M-1)} + \frac{(2\sigma^2)^2 M^2}{N^2(M-1)(M-2)}\right) \qquad \forall M > 2. \tag{2.28}$$

Before investigating the dependency of the ACRB on the number of transmit antennas M, some special cases of the parameters θ and N shall be explored here for illustration.

$\theta \to \pi/2$: Here $\mathrm{ACRB}(\theta) \to \infty$ confirms that the direction cannot be estimated at endfire, since the array has a zero effective aperture (zero resolution).

$\theta = 0$: This is the best case for estimating the direction parameter. Indeed, at broadside the array has the largest effective aperture (best resolution). In the following $\theta = 0$ is assumed unless stated otherwise.

$N = 1$: The bound is infinite. Indeed, a single omnidirectional antenna cannot measure the angle of arrival.

It is easy to verify that if the target's RCS is independent of the aspect, that is if $||\boldsymbol{\alpha}||^2 = 2M$ deterministically, the CRB is independent of M. Having this in mind, it is only natural to define the system's Fading Loss (FL) as the additional SNR necessary to achieve the same average MSE as a system, which is not subject to fading.

By taking the ratio of the ACRB given (2.28) and the unfaded CRB given by (2.26) with $||\boldsymbol{\alpha}||^2 = 2M$, it is easy to verify that the fading loss (in dB) as a function of the number of elements in the transmitting array is lower and upper bounded as

$$10 \log_{10} \frac{M}{M-1} \leq \mathrm{FL}(M) \leq 10 \log_{10} \frac{M}{\sqrt{(M-1)(M-2)}}. \qquad (2.29)$$

For $M \leq 2$ no finite expression for the ACRB can be found, as the unlimited error of the instantaneous CRB increases faster towards infinity than the probability weight function decreases towards zero for a decreasing $||\boldsymbol{\alpha}||^2$. This means, that the integral related to evaluating $E_X\{\frac{1}{X}\}$ does not converge when X is χ_2^2 distributed and the one related to $E_X\{\frac{1}{X^2}\}$ does not converge when X is χ_2^2 or χ_4^2. Therefore, the expressions in (2.28) and (2.29) are only valid for $M \geq 3$. As the integral does not converge to a finite value, the ACRB is infinite.

If one hypothetically considers $M = 1$ and 2 in the expressions (2.28) and (2.29) one finds that the ACRB as defined by (2.28) is infinite, too. Furthermore, one can realize that the lower and upper bound for the fading loss in (2.29) are infinite for $M = 1$ and that for

$M = 2$ the upper bound for the fading loss is infinite. Thus, the expressions for the ACRB also reflect the behavior of the actual ACRB for $M = 1$ and $M = 2$.

In contrast to the ACRB and its expressions, the average MSE of an unbiased estimator might be finite even for $M = 1$ and 2, when the unknown angle parameter θ is estimated with, for example, the maximum likelihood approach. This discrepancy deserves additional consideration. The CRB bound is a small error bound. This means, it predicts the MSE based on the behavior of the log-likelihood function in the vicinity of the true parameter vector. As a small error bound, it ignores the full structure of the parameter space [27], which may result in nonsensical values. For example, in the problem at hand, if $||\boldsymbol{\alpha}||^2$ is small, the instantaneous CRB in (2.26), might be much larger than π^2. However, the MSE of any estimator is upper bounded by π^2 for all values of $||\boldsymbol{\alpha}||^2$. Thus, the average MSE of any estimator must be smaller than or equal to π^2. Hence in those cases, the ACRB is not related to the performance of any true estimator.

The next section introduces another way to evaluate the statistics of the instantenous CRB which is capable of handling small values of M.

Now, the asymptotic case $M \to \infty$ is considered. Here, the fading loss approaches zero, that is, the target's RCS 'hardens' and is not subject to fluctuations. Without target fluctuations, a case referred to as Swerling case 5, the received signal is $\mathbf{r} = \mathbf{a}(\theta)s + \mathbf{v}$. The signal component at each receive element is then a Gaussian random variable with power $|s|^2 = 1$ due to the signal model used here. With fluctuations, the received signal is $\mathbf{r} = \left(1/\sqrt{2}\right) \mathbf{a}(\theta) \sum_{m=1}^{M} \alpha_m s_m + \mathbf{v}$. The signal power at each receive element is then given by $\sum_{m=0}^{M-1} |\alpha_m|^2 \frac{1}{2} \sigma_{s_m}^2$, where the $\sigma_{s_m}^2 = \frac{1}{M}$ is the transmit power of each illuminating antenna. As $\sum_{m=0}^{M-1} |\alpha_m|^2$ is a χ_{2M}^2 random variable, the mean of the receive power is constantly 1 and the variance is $\frac{1}{M}$. Thus, as M tends towards infinity the variance of the instantaneous received signal power tends to 0 and the signal power becomes therefore deterministic.

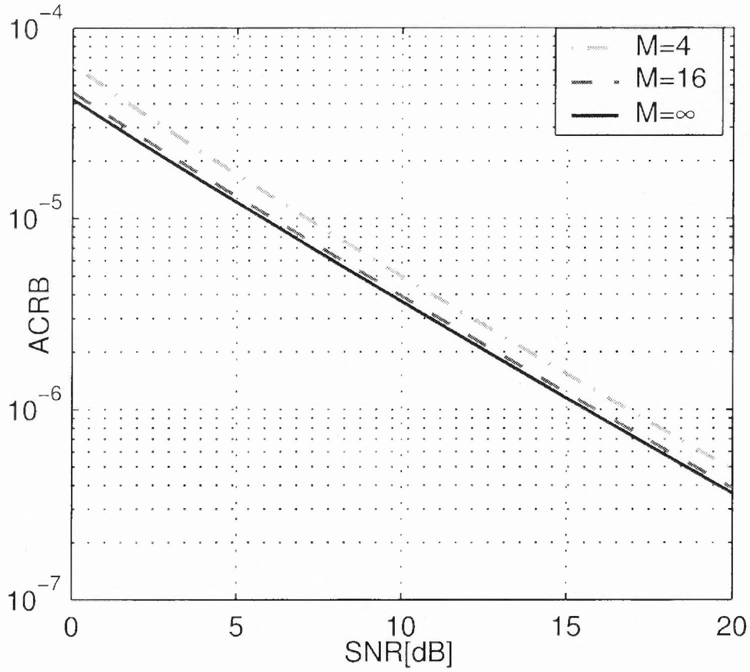

Figure 2.2 Average CRB versus SNR.

Figure 2.2 illustrates the ACRB versus the SNR for $M = 4, 16, \infty$. The SNR refers to a single snapshot, thus it is the ratio $E_{\boldsymbol{\alpha}}\{(2M)^{-1}||\boldsymbol{\alpha}||^2\}/2\sigma^2$ in dB. Other parameters are set to $N = 6$ receive antennas, $\theta = 0$ angle of arrival, and $L = 80$ snapshots.

From the figure it can be seen, that using 4 transmit antennas instead of 16 results in a fading loss of 1.3dB as predicted by (2.29). The *transmit diversity* alters the distribution of the received signal power. Even though the mean of the received signal power is the same for any number of transmit antennas, the smallest achievable average MSE of any estimator decreases with an increasing number of antennas. However, as the average is considered, the related diversity gains are not so tremendous as the ones in the next section.

2.2.3 Outage CRB

In the previous section, it has been found that the ACRB is not converging for $M \leq 2$. The *outage* CRB is introduced here to enable the analysis for $M = 1, 2$ transmit antennas.

Moreover, similar to the outage analysis in communications, the outage CRB serves as a tool for analyzing *slow* fading target cases.

Definition 2.2.1 (Outage CRB) *If the CRB for the parameter to estimate θ depends on the realization of a random variable ψ, the outage CRB for a given probability p is defined as* $\mathrm{CRB}_{out=p}(\theta)$*:*

$$Pr\Big\{\mathrm{CRB}(\theta|\psi) \geq \mathrm{CRB}_{out=p}(\theta)\Big\} = p$$

In other words, with probability $1-p$ the random variable ψ has such a realization, that the lower bound of the MSE of any estimator is smaller than $\mathrm{CRB}_{out=p}$. Therefore, it is not possible to find any estimator, which has an MSE of less than $\mathrm{CRB}_{out=p}$ with a probability $p' > 1-p$.

As the CRB in (2.26) depends on the realization of $||\boldsymbol{\alpha}||^2$, we find $\mathrm{CRB}_{out=p}$ for a given p as:

$$Pr\Big\{\mathrm{CRB}(\theta|\ ||\boldsymbol{\alpha}||^2) \geq \mathrm{CRB}_{out=p}(\theta)\Big\} = p \tag{2.30}$$

As the CRB is strictly monotonic decreasing with $||\boldsymbol{\alpha}||^2$, (2.30) indicates that an $||\boldsymbol{\alpha}_{out=p}||^2$ can be found so that

$$Pr\{||\boldsymbol{\alpha}||^2 \leq ||\boldsymbol{\alpha}||^2_{out=p}\} = p \tag{2.31}$$

and therefore

$$\mathrm{CRB}_{out=p}(\theta) = \mathrm{CRB}(\theta|\ ||\boldsymbol{\alpha}||^2_{out=p}). \tag{2.32}$$

For a given p and M the quantile $||\boldsymbol{\alpha}||^2_{out=p}$ can be found by evaluating the inverse of the χ^2_{2M} probability distribution function numerically or by using tables in, e.g., [28]. The results presented in Figure 2.3 are based on the `chi2inv` function of Matlab.

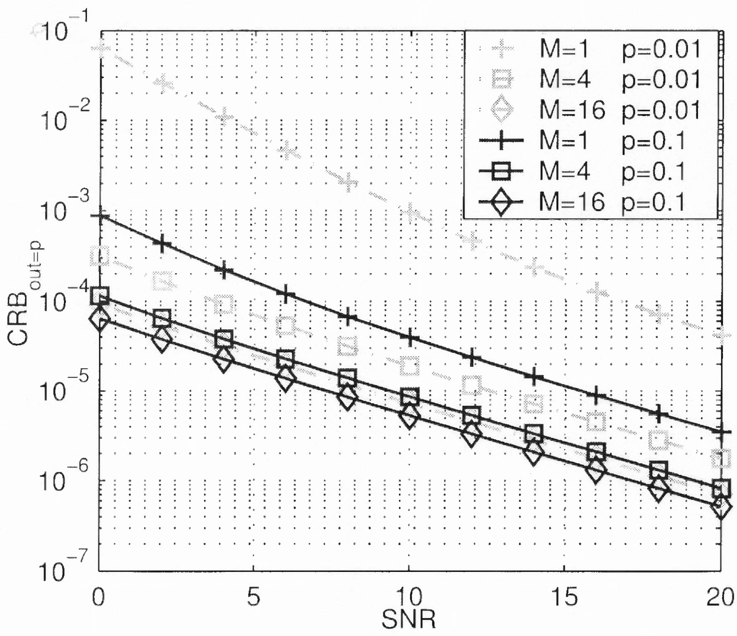

Figure 2.3 Outage CRB versus SNR.

Figure 2.3 shows $\mathrm{CRB}_{p=0.01}$ and $\mathrm{CRB}_{p=0.1}$ for different SNRs. One can see that the SNR gains depend on the probability p. In other words, when one wants to compare $M = 1, 4$ and 16 for $\mathrm{CRB}_{p=0.01}$ meaning that in 99 percent of the scenarios an estimator can achieve an MSE better than $\mathrm{CRB}_{p=0.01}$, we find that for achieving those MSE's the case $M = 1$ requires 13dB more SNR than $M = 4$ and 17dB more than $M = 16$. Further, we see that in this case, the difference between $M = 4$ and $M = 16$ is 3dB compared to the 1.4dB in the previous ACRB analysis.

The transmit diversity has a stronger impact on the outage CRB for small outages than on the ACRB, as the outage CRB is related to the tails of the distributions of $\frac{1}{||\boldsymbol{\alpha}||^2}$ and $\frac{1}{||\boldsymbol{\alpha}||^4}$ whereas the ACRB is related to their means. As stated earlier, the diversity reduces the variance of the of the received signal power, which makes the chance small, that the signal component almost vanishes due to the target fading.

2.3 Simulation Results

In this section, the MSE and the estimation error distribution of the ML–estimator are explored. A simplified scenario is assumed, in which the signals originating from the different transmitters arrive synchronized at the receiver, but are not known by the receiver. The received vector is then given by (2.6). $L = 80$ snapshots, $\theta = 0$ and $N = 6$ is considered. The angle θ is estimated at the receiver by maximizing the term $\sum_{l=1}^{L} |\mathbf{a}^H(\theta')\mathbf{r}_l|^2$, where $\mathbf{r}_l$ is the received signal of the l-th snapshot. Thus, the estimated angle of arrival $\hat{\theta}$ is:

$$\hat{\theta} \quad : \quad \sum_{l=1}^{L} |\mathbf{a}^H(\hat{\theta})\mathbf{r}_l|^2 = \max_{\theta'} \sum_{l=1}^{L} |\mathbf{a}^H(\theta')\mathbf{r}_l|^2 \tag{2.33}$$

2.3.1 Uncorrelated Target Aspects

First, the MSE and estimation error distribution are evaluated for uncorrelated target aspects. Afterwards, correlated target aspects are introduced and the MSE of the ML–estimator is introduced to explore the effects of deviations from the model discussed in section 2.1.

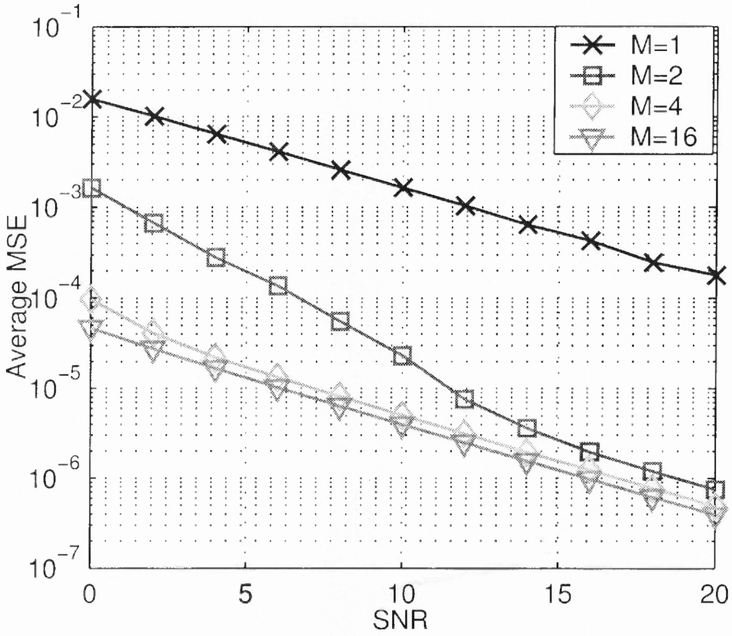

Figure 2.4 Average MSE of the ML estimator versus SNR.

Figure 2.4 shows the (average) MSE for different SNR values and $M = 1, 2, 4$ and 16. The curves for $M = 4$ and $M = 16$ are in excellent agreement with the curves in Figure 2.2. Thus, one can conclude, that in these scenarios the ML-estimator achieves the ACRB. Furthermore, for $M = 1$ and 2, the MLE provides a useful estimate of the angle of arrival, even though the expression of the ACRB (2.28) does not converge. This has been explained in Section 2.2.2. For high SNR values, the ACRB given in equation (2.28) can be approximated by neglecting the second summand containing $(2\sigma^2)^2$ in the enumerator. This approximated average Cramer Rao bound converges also for $M = 2$ and is in excellent agreement with the values of the MSE of the ML-DF simulations for $M = 2$ for high SNR values shown on the right hand side of Figure 2.4.

In summary, the (average) MSE for $M = 1$ is much larger than the one for $M = 4$ or $M = 16$. The transmit diversity provides a gain of more than 20dB in this respect in this AOA estimation scenario.

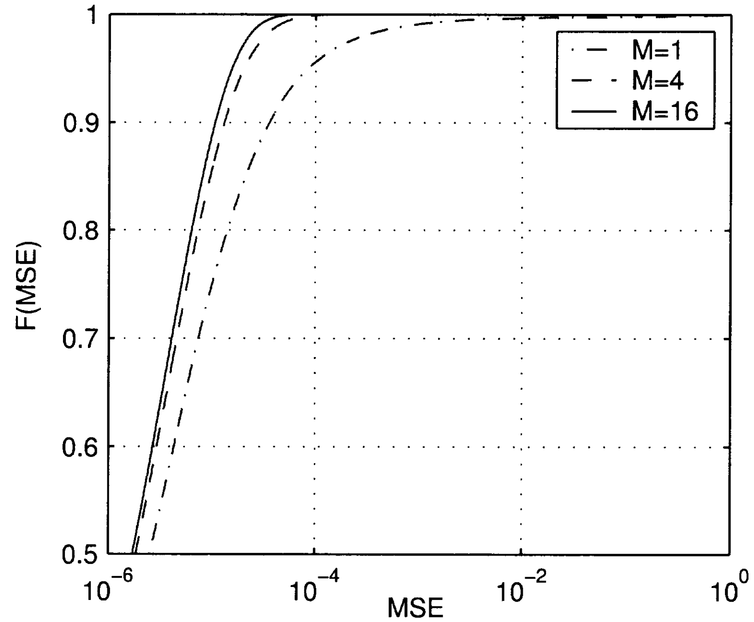

Figure 2.5 CDF of the instantenous error for $M = 1, 4, 16$ at $SNR = 10$dB.

In Figure 2.5 the Cumulative Density Function (CDF) of the instantenous squared error is shown for $M = 1, 4$ and 16 and a per snapshot SNR of 10dB. The Figure is included to illustrate the match between the outage CRB shown in Figure 2.3 and the instantenous squared errors of the ML-DF. For example, the 90 per cent percentile for $M = 1$ and 4 of the ML-DF in Figure 2.5 are in perfect agreement with the values of the outage CRB. For $M = 16$ some small deviation are present due to the limited simulation length.

Moreover, the CDF of the error of the ML-DF illustrates the idea behind using the outage CRB from another perspective. Figure 2.5 demonstrates that for $M = 1$ there is a non negligible chance of having a squared error of 10^{-1} or even 1. Assuming a stationary target, this implies that the RCS fluctuations might lead to a situation in which the target cannot be located effectively. For $M = 4$ and 16 the probability of such a large error is negligible. Thus, one may infer, that particularly for stationary or very slow moving targets, a comparison of different radar systems based solely on the average CRB or the average MSE is not sufficient. A complete evaluation of different systems has to take the slope of the squared error CDF into account. Since the outage CRB, $\mathrm{CRB}_{out=p}$, is a lower bound of the $1 - p$ percentile of any estimator, it is a valid approach to compare systems in this respect.

2.3.2 Correlated Target Aspects

This chapter is concluded by presenting simulation results for an extension of the previous model, which includes correlated target aspects. From Figure 1.1 it can be inferred, that for an insufficient angular separation between the illuminating antennas, the fading coefficients, which determine the returned signal powers from the different transmitters, are not independent. Referring to the signal model discussed in section 2.1, this section explores the scenario of non-orthogonal columns $\mathbf{g}_m$ of the matrix $\mathbf{G}$. The correlated fading coefficients are approximated with a first order AR process. For this purpose, the fading vector $\boldsymbol{\alpha}$ in the signal description in (2.19) is replaced with $\boldsymbol{\alpha}'$ which contains M consecutive samples of an AR process $u(k)$, where $u(k) - \rho \cdot u(k-1) = v(k)$ and $v(k)$ is a white process with variance $\sigma^2 = 1 - \rho^2$. Given that ρ is real, one finds that the correlation matrix $\mathrm{C}_{\alpha'}$ has the form

$$\mathrm{C}_{\alpha'} = \begin{pmatrix} 1 & \rho & \rho^2 & \cdots & \rho^{M-1} \\ \rho & 1 & \rho & & \\ \rho^2 & \rho & 1 & & \vdots \\ \vdots & & & \ddots & \\ \rho^{M-1} & & \cdots & & 1 \end{pmatrix}. \tag{2.34}$$

Using the Cholesky factorization, A can be found so that $\mathrm{A}^H\mathrm{A} = \mathrm{C}_{\alpha'}$. Thus, α' can be implemented by using the uncorrelated elements of α and deriving $\alpha' = \mathrm{A}^H\alpha$, as $\mathrm{C}_{\alpha'} = E\{\alpha'\alpha'^H\} = \mathrm{A}^H E\{\alpha\alpha^H\}\mathrm{A} = \mathrm{A}^H\mathrm{I}_M\mathrm{A}$.

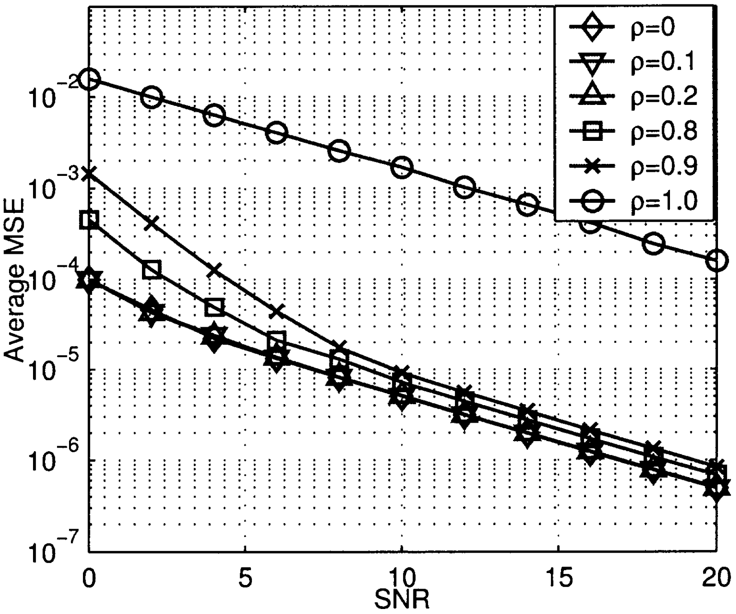

Figure 2.6 Average MSE for correlated target aspects and $M = 4$.

Figures 2.6 and 2.7 show simulation results for correlated target fading among the transmitter aspects for $M = 4$ and $M = 16$, respectively. As one would expect, for $\rho = 1$ the performance of the multiple transmitter scenarios degenerates to the one of a single transmitter as all transmitters illuminate actually the same aspect of the target[2]. This is

---

[2] Note, as for $\rho = 1$ the Cholesky factorization of $\mathrm{C}_{\alpha'}$ is not possible, the simulations have actually been conducted with $\rho = 1 - 10^{-8}$ instead of 1.

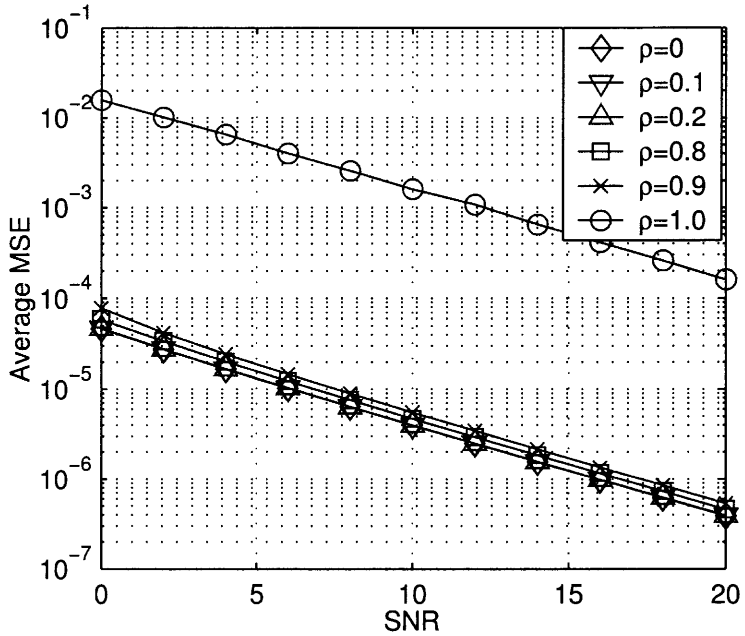

Figure 2.7 Average MSE for correlated target aspects and M=16.

evident when comparing Figures 2.6 and 2.7 with Figure 2.4. Further, the curves for $\rho = 0$ agree with the curves shown in Figure 2.4 for $M = 4$ and $M = 16$.

Further, one can see, that for $\rho = 0.9$ and $\rho = 0.8$ and $M = 4$ the progression of the curves in Figure 2.6 is similar to the one for $M = 2$ in Figure 2.4. This is expected, as the correlation between the different aspects prevents the full diversity gain. In contrast, the curve for $\rho = 0.9$ and $M = 16$ is very close to the curve for $\rho = 0$. This is because the two outer transmitters illuminate two aspects which are almost uncorrelated, $E\{\alpha_1\alpha_{16}^*\} < 0.2$. So in other words, full diversity is roughly achieved.

In summary, one can infer from the plots in Figures 2.6 and 2.7 that significant gains are possible by employing transmit diversity even when adjacent target aspects result in fading coefficients with correlation coefficients as large as 0.9. Moreover, the difference between the performances for small correlation coefficients, like $\rho = 0.2$, and actual orthogonal target aspects is negligible. Therefore, this section underlines again that MIMO radar with transmit diversity is a promising approach for real world radar systems.

CHAPTER 3

MIMO-RADAR DETECTION IN WHITE NOISE

In the previous chapter, the AOA estimation performance of MIMO–radar with transmit diversity has been discussed. In this chapter, the capabilities of MIMO–radar to detect targets in additive white Gaussian noise with known variance are explored. The discussion in this chapter is an extension of the work presented in [8].

3.1 Signal model

In this chapter, a MIMO–radar system is considered, which employs widely separated elements at both, the transmit and the receive side. A two–dimensional scenario is assumed, ignoring the heights of targets and radar elements. The location of each of the M transmitters is denoted as $\vec{T_k} = (x_k^t, y_k^t)$ and the location of each of the N receiver elements as $\vec{R_l} = (x_l^r, y_l^r)$. A target is again assumed to consist of Q scatterers, of which each has a location given by $\vec{X_q} = (x_q, y_q)$. This notation follows the one introduced in [29].

Introducing the propagation delay from the k-th transmitter to the q-th scatterer, $\tau_{tk}(\vec{X_q})$, and the one form the from the q-th scatterer to the l-th receiver element, $\tau_{rl}(\vec{X_q})$, the signal received by the n-th receive element due to the waveform transmitted by the k-th transmitter reflected via the q-th scatterer can be written as

$$r_{q,k,l}(t) = \frac{b_q(l,k)}{L_q(l,k)}\sqrt{\frac{E}{M}}s_k\big(t - \tau_{tk}(\vec{X_q}) - \tau_{rl}(\vec{X_q})\big) + n(t). \tag{3.1}$$

$b_q(l,k) = \zeta_q e^{-j2\pi f_c\left(\tau_{tk}(\vec{X_q})+\tau_{rl}(\vec{X_q})\right)}$ denotes the reflection coefficient of the q-th scatterer and the phase shift due to its position. $L_q(l,k)$ refers to the attenuation due to the pathloss of the two propagation paths and is discussed in the next section in detail. The delays

$\tau_{tk}(\vec{X}_q)$ and $\tau_{rl}(\vec{X}_q)$ can be easily derived as

$$\begin{aligned} \tau_{rl}(\vec{X}_q) \cdot c = d(\vec{R}_l, \vec{X}_q) &= \sqrt{(x_l^r - x_q)^2 - (y_l^r - y_q)^2} \\ \tau_{tk}(\vec{X}_q) \cdot c = d(\vec{T}_k, \vec{X}_q) &= \sqrt{(x_k^t - x_q)^2 - (y_k^t - y_q)^2}, \end{aligned} \tag{3.2}$$

where c refers to the speed of light. Similar to [8, 29], it is assumed here that the distances between the scatterers are negligible compared to the range resolution of the used bandwidth. In other words, the target extend does not lead to an observable frequency selectivity within the employed bandwidth. Accordingly, the delays in the argument of the baseband waveforms $s_k(t)$ are approximated as constant for all Q scatterers. Defining the center of the target or the center of the cell under test as $\vec{X}_0$, this approximation is expressed as $s_k\big(t - \tau_{tk}(\vec{X}_q) - \tau_{rl}(\vec{X}_q)\big) \approx s_k\big(t - \tau_{tk}(\vec{X}_0) - \tau_{rl}(\vec{X}_0)\big)$. Similarly, it is assumed that the path-losses for the scatterers are the same and determined by the target center, $L_q(l,k) \approx L_0(l,k)$. Figure 3.1 is illustrating the used notation and the introduced approximation.

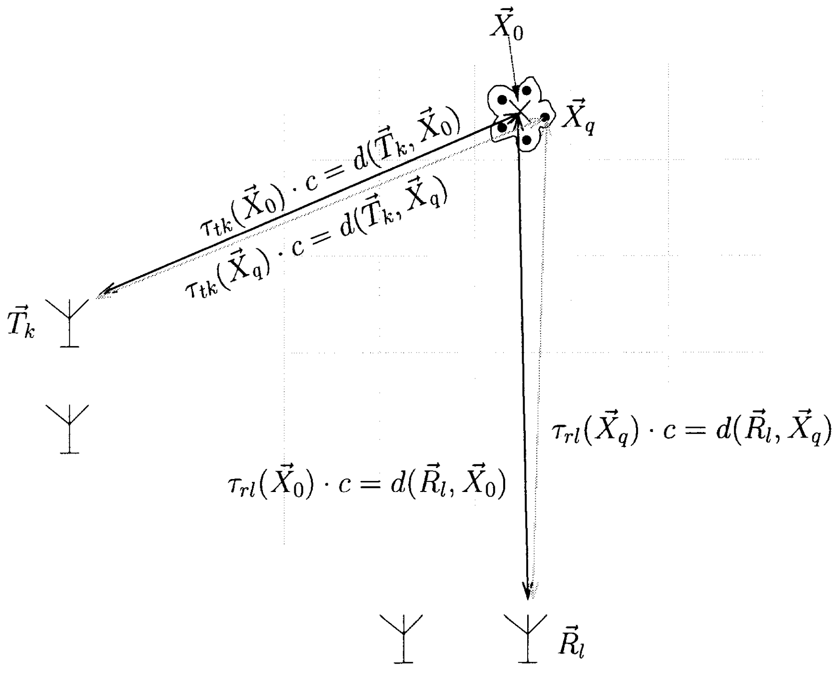

Figure 3.1 Overview over MIMO-radar detection with different test cells and extended targets.

It is emphasized, that the exact position of each scatterer maintains to have an impact on the complex scalar $b_q(l,k) = \zeta_q e^{-j2\pi f_c\left(\tau_{tk}(\vec{X}_q)+\tau_{rl}(\vec{X}_q)\right)}$. The signal received at the l-th receive element due to the waveform transmitted by the k-th transmitter can then be expressed as

$$r_{l,k}(t) = \frac{1}{L_0(l,k)} \underbrace{\sum_{q=0}^{Q-1} b_q(k,l) \cdot}_{h_{l,k}} \sqrt{\frac{E}{M}} s_k\big(t - \tau_{tk}(\vec{X}_0) - \tau_{rl}(\vec{X}_0)\big) + n(t). \tag{3.3}$$

In case the signals should be written in matrix notation, as in the previous chapter or in [8,29], $h_{l,k}$ is the element of the channel matrix $\mathbf{H}$ in the l-th row and the k-th column. Here, the matrix notation is not further pursuit. However, it is noted that the target aspect and in particular the target fading coefficient is determined by the complex sum $h_{l,k} = \sum_{q=0}^{Q-1} b_q(k,l)$. The total received signal at the l-th receive element including all the waveforms transmitted by M transmit elements can then be written as

$$r_l(t) = \sum_{k=0}^{M-1} \frac{h_{l,k}}{L_0(l,k)} \cdot \sqrt{\frac{E}{M}} s_k\big(t - \tau_{tk}(\vec{X}_0) - \tau_{rl}(\vec{X}_0)\big) + n(t). \tag{3.4}$$

Assuming that the waveforms $s_k(t)$ maintain very low cross correlation values or are orthogonal for a variety of different delays, the presence test is prepared by correlating each receive signal on the set of transmitted waveforms, which are delayed accordingly to the position of the cell under test (matched filtering for each waveform). This results in a vector for each receive element and cell under test given by

$$\begin{aligned} \mathbf{r}_l(\vec{X}_0) &= \int \mathbf{s}^*(t|\vec{X}_0, l) \cdot r_l(t)dt \\ &= \sqrt{\frac{E}{M}} \begin{pmatrix} \frac{h_{l,0}}{L_0(l,0)} \\ \vdots \\ \frac{h_{l,M-1}}{L_0(l,M-1)} \end{pmatrix} + \mathbf{v}_l, \end{aligned} \tag{3.5}$$

where $\mathbf{s}(t|\vec{X}_0, l)$ is given as $\mathbf{s}(t|\vec{X}_0, l) = \Big[s_0\big(t - \tau_{t0}(\vec{X}_0) - \tau_{rl}(\vec{X}_0)\big), \ldots, s_M\big(t - \tau_{t(M-1)}(\vec{X}_0) - \tau_{rl}(\vec{X}_0)\big)\Big]^T$ and $\mathbf{v}_n$ contains the noise samples, which are i.i.d. due to the approximately orthonormal transmit waveforms. The necessary properties of the transmit waveforms may be summarized as $\int s_k^*(t-\tau)s_{k'}(t)dt = \delta(\tau)\cdot\delta(k-k')$.

To further proceed preparing for the target presence test, the receive signal vectors of the N receivers, $\mathbf{r}_l(\vec{X}_0)$ are summarized in one vector $\mathbf{r}(\vec{X}_0) = [\mathbf{r}_0^T(\vec{X}_0), \ldots, \mathbf{r}_{N-1}^T(\vec{X}_0)]^T$.

In the previous chapter, a condition has been derived, which determines the minimum distance between transmit elements so that different target aspects are illuminated resulting in independent fading coefficients across the signal paths. Denoting with $d(\vec{T}_k, \vec{T}_{k'}) = \sqrt{(x_k^t - x_{k'}^t)^2 - (y_k^t - y_{k'}^t)^2}$ the distance between any pair of transmitters ($k \neq k'$) and with $d(\vec{R}_l, \vec{R}_{l'}) = \sqrt{(x_l^r - x_{l'}^r)^2 - (y_l^r - y_{l'}^r)^2}$ the distance between any pair of receiver elements, a new condition is introduced here, namely

$$
\begin{aligned}
d(\vec{R}_l, \vec{R}_{l'}) &\geq \frac{R\lambda}{D_{target}} \qquad \forall l \neq l' \qquad \text{or} \\
d(\vec{T}_k, \vec{T}_{k'}) &\geq \frac{R\lambda}{D_{target}} \qquad \forall k \neq k',
\end{aligned}
\tag{3.6}
$$

where D_{target} corresponds to the target's extend. This condition leads to uncorrelated fading coefficients, $h_{l,k}$, across the different signal paths. Similar to the previous chapter and [8], the $h_{l,k}$ are substituted with α_i. The received signal can then be written as

$$
\begin{aligned}
\mathbf{r} &= \sqrt{\frac{E}{M}}
\begin{pmatrix}
\frac{1}{L_0(0,0)} & 0 & \cdots & \cdots & \cdots & 0 \\
0 & \ddots & 0 & & & \vdots \\
\vdots & 0 & \frac{1}{L_0(0,M-1)} & & & \vdots \\
\vdots & & & \frac{1}{L_0(1,0)} & & \vdots \\
\vdots & & & & \ddots & 0 \\
0 & \cdots & \cdots & \cdots & 0 & \frac{1}{L_0(N-1,M-1)}
\end{pmatrix}
\begin{pmatrix}
h_{0,0} \\ \vdots \\ h_{0,M-1} \\ h_{1,0} \\ \vdots \\ h_{N-1,M-1}
\end{pmatrix}
+ \mathbf{v} \\
&= \sqrt{\frac{E}{M}}\mathbf{L}\boldsymbol{\alpha} + \mathbf{v},
\end{aligned}
\tag{3.7}
$$

where the matrix $\mathbf{L}$ is a diagonal matrix containing the different path-losses and the vector $\boldsymbol{\alpha}$ contains all the target fading coefficients which are under the above condition independent. The argument $\vec{X}_0$ is omitted from here on. However, it is emphasized that particularly the components of L depend on the position of the cell under test.

Furthermore, it is noted that the fading coefficient contained in $\boldsymbol{\alpha}$ are i.i.d. complex Gaussian random variables with unit power, thus $\boldsymbol{\alpha} \sim \mathcal{CN}(\mathbf{0}, \mathbf{I}_{MN})$. The noise terms are assumed to be mainly due to the thermal noise on the receive side. Thus, they are i.i.d. complex Gaussian as well, $\mathbf{v} \sim \mathcal{CN}(\mathbf{0}, \sigma^2\mathbf{I}_{MN})$.

To prepare for the comparison carried out in section 3.3, the signal model for a conventional radar, namely a phased array system, is included here. The reader is referred to the previous chapter or [8] for details. Path-losses are ignored in the discussion for conventional radar systems at the current stage. The signals transmitted by the transmit elements in a phased array system arrive at the target with roughly the same delay $\tau_t(\vec{X}_0)$, but different phases depending on the angle between the array and the direction of the cell under test. Furthermore, the signals reflected by the target arrive at the elements of the receive array also with roughly the same delay $\tau_r(\vec{X}_0)$ but different phases. Assuming, that the transmit array steers a beam in direction ϕ and denoting with ϕ_0 the direction of the cell under test from the transmit side and with θ_0 the direction of the cell under test from the receive array, the signal under H_1 hypothesis can be written as

$$\mathbf{r}(t) = \alpha\sqrt{\frac{E}{M}}\mathbf{a}(\theta_0)\mathbf{b}^H(\phi_0)\mathbf{b}(\phi)s\big(t - \tau_t(\vec{X}_0) - \tau_r(\vec{X}_0)\big) + \mathbf{n}(t). \tag{3.8}$$

It is assumed that the transmit beam is steered towards the cell under test, $\phi = \phi_0$. The presence test is prepared by steering the beam of the receive array towards the cell under test and correlating on the the appropriately delayed transmit waveform

$$\begin{aligned}
r &= \int_t \mathbf{a}^H(\theta_0)s^*(t|\vec{X}_0)\mathbf{r}(t)dt \\
&= \int_t \alpha\sqrt{\frac{E}{M}}\mathbf{a}^H(\theta_0)\mathbf{a}(\theta_0)\mathbf{b}^H(\phi)\mathbf{b}(\phi)s^*(t|\vec{X}_0)s\big(t-\tau_t(\vec{X}_0)-\tau_r(\vec{X}_0)\big)dt \\
&\quad + \int_t s^*(t|\vec{X}_0)\mathbf{a}^H(\theta_0)\mathbf{n}(t)dt \\
&= N\cdot M\alpha\sqrt{\frac{E}{M}}+n'. \qquad (3.9)
\end{aligned}$$

As the system observes a signle aspect of the target, the target's RCS fluctuations are represented by a single complex fading coefficient, $\alpha \sim \mathcal{CN}(0,1)$. Further, the n' is a single noise term with the distribution $\mathcal{CN}(0, N\sigma^2)$.

3.2 Diversity Detection with Different Attenuation among the Signal Paths

Given the MIMO signal model developed for a target presence test in the previous section, the detection performance is evaluated in this section for different path-losses across the signal paths. This is an important extension to the work presented in [8] where identical path-losses have been assumed. However, given that the transmit and receive elements have to be sufficiently separated to observe different target aspects for diversity, it is obvious that the free space attenuation for all paths cannot be constant for all possible cells under test.

For H_1 (target presence) and H_0 (target absence) hypotheses the received signal vector is given as

$$\mathbf{r} = \begin{cases} \sqrt{\frac{E}{M}}\mathbf{L}\boldsymbol{\alpha}+\mathbf{v} & H_1 \\ \mathbf{v} & H_0 \end{cases}. \qquad (3.10)$$

The likelihood test statistic for these signals is developed in Appendix B and is found to be

$$\eta = \sum_{i=0}^{MN-1} \frac{\frac{E}{M}\frac{1}{\sigma^4}L(i)^2}{1+\frac{E}{M}\frac{1}{\sigma^2}L(i)^2}|r(i)|^2 \underset{H_0}{\overset{H_1}{\gtrless}} \gamma. \tag{3.11}$$

$L(i)$ denotes the i-the element of the diagonal matrix $\mathbf{L}$. It is noted that the test statistic is a weighted sum of observations $|r(i)|^2$, $\eta = \sum_i w_i |r(i)|^2$. Furthermore, the weights depend on the geometry of the scenario which determines the different path-losses, as

$$L(i) = \frac{1}{L_0(\lfloor i/M \rfloor, (i \mod M))}. \tag{3.12}$$

Moreover, for high SNR ($\frac{E}{M\sigma^2} \gg 1$) the test statistic is roughly the same as the one ignoring the different ranges

$$\eta = \sum_{i=0}^{MN-1} \frac{\frac{E}{M}\frac{1}{\sigma^4}L(i)^2}{1+\frac{E}{M}\frac{1}{\sigma^2}L(i)^2}|r(i)|^2 \approx \frac{1}{\sigma^2}\sum_{i=0}^{MN-1}|r(i)|^2 \qquad \text{for } \frac{E}{M\sigma^2} \gg 1. \tag{3.13}$$

This test is discussed in [8]. It has to be noted, that the derived test statistic requires the knowledge of both, the received signal power E, which depends on the target's mean RCS, and the variance of the additive Gaussian noise σ^2. Finally, it is noted, that the test statistic incorporating the derived weights is not χ^2 distributed due to those weights. In contrast, when the different path-losses are constant the test statistic is χ^2 distributed under both hypothesis.

In the following the performance of a detector accounting for the different path-losses according to (3.11) is compared to the one of a detector assuming identical ones. The comparison is based on free space attenuation. Thus, the gains across the signal paths are given by

$$\frac{1}{L_0(l,k)} = \frac{1}{d(\vec{R}_l, \vec{X}_0)d(\vec{T}_k, \vec{X}_0)}. \tag{3.14}$$

It is worthwhile mentioning in this context, that the exponent 4 of the range in the standard radar equations, [5], is due to the propagation to *and* back from the target and not due to ground reflections as discussed for long range wireless communications in , e.g., [4].

The here presented simulation results are based on a scenario depictured in 3.2. Four receive and two transmit elements are considered. Further, ten possible target positions are evaluated, $\vec{X}_{0,1}, \ldots, \vec{X}_{0,10}$. It is noted that even though the targets are depictured as points, they are assumed to be complex thus having an aspect dependent RCS resulting in uncorrelated α_i.

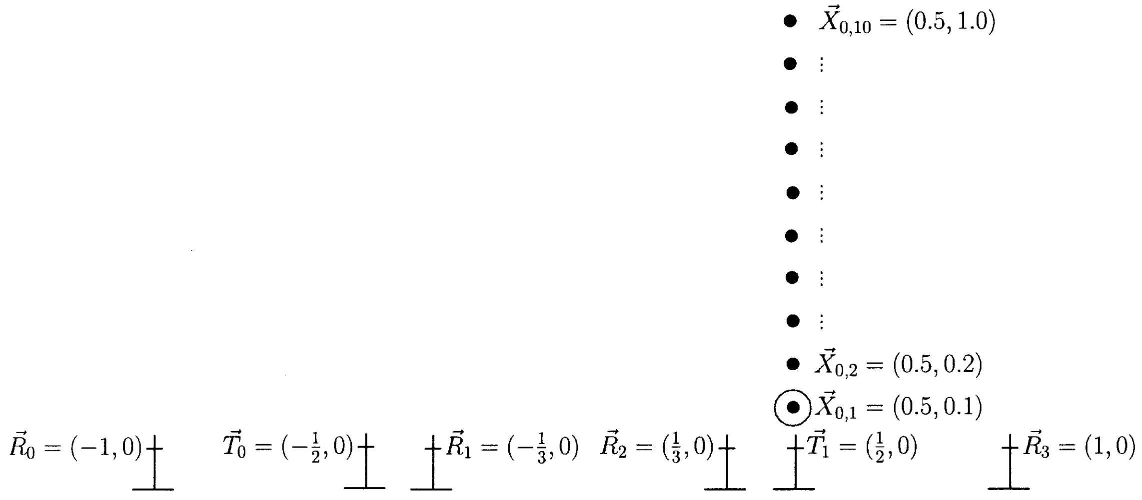

Figure 3.2 Illustration of receiver, transmitter and target locations used in the analysis.

As the aim of this section is to compare the effects of different weighting approaches in the test statistic and not to explore the system coverage, the effective received power is held constant by normalizing E according to

$$E' \cdot N = \sum_i L(i)^2 \frac{E}{M}, \tag{3.15}$$

where E' is the one used in the SNR context and E the in 3.7 etc. In other words, targets far away result in the same total receive power as targets close to the receive and transmit apertures. However, the amount each individual transmit-receive path contributes to the total receive power differs obviously for close by and far away targets. Further, this normalization applies to the *mean* total receive energy. The target still has random fading coefficients across all observed aspects.

As stated previously, deriving the weights for the test statistics given in (3.11) requires knowledge of the ratio $\frac{E}{\sigma^2}$. Further, according to (3.13) the weights for high SNR values tend to be uniform and a knowledge of the actual SNR is no longer required. In radar, it is impossible to know the SNR *prior* detection, as the mean signal energy depends on the target's mean RCS. As the target is to be detected in the first place, it is not feasible to assume to know the target's RCS. A simple approach to circumvent this deadlock is to derive the weights of the test statistic for a fixed assumed minimal SNR. As the following plots show a target can be called "detectable" for an SNR of roughly $\frac{E'}{\sigma^2} = 5\text{dB}$, this SNR value may be chosen to derive the weights of the test statistic.

Figures 3.3 and 3.4 show the probability of detection, P_D for different $\frac{E'}{\sigma^2}$ values and a false alarm rate of $P_{false} = 10^{-4}$. The first Figure is based on a single target location $\vec{X}_{0,1}$ marked in Figure 3.2 by a circle, whereas the second plot is based on an average over all ten possible target locations.

The solid line is based on an equal weight combining of the observations, ignoring the different gains over the transmission paths. The dashed line is based on an assumed fixed SNR of $\frac{E'}{\sigma^2} = 5\text{dB}$. The dotted line is based on a system which knows the actual ratio between returned target and noise power.

As expected, the equal gain combining leads to suboptimal performance but approaches the optimal (hypothetical) one for high SNR values. On the contrary, the approach based on weights calculated for an SNR of 5dB behaves for similar values as the optimal approach but leads to lower detection probabilities for higher SNR values. Thus, this approach can be used to enhance the detection for small targets of minimal detectable size at the expense of detection probability for big targets resulting in high SNR values.

However, comparing Figures 3.3 and 3.4, it is evident, that the different combining approaches differ only in performance in situations, where there is a strong bias in the

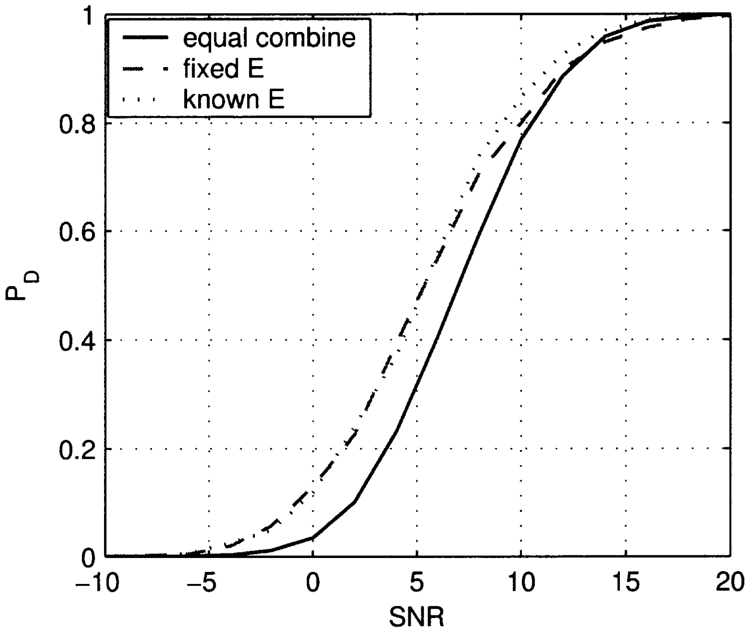

Figure 3.3 Detection probability versus SNR for different signal combine approaches and a single cell under test.

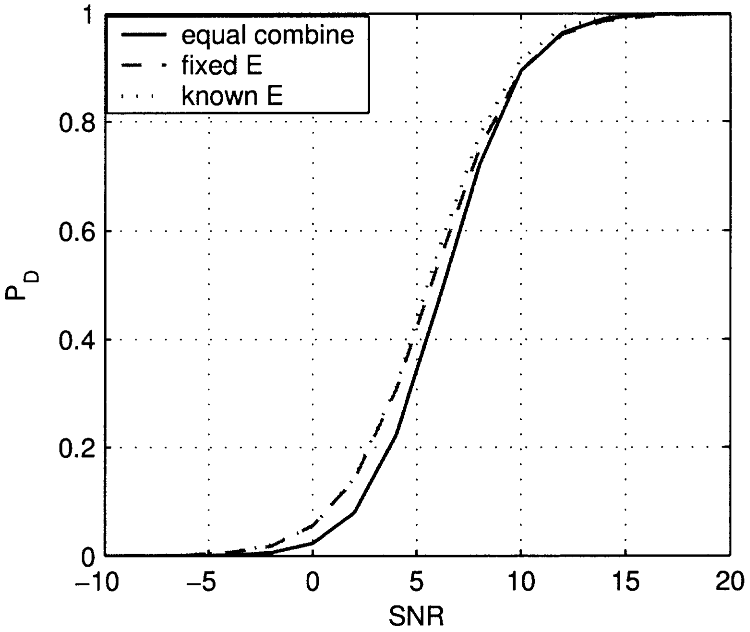

Figure 3.4 Detection probability versus SNR for different signal combine approaches, averaged over several cells under test.

signal gains (the target is close to a particular transmit-receive pair). Even in such situations the difference between the approaches is within the range of $1, 2$dB. Therefore, the exact geometry is in the further principal investigations ignored. However, the result of this analysis is motivating in the MIMO context, as it demonstrates that equal gain combining, though being suboptimal, leads in realistic scenarios to good results. Particularly in future research exploring constant false alarm detectors with neighbouring cell averaging similar to [6], this observation is important.

Finally, it is noted that the slope of the curves in Figure 3.4 is more steep than the one of the curves in 3.3. This is due to the fact that curves in 3.4 are based on situations with in the average stronger diversity than the single situation illustrated in 3.3. Indeed the target location $\vec{X}_{0,1}$ is from a diversity point of view degenerated as mainly the signal path from $\vec{T}_1$ via $\vec{X}_{0,1}$ to $\vec{R}_2$ contributes to the test statistic.

3.3 Detection in White Noise with Identical Path–Losses

The aim of this section, is to extend the observations concerning target detection in white noise presented in [8] to include correlated target aspects similar to what is done in the AOA chapter. Further, low SNR Receiver Operating Characteristics (ROC) are discussed to prepare a fundamental argument presented in the next section.

3.3.1 Uncorrelated Target Aspects

As discussed in the previous section, it can be argued to neglect the different range related gains in a MIMO-radar system for principal investigations. Accordingly, from here on $\mathrm{L} = \mathrm{I}_{MN}$ is assumed.

The test statistic for equal weights is then

$$\eta = \sum_{i=0}^{MN-1} |r(i)|^2 = |\mathbf{r}|^2 \underset{H_0}{\overset{H_1}{\gtrless}} \gamma. \tag{3.16}$$

Denoting with χ_K^2 a chi square distribution with K degrees of freedom the test statistic has then the following distributions

$$\eta \sim \begin{cases} \frac{1}{2}(\sigma^2 + \frac{E}{M})\chi_{2MN}^2 & H_1 \\ \frac{1}{2}\sigma^2\chi_{2MN}^2 & H_0 \end{cases}. \tag{3.17}$$

Accordingly, for any false alarm rate the following equality holds

$$\begin{aligned} P_{false} &= Pr(\eta \geq \gamma | H_0) = Pr(\chi_{2MN}^2 \geq \frac{2\gamma}{\sigma^2}) \\ &= 1 - F_{\chi_{2MN}^2}(\frac{2\gamma}{\sigma^2}), \end{aligned} \tag{3.18}$$

and the threshold γ can be found as

$$\gamma = \frac{\sigma^2}{2} F_{\chi_{2MN}^2}^{-1}(1 - P_{false}). \tag{3.19}$$

Given this threshold the detection probability is easily found as

$$\begin{aligned} P_D &= Pr(\eta \geq \gamma | H_1) = Pr\left(\chi_{2MN}^2 \geq \frac{2\gamma}{\sigma^2 + \frac{E}{M}}\right) \\ &= Pr\left(\chi_{2MN}^2 \geq \frac{\sigma^2}{\sigma^2 + \frac{E}{M}} F_{\chi_{2MN}^2}^{-1}(1 - P_{false})\right) \\ &= 1 - F_{\chi_{2MN}^2}\left(\frac{\sigma^2}{\sigma^2 + \frac{E}{M}} F_{\chi_{2MN}^2}^{-1}(1 - P_{false})\right). \end{aligned} \tag{3.20}$$

On the contrary, a phased array radar system operates after the beamforming (coherent processing) with the test statistic given by $\eta = |r|^2$, where r is given in equation (3.9). This test statistic has the following distribution

$$\eta \sim \begin{cases} \frac{1}{2}(N \cdot \sigma^2 + M \cdot N^2 \cdot E)\chi_2^2 & H_1 \\ \frac{1}{2}N \cdot \sigma^2\chi_2^2 & H_0 \end{cases}. \tag{3.21}$$

The threshold given the false alarm rate P_{false} is then found as

$$\gamma = \frac{N \cdot \sigma^2}{2} F_{\chi_2^2}^{-1}(1 - P_{false}), \tag{3.22}$$

and the detection probability is given by

$$\begin{aligned} P_D = Pr(\eta \geq \gamma | H_1) &= Pr\left(\chi_2^2 \geq \frac{2\gamma}{N \cdot \sigma^2 + E \cdot M \cdot N^2}\right) \\ &= 1 - F_{\chi_2^2}\left(\frac{\sigma^2}{\sigma^2 + E \cdot M \cdot N} F_{\chi_2^2}^{-1}\left(1 - P_{false}\right)\right). \end{aligned} \tag{3.23}$$

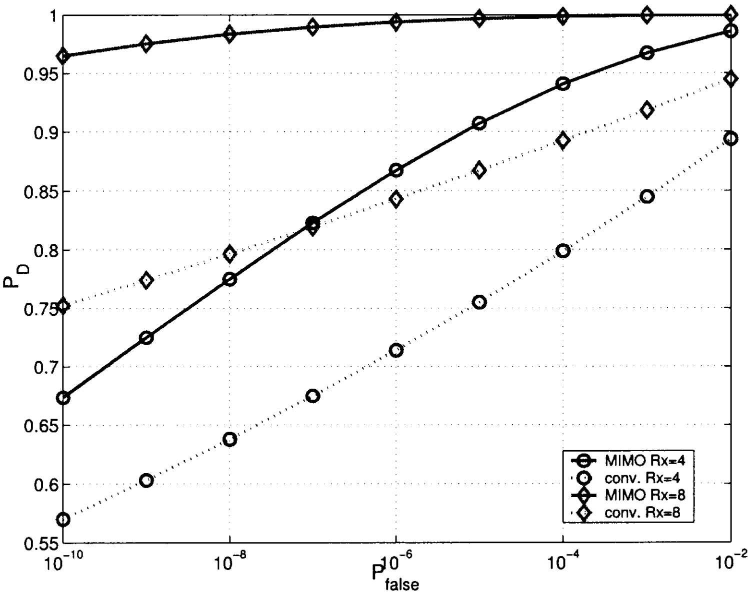

Figure 3.5 Receiver operating Chararacteristic for SNR $=$ 10dB for conventional and MIMO radars.

Figures 3.5 and 3.6 contain ROCs based on the expressions 3.20 and 3.23. The curves in both figures are based on either 1×4 or 1×8 systems operating either in MIMO or phased array mode, the latter is denoted as “conv.” in the figure legends.

The Figure 3.5 is based on an SNR of $\frac{E}{\sigma^2} = 10\text{dB}$ and Figure 3.6 on $\frac{E}{\sigma^2} = 5\text{dB}$. The two 1×4 curves in 3.5 can be found in [8]. Further, the curves in Figure 3.5 clearly revail the promiss of MIMO radar in target detection. The detection performance of the conventional coherent beamforming systems for high ratios between mean target return and interference power is limited by the target's fading RCS. MIMO-systems can capatilize on the non coherent diversity and thus “harden” the distribution of the target returned power around its mean. Therefore, the detection probabilities of MIMO radar are larger than the ones of conventional radar systems given high SNR values. In [8] and [29] this is further illustrated by plotting the logarithmic missed detection probability versus the SNR for a given false alarm rate.

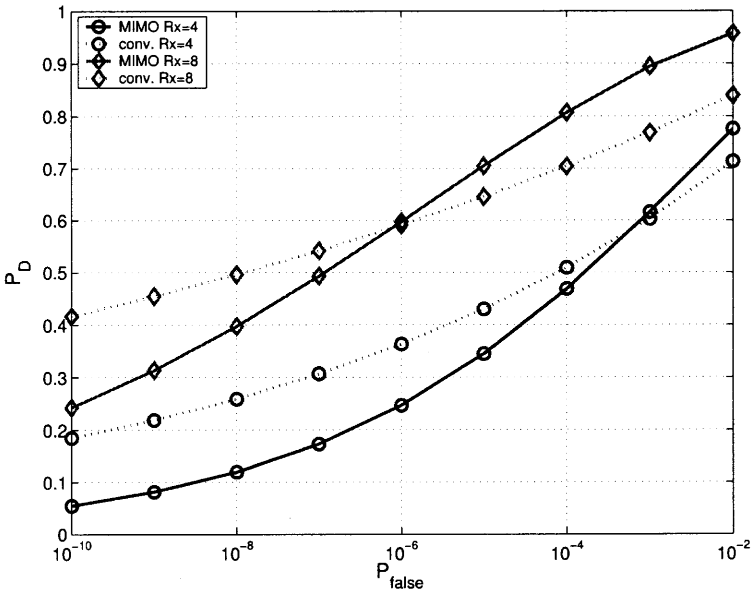

Figure 3.6 Receiver operating Chararacteristic for SNR $=$ 5dB for conventional and MIMO radars.

However, for relatively low SNR values, such as $\frac{E}{\sigma^2} =$ 5dB in Figure 3.6, this observation no longer holds. It is noted that this is due to the non-coherent nature of MIMO-radar detection. The reader is refered to [4, Chapter 3.5], where the difference between coherent and non-coherent communication via L diversity branches is discussed. Further, the next section is discussing the principal behaviour of MIMO radar detection in view of this important aspect.

3.3.2 Correlated Target Aspects

In this part of the dissertation, the impact of correlated target aspects is discussed similarly to the analysis of AOA estimation in the previous chapter. Again, it is noted that the correlation among the fading coefficient is due to a too small element separation on the transmit or receive side. For simplicity only $1 \times N$ systems are discussed. The elements of α are again assumed to be one realization of an 1st order AR process.

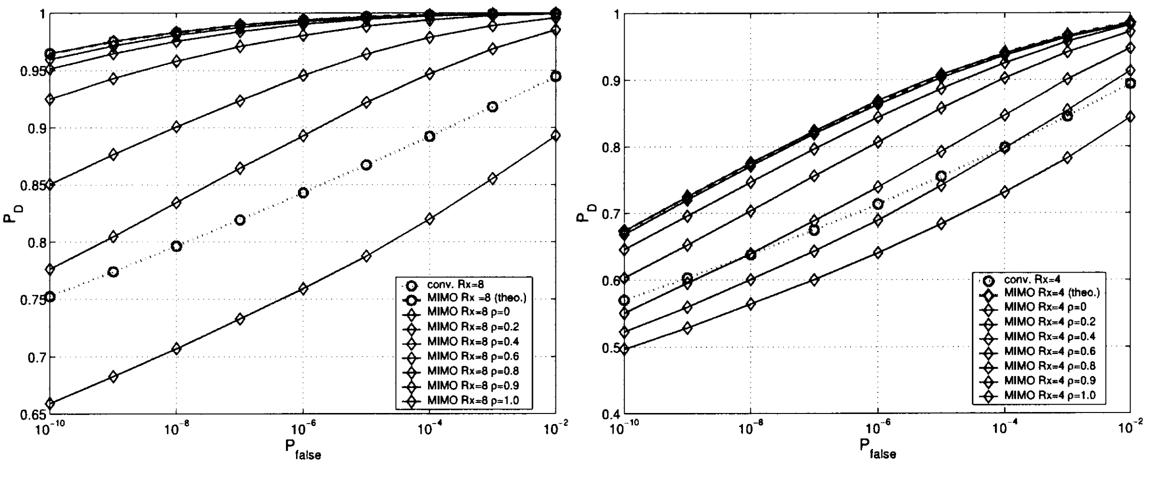

(a) Rx=8 (b) Rx=4

Figure 3.7 Receiver operating Chararacteristic for SNR $=$ 10dB with correlation among the target aspects.

Accordingly, the correlation matrix of α is given by

$$E\{\alpha\alpha^H\} = \mathbf{C}_\alpha = \begin{pmatrix} 1 & \rho & \rho^2 & \cdots & \rho^{M-1} \\ \rho & 1 & \rho & & \\ \rho^2 & \rho & 1 & & \vdots \\ \vdots & & & \ddots & \\ \rho^{M-1} & & \cdots & & 1 \end{pmatrix}, \tag{3.24}$$

and α can be derived as $\alpha \sim \mathbf{A}^H \mathcal{CN}(0, I_{MN})$, where $M = 1$ and $\mathbf{A}^H\mathbf{A} = \mathbf{C}_\alpha$. It is noted, that under H_0 the MIMO test statistic is again χ^2_{2N} distributed, but under H_1 it is no longer χ^2 distributed due to the correlation among the elements of α accordingly detection probabilities of the ROCs have to be based on Monte Carlo simulations.

Figures 3.7 and 3.8 contain ROCs for different values of ρ and an SNR of 10dB and 5dB, respectively. The ROCs for uncorrelated aspects in MIMO systems and for conventional phased array systems are plotted for comparison.

First, it is noted that, given an SNR of 10dB, for small correlation coefficients ρ the detection capabilities of MIMO radar are not impaired. However, once the correlation among the target's aspects approaches one, the detection performance of the MIMO approach is considerably degraded and even worse than the one of the conventional coherent approach. The reason for this is the fact that the diversity the MIMO system is aiming at is no longer given and as the MIMO system combines the observations non coherently it enhances the interferance requiring higher thresholds than the conventional system for a given false alarm rate.

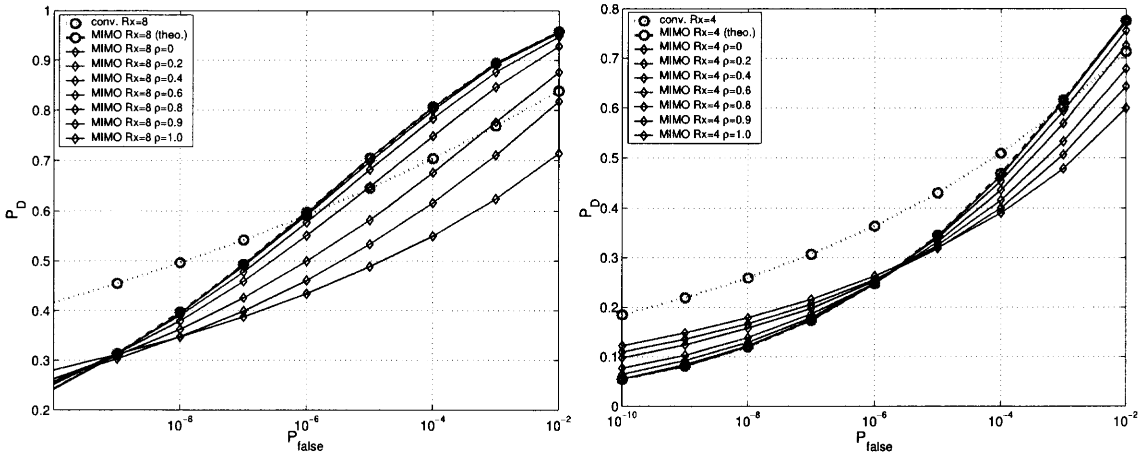

(a) Rx=8

(b) Rx=4

Figure 3.8 Receiver operating Chararacteristic for SNR $=$ 5dB with correlation among the target aspects.

Second, regarding the ROCs for an SNR of 5dB it is emphasized once again, that the MIMO approach cannot enjoy the benefits of diversity for low SNRs and thus is outperformed by the conventional approach. However, it is interesting to observe that for low false alarm rates and accordingly high thresholds the MIMO system's performance improves with increasing correlation coefficients. This is due to the fact that for high thresholds and small target returns it is possible to gain from the target's RCS fluctuations to exceed the thresholds with some probability. Thus, the "hardening" of the signal distribution due to diversity is contra-productive in such cases. However, as this results only in very small detection probabilities, it is very doubtful, if this observation has any practical implications.

3.4 Combining Diversity with Coherent Processing Gain: Hybrid Systems

In the previous section it is explored that for low SNR values MIMO systems are outperformed by conventional ones, as the first have to work non-coherently in contrast to the second which operate coherently with phased arrays. In this section is reiterated and put in the context of scenarios normally found in radar.

It has to be emphasized that the signal to noise or better signal to interference ratio in radar is a difficult design parameter. To assume just a more or less high SNR or SINR can be very misleading. First of all, the mean power of the signal component depends evidently on the target's size determining its mean RCS. A radar system normally has to cope with a variety of possible target sizes. Second, the clutter return contributes considerably to the noise or interference power. Moving target detection in clutter presence with Doppler processing is discussed in the next chapter. However, here it is noted, that the signal to clutter ratio cannot be controlled by increasing the transmit power. It has to be improved by Doppler processing, limiting the size of a competing clutter cell by beamforming, or a combination of both depending on the scenario.

It is possible to develop based on the radar equations for a clutter dominated environment found in [5] an analysis for target to clutter ratios found in a given scenario. However, the derived SNR values would be valid only for this particular scenario. Instead the reader is here asked to remember the size of directive antennas found in radar and compare it to the used wavelength. Assuming an inter element spacing of roughly $\lambda/2$ it is obvious that the commonly used antennas are equivalent to phased arrays with a few tens of elements. Accordingly, it can be argued that the coherent processing over several elements is normally necessary to improve the effective SNR to a certain value enabling detection.

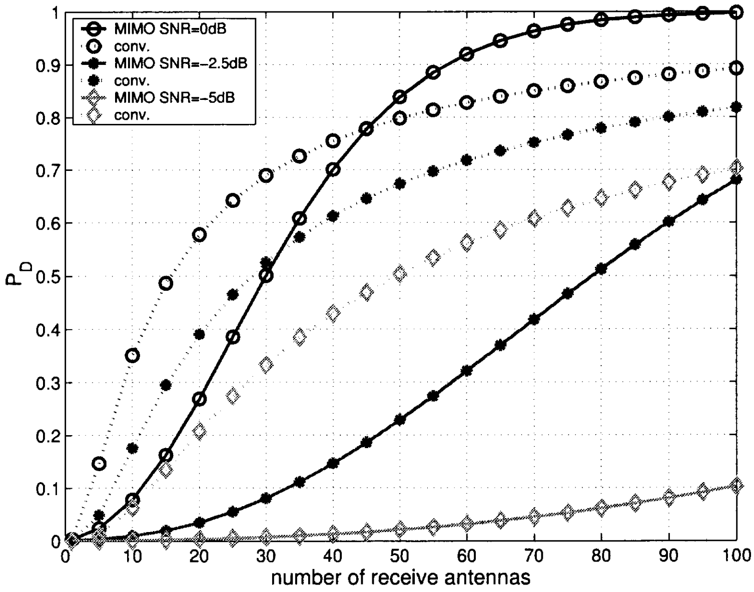

Figure 3.9 Detection probability versus number of receive elements for different SNRs.

Following the argument developed above the it is now explored how many array elements are necessary for a $1 \times N$ system with a fading target given a low initial SNR. Figure 3.9 illustrates the detection performance versus the number of receive elements N for a false alarm rate of $P_{false} = 10^{-6}$ based on the expressions 3.20 and 3.23, respectively. The MIMO system enjoys diversity, but needs to operate non-coherently therefore. It is observed that increasing the number of elements in the conventional phased array system first improves the detection probability fast until a saturation point is reached. This saturation point is due to that ones the effective SNR is good enough the target fading dominates the detection performance. On the contrary, the MIMO system's detection probability improves slower with an increasing number of antennas, but does not reach a saturation. However, it is emphasized that for a very low SNR of -5dB relating to a very small target the MIMO system effectively fails to work in contrast to the conventional system.

It is reiterated, that the diversity enjoyed by the MIMO approach results for high SNR values in an improved detection probability as the chances of a vanishing target return are limited. However, this improvement is achieved by sacrificing the coherent processing gain. This decreases the detection probability for low SNR values related to small targets. In other words, MIMO-radar detects big targets more reliable at the expense of detecting small targets.

Given this argument and the observations derived from Figure 3.9, it is apparent, that under realistic considerations a trade off between the amount to which diversity is achieved and the improvement in effective SNR due to coherent processing can be attractive. For example, a 1 × N system can consist of N_{div} subarrays on the receive side each of which consists of N_{coh} individual elements. The total number of elements is $N = N_{coh} \cdot N_{div}$. Each subarray stears a beam towards the cell under test resulting in a processing gain of N_{coh} and the signals from the N_{div} subarrays, which are sufficiently separated in space, are combined non-coherently to achieve diversity. The same is possible on the transmit side with $M = M_{coh} \cdot M_{div}$. Such a system may be called a hybrid system.

The false alarm rate of such a system can be derived as

$$\begin{aligned} P_{false} &= Pr\big(\chi^2_{2M_{div}N_{div}} \geq \frac{2\gamma}{N_{coh}\sigma^2}\big) \\ &= 1 - F_{\chi^2_{2M_{div}N_{div}}}\big(\frac{2\gamma}{N_{coh}\sigma^2}\big), \end{aligned} \tag{3.25}$$

and the detection probability as

$$\begin{aligned} P_D &= Pr\left(\chi^2_{2M_{div}N_{div}} \geq \frac{2\gamma}{N_{coh}\sigma^2 + M_{coh}N^2_{coh}\frac{E}{M_{div}}}\right) \\ &= Pr\left(\chi^2_{2M_{div}N_{div}} \geq \frac{N_{coh}\sigma^2}{N_{coh}\sigma^2 + N^2_{coh}M_{coh}\frac{E}{M_{div}}} F^{-1}_{\chi^2_{2M_{div}N_{div}}}\big(1 - P_{false}\big)\right) \\ &= 1 - F_{\chi^2_{2M_{div}N_{div}}}\left(\frac{\sigma^2}{\sigma^2 + N_{coh}M_{coh}\frac{E}{M_{div}}} F^{-1}_{\chi^2_{2M_{div}N_{div}}}\big(1 - P_{false}\big)\right). \end{aligned} \tag{3.26}$$

Figure 3.10 presents the detection probability derived with these expressions for a false alarm rate of $P_{false} = 10^{-6}$, $M = 1$ and $N = 64$ or $N = 16$. For each value of N three systems are considered. One achieves full diversity, $N = N_{div}$, one which maximizes the coherent processing gain, $N = N_{coh}$, and one which uses 4 subarrays of 4 or 16 elements, $N_{div} = 4$ and $N_{coh} = 4$ or $N_{coh} = 16$.

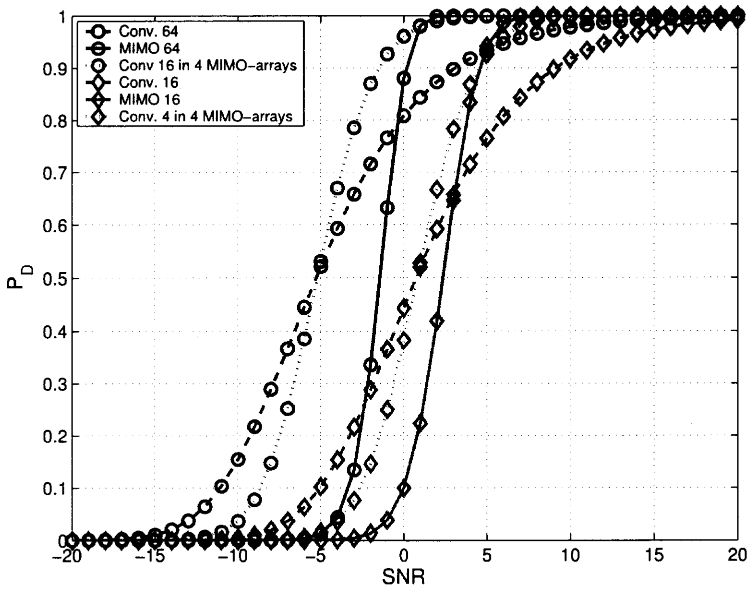

Figure 3.10 Detection probability versus SNR for MIMO, conventional and hybrid systems.

The hybrid approach using only 4 complex diversity branches bridges successfully between the two other systems. Its detection performance for low SNR values is roughly as good as the one of the fully coherent system and for high SNR values it still features enough diversity to compete with the system enjoying full diversity.

It is noted, that from here on again only systems with full diversity are compared with the ones operating completely coherent with a limited number of elements. However, it is obvious that the considered high SNR values can be achieved by replacing the each of the few elements with a coherently operated subarray.

CHAPTER 4

DETECTION OF MOVING TARGETS IN HOMOGENEOUS CLUTTER

One aim of this chapter is to establish the idea, that an assumed random direction of a moving target impairs the performance of a conventional phased array moving target detection radar on a similar way the RCS fluctuations do. In radar, it is commonly distinguished between the returns of (moving) objects of interest and the ones due to the omnipresent clutter by the frequency shifts of the returned signals. Clutter, such as the sea-surface or wooden hills, leads to only small frequency shifts, whereas the target's radial movement results in larger frequency shifts. Therefore, in Moving Target Indication (MTI) delay lines are employed to attenuate the DC components of the received signal pre detection [5]. Space Time Adaptive Processing (STAP) employed in airborne radars uses the inversion of an estimated clutter covariance matrix[1] to "whiten" the received signal or, in other words, attenuate the clutter returns.

Assuming that a target has a given speed |v| and a random movement direction Ω, e.g. uniformly distributed over $[0, 2\pi]$, the targets velocity components in x and y direction are given by

$$\begin{aligned} v_x &= |v| \cos \Omega \\ v_y &= |v| \sin \Omega. \end{aligned} \tag{4.1}$$

Further assuming, that the conventional radar transmit and receive array illuminates and observes the target along the x-axis, there is a certain probability that the radial velocity component, v_x, is small leading to a small Doppler shift and therefore attenuation of

---

[1] Note, that clutter in STAP is described in spatial and Doppler domain, whereas in this publication we assume stationary radar elements and spatial homogenous clutter and thus the later introduced covariance matrix only contains the Doppler characteristic of the clutter.

the target's reflection. Thus, the target cannot be distinguished from the clutter and can therefore not be detected.

In [13], it is argued that multi-static radar systems are capable of circumventing this obstacle, as they observe a target from different aspects and the target cannot have vanishing velocity components towards all of these aspects. However, in [13] no definite results are provided. Further, regular multi-static systems can be distinguished from MIMO systems, as the first commonly process the received signals in a distributed manner and fuse the results in a central station, whereas the later process all signals jointly in the central entity. This chapter illustrates, that MIMO systems outperform the multi-static ones because of information losses in the distributed processing.

It has to be noted, that multi-static systems do not necessarly employ decision fusion, and that MIMO–systems can be viewed as a group of particular multi–static systems. However, as most of the literature on multi–static detection is concerned with decision fusion, e.g. [13,30,31,32], in the subsequent, systems using decision fusion are referred to as multi–static systems.

In this chapter, a simple scenario with fixed radar stations surveying a 2-dimensional space is assumed. This space contains a homogenous clutter medium, such as a sea surface or wooden ground, whose second order statistics are assumed to be known or to be estimated. It is shown in this chapter and Appendix C, that detectors using an estimate of the clutter covariance matrix lead to Constant False Alarm Rate (CFAR). The radar systems try to detect the presence of a target with unknown 2-dimensional velocity in a given cell under test. The radar systems try to detect the presence of a target with unknown 2-dimensional velocity in a given range cell under test. It is noted, that in x and y direction range cells are defined according to the previous chapter. For simplicity, only one cell is considered subsequently. Therefore, the dependencies of the signals on the coordinates of this cell can be omitted.

4.1 Signal Models

In this section, the signal models for the different radar systems considered in this chapter are developed. The signal models are based on the same physical model. However, two separate models are developed; one for MIMO and multi-static radar and one for conventional phased array radar, which differ in some details to ease the derivation of the detectors in the next section.

It has to be noted here that the subsequent developed signal models differ from the ones used in the previous chapters:

1. The transmit power per transmitter element is no longer normalized by the number of transmitter elements to maintain a constant total transmit energy.
2. For notational simplicity, the energy per transmitter element is assumed to be one 1.

Particularly the implications of the first point are discussed in Section 4.3.3.

4.1.1 MIMO and Multi-Static Signal Model

It is assumed in this chapter, that the target does not leave the above mentioned range cell during K consecutive pulse transmissions. Furthermore, it is assumed that the M transmit elements employ pulse waveforms, which maintain approximately orthogonality under a variety of mutual delays and frequency shifts. This allows the receive elements to separate between the pulses transmitted by the different transmit elements. Under the H_1 hypothesis (target presence in the cell under test) and the H_0 hypothesis (target absence) respectively, the K consecutive signal samples at the l-th receiver due the pulses from the k-transmitter are given by

$$\mathbf{r}_{k,l} = \begin{cases} \mathbf{c}_{k,l} + \mathbf{n}_{k,l} & H_0 \\ \alpha_{k,l} \cdot \mathbf{d}_{k,l}(v_x, v_y) + \mathbf{c}_{k,l} + \mathbf{n}_{k,l} & H_1. \end{cases} \tag{4.2}$$

The scalar $\alpha_{k,l}$ represents the fading coefficient due to the targets RCS fluctuations across different aspects, which are assumed to be independent complex Gaussian random variables and constant during the K consecutive scans. This is equivalent to a Swerling case 1 model. It is noted, that first in contrast to the previous chapters the transmit power is not normalized with the number of transmit antennas M in this chapter. Further, the square root of the transmit energy E is from here on incorporated in the $\alpha_{k,l}$ terms to achieve a concise notation without loosing any insight.

The vector $\mathbf{d}_{k,l}(v_x, v_y)$ represents the changes in phase of the K samples due to the targets movement and has the form

$$\mathbf{d}_{k,l}(v_x, v_y) = \begin{pmatrix} 1 \\ e^{j2\pi f_{k,l} k T_{PRF}} \\ \vdots \\ e^{j2\pi f_{k,l}(K-1)T_{\mathrm{PRF}}} \end{pmatrix}, \tag{4.3}$$

where $T_{\mathrm{PRF}} = \frac{1}{\mathrm{PRF}}$ is the time between scans given by the Pulse Repetition Frequency (PRF). The Doppler shift $f_{k,l}$ observed at the l-th receiver is given by

$$f_{k,l} = (\cos(\theta_k^t) + \cos(\theta_l^r))\frac{f_c v_x}{c} + (\sin(\theta_k^t) + \sin(\theta_l^r))\frac{f_c v_y}{c}. \tag{4.4}$$

Here, f_c is the carrier frequency, c the speed of light. The transmit and receive elements are located at θ_l^t and θ_k^r, respectively. Figure 4.1 illustrates the geometry of this scenario. In (4.2), $\mathbf{c}_{k,l}$ represents the clutter return and $\mathbf{n}_{k,l}$ the thermal noise at the receivers. We assume the clutter to be Gaussian distributed with the following properties:

$$E\{\mathbf{c}_{k,l}\mathbf{c}_{k,l}^H\} = \mathbf{C}' \tag{4.5}$$

$$E\{\mathbf{c}_{k,l}\mathbf{c}_{k',l'}^H\} = \mathbf{0}_{K\times K} \qquad \forall k \neq k' \text{ or } l \neq l' \tag{4.6}$$

The clutter correlation matrix $\mathbf{C}'$ is discussed in a later paragraph of this section. The thermal noise at the receive elements is assumed to be white Gaussian noise with the correlation matrix $E\{\mathbf{n}_{k,l}\mathbf{n}_{k,l}^H\} = \sigma_n^2\mathbf{I}_{K\times K}$.

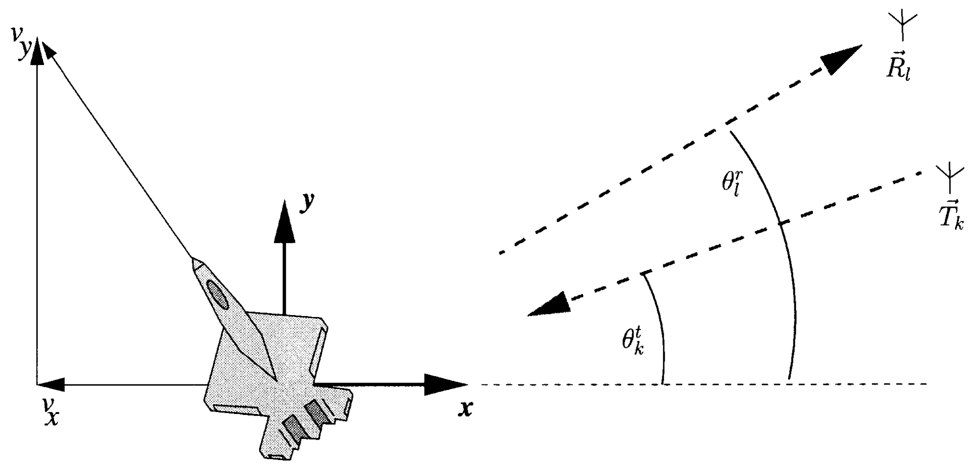

Figure 4.1 Location of transmitter and receivers in respect to target and its movement.

In the signal model above, eventual different path losses between the different transmitter and receiver pairs are ignored for simplicity. Thus, it is assumed, that all transmitters and receivers have roughly the same distance to the cell under test, but view this cell from different angles θ_k^t and θ_l^r. In this context, it is convenient to rewrite the expression (4.4) for the Doppler frequency observed by each transmit receive pair in the following way

$$\begin{aligned} f_{k,l} &= (\cos(\theta_k^t) + \cos(\theta_l^r))\frac{f_c v_x}{c} + (\sin(\theta_k^t) + \sin(\theta_l^r)\frac{f_c v_y}{c} \\ &= \frac{2f_c}{c}\vec{v} \cdot \vec{u} = \frac{2f_c|\vec{v}|}{c}\cos(\phi_{k,l}^{bs})\cos\left(\frac{\theta_k^t - \theta_l^r}{2}\right). \end{aligned} \tag{4.7}$$

The term $\vec{v} \cdot \vec{u}$ denotes the vector product and the vector $\vec{u}$ relates to the bistatic bisector as discussed in [33]. Figure 4.2 illustrates the geometry of the situation. The reader is asked to note, that $|\vec{u}| = \cos\left((\theta_k^t - \theta_l^r)/2\right)$.

As equation (4.7) and Figure 4.2 show, for a given speed the magnitude of the observed Doppler shift depends on one hand on the angle, $\phi_{k,l}^{bs}$ between the target's velocity vector $\vec{v}$ and the bistatic bisector, as the velocity vector is projected onto the bistatic bisector, and on the other hand on the angle between the transmit and receive pair. Spatial diversity in respect to the random movement diversity is achieved in MIMO radar by operating with several bistatic bisectors and thus ensuring, that eventually one is almost

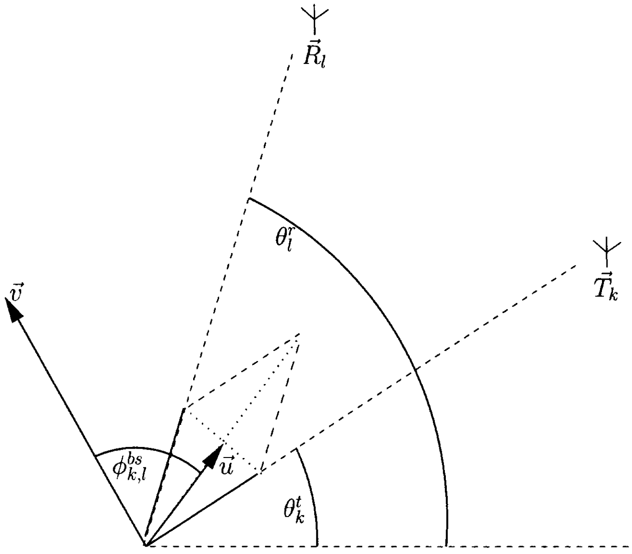

Figure 4.2 Illustration of the bistatic bisector and its impact.

aligned with the target's direction (small $\phi_{k,l}^{bs}$) resulting in a large Doppler shift. However, at the same time the difference between the transmitter aspect θ_k^t and the receiver aspect θ_l^r should be maintained small to observe a large Doppler shift, which allows to separate between target and clutter return. Therefore, it is advantageous to distribute *both*, the transmitter and receiver elements, in a similar way in space. This leads to diversity in respect to the target's movement *and* limits the difference between θ_l^r and θ_k^t. In a latter section a numerical example is illustrating this.

4.1.2 Phased Array Signal Model

For comparison with conventional radar systems, this chapter also considers a radar consisting of N receiver elements forming a linear array with small inter element spacing and M transmitter elements also having small interelement spacing and steering a beam into the direction ϕ_{steer}. The reader is asked to note, that similar to [8] and Chapter 3 the transmitter elements do not use different orthogonal pulse waveforms, but impose phase shifts $b_k(\phi_{\text{steer}})$ to the transmit pulses to steer the beam towards the direction ϕ_{steer}. The received signals at the l-th array element are

$$\mathbf{r}_l = \begin{cases} \sum_{k=1}^{M} \mathbf{c}_{k,l} b_k(\phi_{\text{steer}}) + \mathbf{n}_l & H_0 \\ \sum_{k=1}^{M} \Big(a_l(\phi_t) \cdot \alpha \cdot \mathbf{d}(v_x, v_y) b_k^*(\phi_t) & \\ \quad + \mathbf{c}_{k,l} \Big) b_k(\phi_{\text{steer}}) + \mathbf{n}_l & H_1. \end{cases} \tag{4.8}$$

Here, the fading coefficient, α, is the same for all elements, as they view the same RCS aspect of the target. Further, the vector $\mathbf{d}(v_x, v_y)$ is the same across all elements as they have the same perspective on the target's movements. The angle of arrival, ϕ_t, of the target return results in the phase shifts across the receive array elements given by $a_l(\phi_t) = e^{\jmath l 2\pi \cos(\phi_t)\Delta_r/\lambda}$, where Δ_r is the inter element spacing on receive side and λ the considered wavelength. Furthermore, the target's orientation towards the transmitter array results in phase shifts of impinging pulses given by $b_k(\phi_t) = e^{\jmath 2k\pi \cos(\phi_t)\Delta_t/\lambda}$, where Δ_t is the inter element spacing on the transmit side. The clutter and noise components have the same properties as described above. In particular, the independence between clutter returns at different transmitter–receiver–pairs applies here, too:

$$E\{\mathbf{c}_{k,l}\mathbf{c}_{k',l'}^H\} = 0_{K\times K} \qquad \forall k \neq k' \text{ or } l \neq l' \tag{4.9}$$

This may be surprising at first. However, considering, that the clutter return is due to a large number of small scatters distributed uniformly in a circle around the receive elements, one may realize the similarity of this situation to the Rayleigh fading channel model commonly used in mobile communications. It is a well established observation in communications, that the fading coefficients de-correlate over a distance of roughly $\frac{\lambda}{2}$, [34]. Thus, if one equates the clutter return path with the multi path communication models, one can expect, that the clutter returns are decorrelated for different receiver–transmitter–pairs. Further, in the next section a beamformer towards the cell under test is introduced at the receiver. This beamformer results in a processing gain, which equals the processing gain described by the signal to interference ratio for clutter dominated scenarios found in [5].

4.1.3 The Clutter Correlation Matrix

The clutter correlation matrix can have a variety of forms. In most of this chapter, it is assumed, that the clutter correlation matrix is known or estimated. Further, a homogenous clutter uniformly distributed in space is assumed. This could relate to sea surface, wooden ground with wind or chaff. In [5] and [35] the correlation of such clutter is described with a Power Spectral Density (PSD):

$$S_{cc}(f) = \frac{P_{cc}\lambda}{\sqrt{2\pi}2\sigma_v} e^{-\frac{f^2\lambda^2}{8\sigma_v^2}} \tag{4.10}$$

This relates to a continuous Auto Correlation Function (ACF) of

$$\begin{aligned} \varphi_{cc}(\tau) &= \int_{-\infty}^{\infty} \frac{P_{cc}\lambda}{\sqrt{2\pi}2\sigma_v} e^{-\frac{f^2\lambda^2}{8\sigma_v^2}} e^{j2\pi f\tau} df && (4.11) \\ &= P_{cc} e^{-\pi^2\tau^2 8\frac{\sigma_v^2}{\lambda^2}}. && (4.12) \end{aligned}$$

Sampling this ACF at the PRF one finds the correlation coefficients $\rho_{cc}(k)$ of consecutive samples, $\rho_{cc}(k) = \varphi_{cc}(kT_{RPF})$. The clutter correlation matrix is then given as

$$\mathbf{C}' = \begin{pmatrix} \rho_{cc}(0) & \rho_{cc}(1) & \cdots & \rho_{cc}(K-1) \\ \rho_{cc}(1) & \rho_{cc}(0) & & \vdots \\ \vdots & & \ddots & \rho_{cc}(1) \\ \rho_{cc}(K-1) & \cdots & \rho_{cc}(1) & \rho_{cc}(0) \end{pmatrix} \tag{4.13}$$

In the following sections the thermal noise and the clutter return are summarized as $\mathbf{x}_{k,l} = \mathbf{c}_{k,l} + \mathbf{n}_{k,l}$ for conciseness. The correlation matrix of $\mathbf{x}_{k,l}$ is then $\mathbf{C} = E\{\mathbf{x}_{k,l}\mathbf{x}_{k,l}^H\} = \mathbf{C}' + \sigma_n^2 \mathbf{I}_{K\times K}$.

4.2 The Moving Target Detectors

Using the signal models defined in (4.2) and (4.8), the detectors for the different schemes are derived based upon the Generalized Likelihood Ratio Test (GLRT) in this section. It is assumed throughout this chapter that in a cell under test is either one target with a velocity vector $\vec{v} = [v_x, v_y]^T$ or no target at all. Therefore, the veloctiy vector can be treated as an unknown deterministic parameter. Note, that even though in the numerical evaluations of the detectors this vector is implemented as a random variable, it would be unrealistic to assume to know the probability distribution funtion of the target's velocity and to derive a detector based on it.

4.2.1 The MIMO Moving Target Detector

Summarizing the MN received vectors $\mathbf{r}_i$ in one vector $\mathbf{r} = [\mathbf{r}_{1,1}^T, \ldots, \mathbf{r}_{M,N}^T]^T$ and the MN fading coefficients $\alpha_{k,l}$ in the vector $\boldsymbol{\alpha} = [\alpha_{1,1}, \ldots, \alpha_{M,N}]^T$, the joint densities of the received vectors conditioned on the hypotheses and parameters can be written as

$$\begin{aligned} f(\mathbf{r}|\boldsymbol{\alpha}, v_x, v_y, H_1) &= \prod_{k=1}^{M}\prod_{l=1}^{N} \frac{1}{\pi^K \sqrt{\det\{\mathbf{C}\}}} \\ &\quad \cdot e^{-\left(\mathbf{r}_{k,l}-\alpha_{k,l}\mathbf{d}_{k,l}(v_x,v_y)\right)^H \mathbf{C}^{-1}\left(\mathbf{r}_{k,l}-\alpha_{k,l}\mathbf{d}_{k,l}(v_x,v_y)\right)} \\ f(\mathbf{r}|H_0) &= \prod_{k=1}^{M}\prod_{l=1}^{N} \frac{1}{\pi^K \sqrt{\det\{\mathbf{C}\}}} e^{-\mathbf{r}_{k,l}^H \mathbf{C}^{-1}\mathbf{r}_{k,l}}, \end{aligned} \tag{4.14}$$

where $\mathbf{C} = \mathbf{C}' + \sigma_n^2 \mathbf{I}_{K\times K}$ is used. The GLRT is then defined as, [36],

$$\xi = \ln\left(\frac{f(\mathbf{r}|\hat{\boldsymbol{\alpha}}, \hat{v}_x, \hat{v}_y, H_1)}{f(\mathbf{r}|H_0)}\right) \underset{H_0}{\overset{H_1}{\gtrless}} \gamma, \tag{4.15}$$

where

$$f(\mathbf{r}|\hat{\boldsymbol{\alpha}}, \hat{v}_x, \hat{v}_y, H_1) = \max_{\boldsymbol{\alpha}, v_x, v_y} f(\mathbf{r}|\boldsymbol{\alpha}, v_x, v_y, H_1). \tag{4.16}$$

It is noted, that maximizing $f(\mathrm{r}|\boldsymbol{\alpha}, v_x, v_y, H_1)$ in respect to $\boldsymbol{\alpha}, v_x$ and v_y is equivalent to minimizing

$$\sum_{k=1}^{M}\sum_{l=1}^{N}\left(\mathbf{r}_{k,l}-\alpha_{k,l}\mathbf{d}_{k,l}(v_x,v_y)\right)^H\mathbf{C}^{-1}\left(\mathbf{r}_{k,l}-\alpha_{k,l}\mathbf{d}_{k,l}(v_x,v_y)\right), \tag{4.17}$$

which in turn is equivalent to maximizing

$$\begin{aligned}\sum_{k=1}^{M}\sum_{l=1}^{N}&2\Re\{\alpha_i^*\mathbf{d}_{k,l}^H(v_x,v_y)\mathbf{C}^{-1}\mathbf{r}_{k,l}\}\\ &-|\alpha_{k,l}|^2\mathbf{d}_{k,l}^H(v_x,v_y)\mathbf{C}^{-1}\mathbf{d}_{k,l}(v_x,v_y).\end{aligned} \tag{4.18}$$

Further, it is noted that entering the densities given in (4.14) into (4.15) leads to the same expression as (4.18). Furthermore, the expression (4.18) is maximized for *any* given pair v_x and v_y by

$$\alpha_{k,l}=\frac{\mathbf{d}_{k,l}^H(v_x,v_y)\mathbf{C}^{-1}\mathbf{r}_{k,l}}{\mathbf{d}_{k,l}^H(v_x,v_y)\mathbf{C}^{-1}\mathbf{d}_{k,l}(v_x,v_y)}. \tag{4.19}$$

This results in the following decision rule:

$$\xi=\max_{v_x,v_y}\sum_{k=1}^{M}\sum_{l=1}^{N}\frac{\left|\mathbf{d}_{k,l}^H(v_x,v_y)\mathbf{C}^{-1}\mathbf{r}_{k,l}\right|^2}{\mathbf{d}_{k,l}^H(v_x,v_y)\mathbf{C}^{-1}\mathbf{d}_{k,l}(v_x,v_y)}\ \underset{H_0}{\overset{H_1}{\gtrless}}\ \gamma \tag{4.20}$$

It is emphasized that the MIMO-MTD involves a joint estimate involving all receive vectors of the true velocity vector $\vec{v}$. In the next section the implications of this joint estimate are discussed by comparing it to local velocity estimates at the receive stations. Further, it is brought to the reader's attention, that the summands of the test statistic (4.20) are well established in the STAP context as adaptive matched filter test statistic, [37] and [38].

4.2.2 The Multi-Static Moving Target Detector

As mentioned before, an important difference between MIMO radar systems and common multi-static systems is, that in MIMO radar the received signals are processed jointly at a central station, whereas in multi-static radar it is normal, that each receive station processes its received signal autonomously and transmits a *local* decision to a fusion center. In [13] "l-out-of-N" decision fusion rules are discussed for moving target detection. Such detection procedures involve first local decisions at the receive stations based on a threshold test and later a fusion at the central station of those decisions into a final decision, which is H_1 if l or more local decisions indicate target presence and H_0 otherwise. The local thresholds γ' and the fusion rule (how to choose l) have to be optimized jointly for such a detection procedure. In [39], the local thresholds are derived for a *given* fusion rule in the radar context. In [40], the case of bit errors in the transmission of the local decisions is taken into account. However, it is noted that "l out of N" decision rules are only optimal under the assumption that the local observations are conditionally independent and have the same distribution. The reader is referred to [41] and [42] for a thorough treatment of decision fusion.

In this chapter, the multistatic detector is implemented as a fusion of *soft decisions* described by the following test and *global* test statistic

$$\xi = \sum_{k=1}^{M} \sum_{l=1}^{N} \max_{f_{k,l}} \frac{\left|\mathbf{d}_{k,l}^{H}(f_{k,l})\mathbf{C}^{-1}\mathbf{r}_{k,l}\right|^2}{\mathbf{d}_{k,l}^{H}(f_{k,l})\mathbf{C}^{-1}\mathbf{d}_{k,l}(f_{k,l})} \underset{H_0}{\overset{H_1}{\gtrless}} \gamma. \tag{4.21}$$

This expression implies that the l-th receive station estimates the Doppler frequency $f_{k,l}$ due to the supposedly present target's movement independently for each of the transmit stations and indepedently from the other receive stations. The soft decision are transferred to the fusion center, which only sums over all the soft decisions to compute the final test statistic [2]. Thus, instead of transmitting K samples per test and receiver–transmitter–pair to the central station as in the MIMO case only one sample is fed into the fusion center in the multi-static case. It can be argued, that binary local decisions, as described in [13], are

---

[2] The notation $\mathbf{d}(f_{k,l})$ is used for multi static detectors instead of $\mathbf{d}(v_x, v_y)$ to emphasize this local Doppler based estimates.

nothing but a form of quantization of those samples. Following the common observation that the fusion of *soft decisions* outperforms the fusion of *hard decisions*, it can be inferred that a detector based on (4.21) performs at least as good as a detector based on a l-out-of-N fusion procedure.

The expression in (4.21) is the sum of the locally derived likelihood ratios. Summing equal weight likelihood ratios leads to an optimal test statistic under the assumption that the observations are independent, similar to a l-out-of-N fusion. In the here discussed scenario, the observations related to a target without RCS fluctuations are clearly correlated when more than two receivers are employed. But the independent fading coefficients for a target with RCS fluctuations de-correlates those observations considerable. However, deriving a multi-static radar, which is optimal in respect to the eventual residual correlation among observations, is beyond the scope and intention of this dissertation.

4.2.3 Phased Array Moving Target Detector

A conventional phased array radar is steering a transmit beam and a receive beam towards the cell under test under the assumption, that there are no other targets with the same range and that the clutter is uniformly distributed. The beamformer on transmit side is already incorporated in the signal model, (4.8). The beamformer on receive side sums the N receiver signal vectors into a single received vector $\mathbf{r}$

$$\mathbf{r} = \sum_{l=1}^{N} a_l^*(\phi_{\text{steer}})\mathbf{r}_l. \tag{4.22}$$

Assuming that the steering angle ϕ_{steer} matches the angle of arrival ϕ_t, this processing leads to the following observations. The target component of the received signal after this processing under H_1 is

$$\sum_{l=1}^{N} a_l^*(\phi_{\text{steer}})a_l(\phi_t)\alpha\mathbf{d}(v_x, v_y)\sum_{k=1}^{M} b_k^*(\phi_t)b_k(\phi_{\text{steer}}) = MN\alpha\mathbf{d}(v_x, v_y), \tag{4.23}$$

resulting in a post processing target power of $M^2N^2|\alpha|^2$ per sample. As the clutter and noise samples are independent across the receive elements, their joint correlation matrix, post beamforming, has the form

$$\begin{aligned}
&E\left\{\left(\sum_{l=1}^{N} a_l^*(\phi_{\text{steer}}) \sum_{k=1}^{M} \mathbf{c}_{k,l} b_k(\phi_{\text{steer}}) + \mathbf{n}_l\right)\left(\sum_{l'=1}^{N} a_{l'}^*(\phi_{\text{steer}}) \sum_{k'=1}^{M} \mathbf{c}_{k',l'} b_{k'}(\phi_{\text{steer}}) + \mathbf{n}_{l'}\right)^H\right\} \\
&= \sum_{k=1}^{M}\sum_{l=1}^{N} |a_l(\phi_{\text{steer}})|^2 |b_k(\phi_{\text{steer}})|^2 E\left\{\mathbf{c}_{k,l}\mathbf{c}_{k,l}^H\right\} + \sum_{l=1}^{N} |a_l(\phi_{\text{steer}})|^2 E\left\{\mathbf{n}_l\mathbf{n}_l^H\right\} \\
&= NM\mathbf{C}' + N\sigma_n^2\mathbf{I}_{K\times K}. \qquad (4.24)
\end{aligned}$$

Accordingly, it can be inferred, that transmit *and* receive beamforming improves the target to clutter ratio by MN and the target to additive white noise ratio by M^2N. This is due to the fact, that the total transmit power is not normalized in this chapter as previously mentioned. The total transmit power increases with the number of transmitter elements. However, by increasing the total transmit power the system has also to deal with a stronger clutter return. Therefore, increasing the number of transmitter elements enhances the target to thermal noise ratio more drastically than the target to clutter ratio.

For comparing phased array and MIMO radar in the subsequent, it is focused on single transmitter systems. This eases the treatment of the phased array systems. Furthermore, in [8] it is argued, that though beamforming on transmit side in phased array systems enhances the signal to interference ratio, it requires the system to observe only a specific direction at a given instant. In contrast MIMO systems observe the complete space at all times. Accordingly, a comparison between the two systems is "fair" only for a single transmitter. Further, it is noted, that (4.24) leads, for a single transmitter, to $N\mathbf{C}' + N\sigma_n^2\mathbf{I}_{K\times K} = N\mathbf{C}$ describing the interference sum.

In the case of a single transmitter, the beamforming procedure of the phased array on receive side results in a coherent processing gain of N improving the signal to interference ratio, where interference denotes both the clutter return and the additive white noise. In [5] the following signal to interference ratio is given for a clutter dominated scenario:

$$\mathrm{SINR} = \frac{\sigma_t}{\sigma^0 R \theta_B (c\tau/2)\sec\phi}, \tag{4.25}$$

where θ_B is the antenna beamwidth. Using the approximation $\theta_B \approx \frac{\lambda}{D}$ and $D = N \cdot \Delta$, one can confirm, that the improvement in signal to interference ratio scales with N in phased array systems. This observation also verifies the signal model in the previous section.

The moving target detection procedure is based on the single $K \times 1$ vector $\mathbf{r}$. Following the same derivation as in the section 4.2.1 the test statistic is derived as

$$\xi = \max_{f_d} \frac{\left|\mathbf{d}^H(f_d)\mathbf{C}^{-1}\mathbf{r}\right|^2}{\mathbf{d}^H(f_d)\mathbf{C}^{-1}\mathbf{d}(f_d)} \underset{H_0}{\overset{H_1}{\gtrless}} \gamma. \tag{4.26}$$

It is noted again, that the conventional phased array radar observes only one Doppler shift resulting from the targets radial velocity. Accordingly, the GLRT test statistic is based on one estimate of this frequency shift, as (4.26) indicates.

4.2.4 Adaptive MIMO Moving Target Detector

All the decision statistics above are derived for clarity under the assumption of known clutter correlation matrix C. However, in reality this matrix might be unknown. It could still be of the form as described in Section 4.1.3, but feature an unknown σ_v, an unknown clutter power $\rho_{cc}(0)$, an unknown white noise power σ_n^2, or may even be of complete different form. Moreover, different transmitter–receiver–pairs in the MIMO or multi–static system might operate via paths that are subject to different interference levels or characteristics, and, thus, have different clutter matrices. Accordingly, $\mathrm{C}_{k,l}$ denotes in the subsequent the clutter matrix for the specific pair of the l-th transmitter and the k-th receiver.

It is possible, to convert all of the above detectors to adaptive detectors, which maintain a Constant False Alarm Rate (CFAR), [6, 38], under H_0 for any clutter and noise levels and characteristics. This is accomplished by replacing the true clutter matrix by its estimate $\hat{\mathbf{C}}_{k,l}$ based on $L > K$ "secondary" data vectors, $\mathbf{r}_{k,l}(i)$ for each transmitter–receiver–pair k, l,

$$\hat{\mathbf{C}}_{k,l} = \frac{1}{L}\sum_{i=1}^{L} \mathbf{r}_{k,l}(i)\mathbf{r}_{k,l}(i)^H. \tag{4.27}$$

The $\mathbf{r}_{k,l}(i)$ are measured in adjacent range cells, for which target absence is assumed. It is referred to [6] and [37] for details. The MIMO test statistic is then given as

$$\xi = \max_{v_x,v_y} \sum_{k=1}^{M}\sum_{l=1}^{N} \frac{\left|\mathbf{d}_{k,l}^H(v_x,v_y)\hat{\mathbf{C}}_{k,l}^{-1}\mathbf{r}_{k,l}\right|^2}{\mathbf{d}_{k,l}^H(v_x,v_y)\hat{\mathbf{C}}_{k,l}^{-1}\mathbf{d}_{k,l}(v_x,v_y)} \underset{H_0}{\overset{H_1}{\gtrless}} \gamma. \tag{4.28}$$

In Appendix C it is shown, that this test statistic is indeed subject to a CFAR behaviour. The same result can easily be extrapolated to the multi-static and phased array cases. In this context, it is noted that the clutter is assumed to have the same statistical characteristics for all transmitter–receiver–pairs in the phased array system. Thus, the for all pairs common clutter matrix can be estimated on secondary data vectors retrived after the beamforming process. This assumption is not made for the diversity achieving systems (MIMO and multi-static), as due to the desired diversity the transmit and receive elements have to be spread out in space and, thus, it is likely that the observed clutter has different second order statistics for the different transmitter–receiver–pairs.

In Section 4.3.4 the CFAR property of the test statistic (4.28) is demonstrated with numerical results and the MIMO and phased array system in adaptive mode are compared.

4.3 Simulation Results and Inferences

In this section, simulation results are discussed and the performance of the different systems and setups is compared. In Table 4.1 the parameters used in the simulations are listed.

Table 4.1 Parameters of the presented simulation results.

Pulse Repetition Frequency	2kHz
carrier frequency f_c	1GHz
speed of light c	$3 \cdot 10^8 \mathrm{m/s}$
clutter to noise ratio $\frac{P_{cc}}{\sigma_n^2}$	30dB
number of time samples K	10
RMS of clutter motion σ_v	$1.25\mathrm{m/s}$

The PRF is chosen to allow unambitious velocity estimates over a range of roughly $v_x, v_y \in [-500\mathrm{km/h}, 500\mathrm{km/h}]$. The searches of the different GLRT procedures are performed over this range.

4.3.1 A New Kind of Processing Gain

In this section, the MIMO and multi-static detector are compared. In particular, it is illustrated and discussed in what way the tests defined by (4.20) and (4.21) differ. As explained in the previous section, the MIMO detector derives the test statistic based on a joint estimate of the target velocity in vector form based on all available samples. In contrast, a regular multi-static detector is based on likelihood ratios that are derived in respect to the for each transmitter–receiver–pair observed frequency shifts ignoring the observations for the other pairs.

Considering three or more receive different pairs, the MIMO joint maximization approach performs a search over a 2-dimensional space, whereas the multi-static approach searches over N dimensions independently.

In case that a target is present and the target's reflection dominates the received signal, both searches should result in addends in the sums, (4.20) and (4.21), determined by the true velocity vector v and therefore the distributions of the test statistics should not differ.

In contrast, in case, that no target is present and the received signals contain only clutter returns and noise, the MIMO processing imposes the condition on the search for frequencies maximizing the sum (4.20), that all the frequencies have to relate to a hypothetical but realistic target movement. In contrast, the multi-static searches may choose a set of frequencies which result in maxima of the local test-statistics, but which contradict each other. For example, assuming that three receive stations are spread over less than 90°. For this situation, there exists no target movement that results in a positive Doppler at the first and the third station and a negative Doppler at the station in the middle. The MIMO processing takes this into account, whereas the multi-static ignores it. Accordingly, the sum of the total test statistic under H_0 is larger in multi-static radar systems than it is in MIMO radar systems.

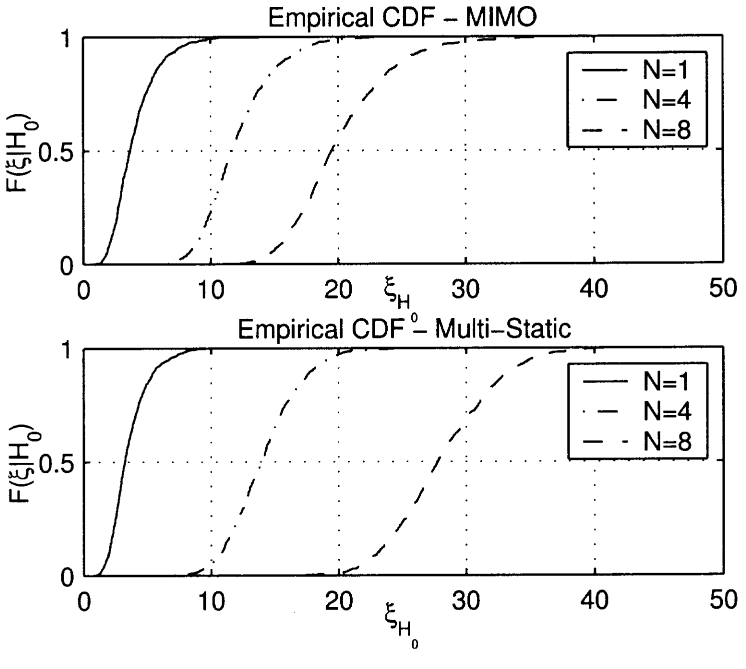

Figure 4.3 CDF of ξ given H_0 for different numbers of receiver antennas.

Figures 4.3 and 4.4 show the CDFs for H_0 and H_1 for radar systems in MIMO or multi-static operation mode. The single transmitter is located at $\theta_1^t = 0°$. For $N = 1$, the receiver is at $\theta_1^r = 0°$. For $N = 4$, the receiver locations are given as $\theta_l^r = \{-39°, -13°, 13°, 39°\}$. For $N = 8$, they are $\theta_l^r = \{-39°, -26°, -13°, 0°, 13°, 26°, 39°, 51°\}$.

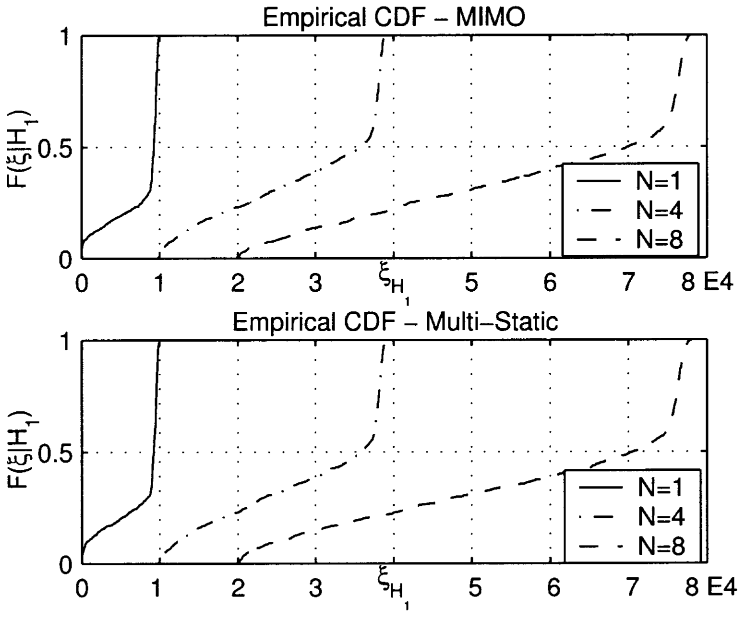

Figure 4.4 CDF of ξ given H_1 for different numbers of receiver antennas.

Figure 4.3 features the experimental Cumulative Density Function (CDF) for the test statistic given H_0. One may see, that the multi static test statistic increases linearly with the number of receive antennas, whereas the MIMO test statistic increases slower.

Figure 4.4 displays the CDFs of the test statistic for a target with speed $300\mathrm{km/h}$ and no RCS fluctuations. The target to interference ratio is 0dB. Here, one can see that given a strong target return the test statistic for MIMO and multi-static radar follow a similar distribution.

It is reiterated, that the MIMO detector imposes the condition on the test statistic, that the frequency shifts, on which the local likelihood measures are based, relate to one common velocity vector. The multi-static detector does not impose such a condition. This condition reduces the interference level in the MIMO-detector and allows to choose a smaller threshold γ, without reducing the target component. Therefore, one may claim that using this condition results in *a new kind of processing gain.*

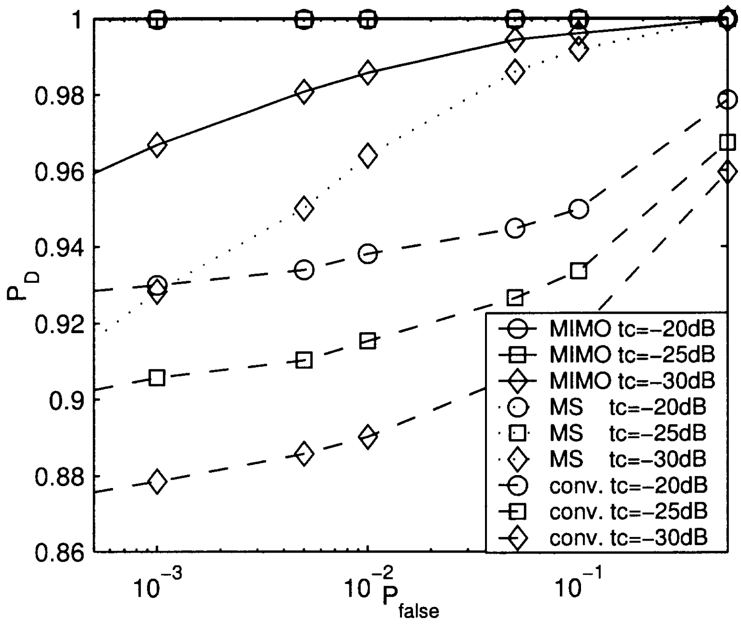

Figure 4.5 ROC for a 300km/h target with random direction and no RCS-fluctuations.

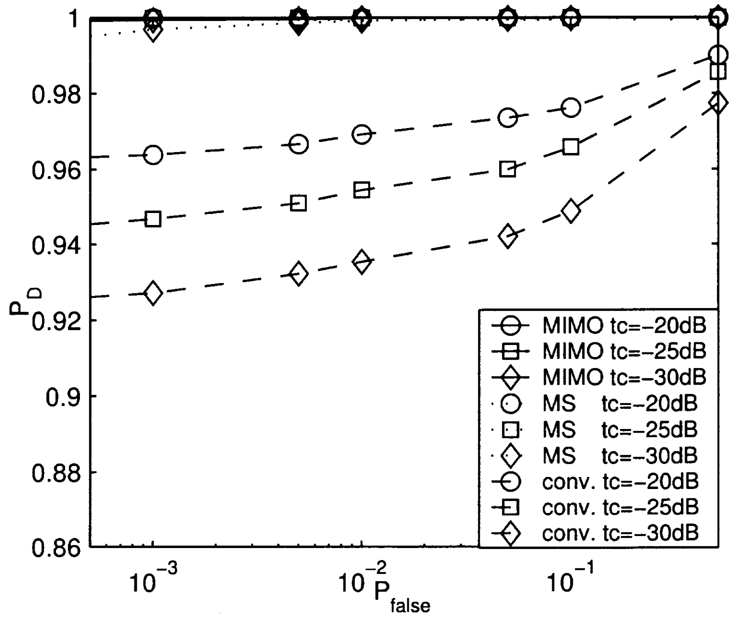

Figure 4.6 ROC for a 500km/h target with random direction and no RCS-fluctuations.

4.3.2 Comparing the three Radar Systems

Here, the different radar systems are compared by the means of their Receiver Operating Characteristics (ROC). The Figures 4.5 and 4.6 show the ROCs for different target to clutter ratios, referred to as "tc" in the legends, and target velocities of 300km/h and 500km/h, respectively, with random direction. 1×8 systems are considered with the element locations as described above.

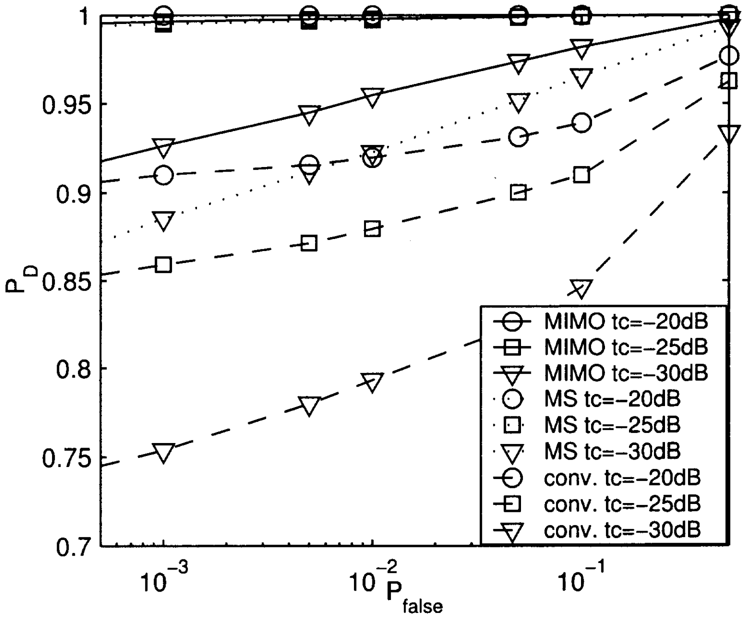

Figure 4.7 ROC for a 300km/h target with random direction and RCS-fluctuations.

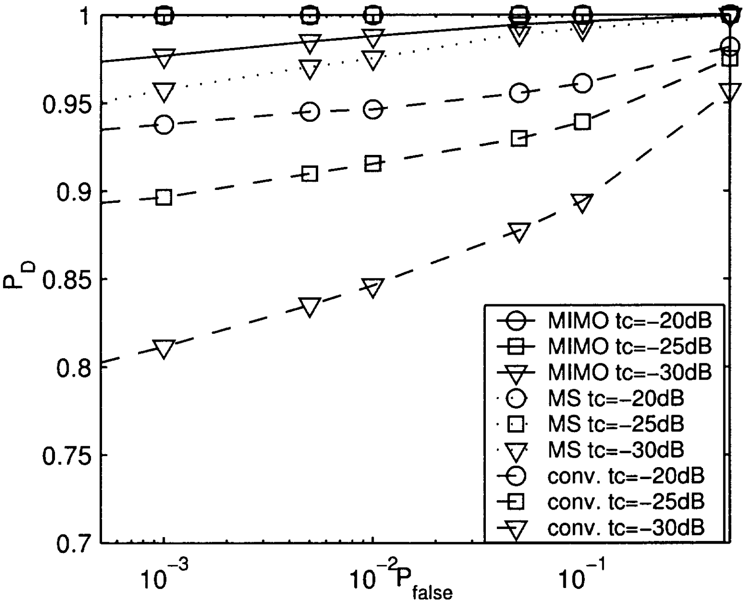

Figure 4.8 ROC for a 500km/h target with random direction and RCS-fluctuations.

It is noted, that though the detection rules have been developed for targets with RCS-fluctuations, the plots in 4.5 and 4.6 show the performance for a non-fluctuating target. From this plots, it can be inferred that the random direction of the target *by itself* leads to a performance impairment similar to the one caused by the fading behavior of the RCS explored in [8]. Conventional radar systems which observe only the radial component of the target's movement suffer under this effect. The reader may note, that in Figure 4.4 the vanishing values of the test statistic for a single antenna illustrate this effect of small radial velocities. Further, it is obvious that with an increased absolute speed value the chances of small radial velocities, which are attenuated by the detector processing, are reduced. Therefore, the performance of the phased array system is less subject to the according degradations. The Figures 4.5 and 4.6 show this tendency.

The Figures 4.7 and 4.8 feature the ROCs for targets with RCS fluctuations and velocities of $300\mathrm{km/h}$ and $500\mathrm{km/h}$ with random direction. One may realize, that the RCS fluctuations impair the performance of all three radar systems. However, the MIMO and multi-static radars outperform the conventional phased array systems because of their spatial diversity in respect to the target's movement direction and the target's RCS fluctuations. Furthermore, the MIMO system outperforms the multi-static system because it imposes a condition on the interference, as explained in Section 4.3.1.

4.3.3 Distributed Transmitter Elements

In Section 4.1 it has been argued, that in the light of equation (4.7) it is desirable to distribute both, receiver and transmitter elements, in space to ensure that the target's movement results in sufficient Doppler shifts to separate between target and interference. In this Subsection, the validity of this argument is demonstrated by comparing a 1×8 and a 2×4 MIMO–radar with each other. The element locations of the 1×8 system are $\theta_1^t = 45°$ and $\theta_l^r = \{0°, 13°, 26°, 38°, 50°, 62°, 75°, 90°\}$. The 2×4 system consists of transmitter and receiver elements located at $\theta_k^t = \{5°, 85°\}$ and $\theta_l^t = \{0°, 30°, 60°, 90°\}$.

It should be noted here, that as the 1×8 and 2×4 capture the same amount of energy reflected by the target and have the same number of "diversity branches", namely $N \cdot M = 8$, it is obvious that they should perform identical in a simple single pulse and white interference situation. Indeed, with the analysis presented in [8] and Section 3.3 this may be verified. The reader should note again, that in [8] and Section 3.3 the total transmit power is normalized and under this constraint a 2×4 system is outperformed by 1×8. "Denormalizing" the transmit power in Section 3.3 by replacing $\frac{E}{M}$ with E in expressions (3.17) and (3.20) clearly illustrates that for simple AWGN detection without power normalization a MIMO and SIMO would have identical ROCs as long as only the product $M \cdot N$ remains constant.

In contrast, Figure 4.9 shows that the system with two transmitters outperforms a single transmitter system.

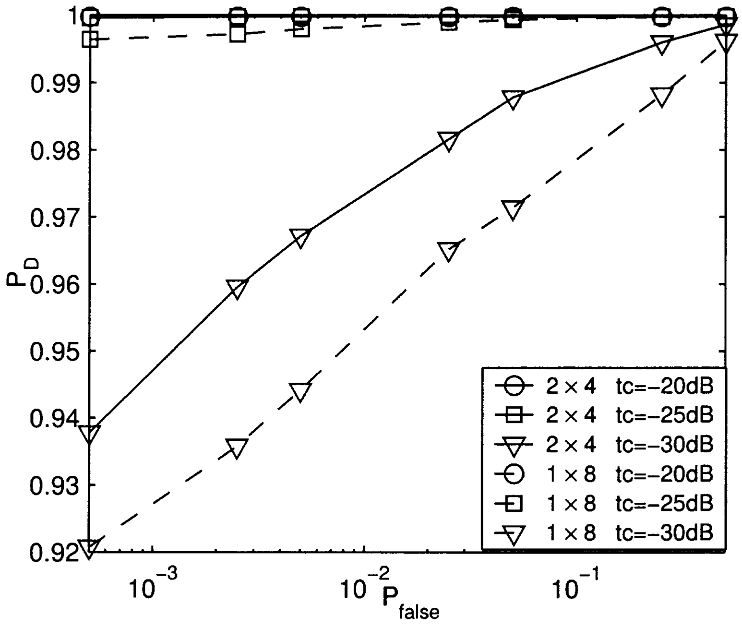

Figure 4.9 ROC for a 300km/h target with random direction and RCS-fluctuations for a 1×8 and 2×4 system.

This is a remarkable observation, as it contrasts possible inferences from the analysis found for simple scenarios in [8] and Section 3.3. Further, noting that the 1×8 system has a total of 9 transmit or receive stations whereas the 2 × 4 system has only 6 stations, the preference towards systems with distributed transmitter *and* receiver elements may be strengthened by an economical argument.

4.3.4 CFAR Properties of the Test Statistics

In this section, 1×4 and 1×8 adaptive MIMO or phased array systems are discussed. Figure 4.10 shows the empirical CDF of the adaptive MIMO test statistic, (4.28), under H_0 for a 1×4 system and different numbers of secondary vectors, L. The transmit and receiver elements have the same positions as in Section 4.3.1.

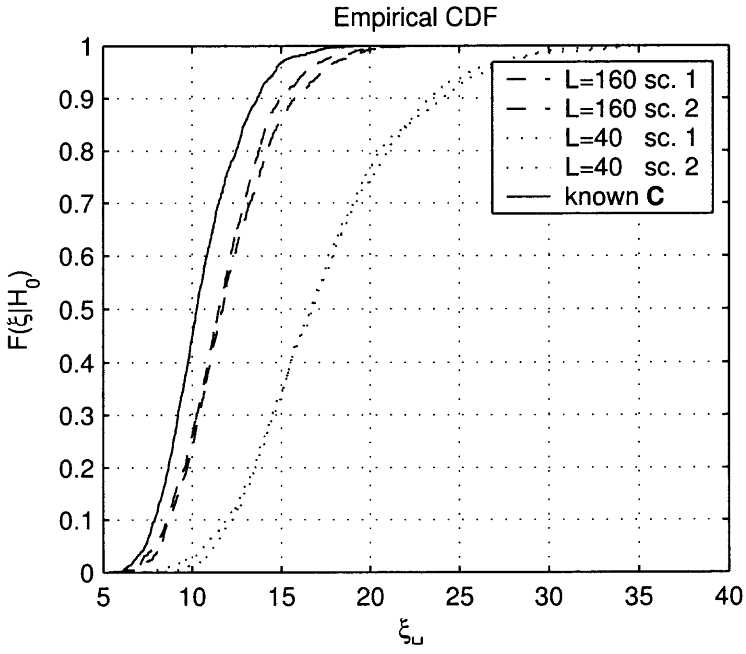

Figure 4.10 CDFs for a CFAR 1×4 system with different amounts of secondary samples.

The solid curve is the CDF resulting from a known clutter covariance matrix. The dashed curves reflect the empirical CDF of the test statistic ξ under H_0 for $L = 160$ and the dotted ones for $L = 40$. For each L two scenarios are considered:

- Scenario 1 (sc. 1): The clutter covariance matrix is the same for all receiver elements and has the previously described form (Table 4.1 and Section 4.1.3).

- Scenario 2 (sc. 2): Two of the four receiver elements observe clutter returns with the same covariance matrix as before. For the other two the clutter to noise ratio is reduced by 20dB and the complete interference power raised by 6dB.

The almost identical empirical CDFs for the two scenarios illustrate, that the adaptive test statistic has a distribution that is independent of the underlying clutter characteristic and, therefore, can be used in a detector with CFAR properties. However, the number of secondary vectors used in the estimate of the covariance matrix has an impact on the test statistic distribution. For small values of L a large threshold has to be used for a given P_{false}, as the variance of the test statistic under H_0 increases. This leads to a reduced P_D and is a well observed fact for CFAR detection, [6].

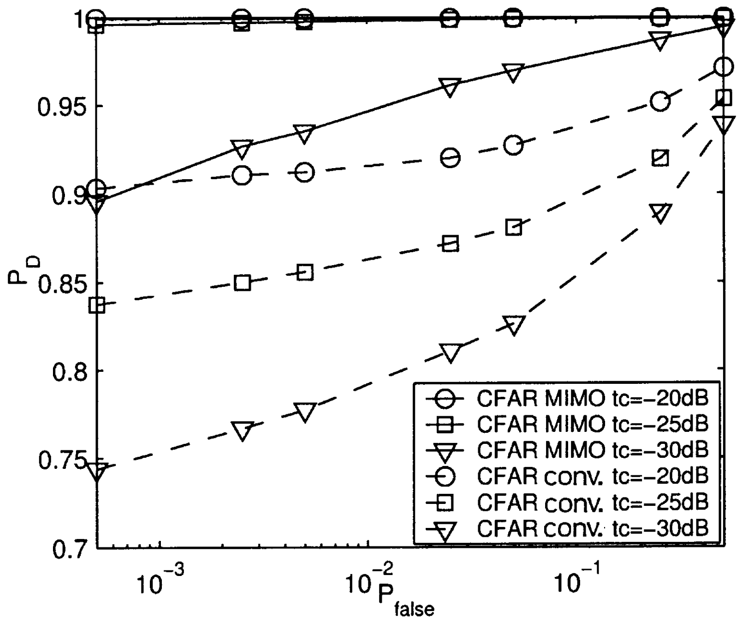

Figure 4.11 ROC for a 300km/h target with random direction and RCS-fluctuations for a phased array and MIMO 1×8 CFAR system, $L = 200$.

Figure 4.11 shows the ROCs for 1×8 MIMO and phased array radar systems. $L = 200$ secondary data vectors are used. A target with RCS fluctuations and a speed of $|\vec{v}| = 300$km/h is considered for H_1. Comparing those ROCs to the ROCs featured in Figure 4.7 it can be inferred that performance of both, MIMO–radar and phased array radar, is slightly impaired. However, the MIMO–system still outperforms the phased array one significantly.

CHAPTER 5

HIGH RESOLUTION MODE OF MIMO-RADAR

This chapter explores the potential of MIMO–systems to locate a single point scatter or separate between several of those with coherent processing over the extremely sparse MIMO–aperture. For completeness, it is noted that a similar system with a single transmitter is discussed in [43]. However, the here presented analysis covers the use of several transmitter elements and investigates the role of different system parameters.

Normally, the spatial resolution in range of a radar system is determined by the signal bandwidth employed. Coherent processing over sensor elements partly surrounding the target may overcome this barrier.

The chapter is organized as follows: First, a signal model for a single scatter is developed. Based on this model, the ambiguity function for a two dimensional target location estimation is introduced. Afterwards, theoretical bounds for the location estimation accuracy of a single scatter are introduced and compared to simulation results. The bounds are then linked to properties of the ambiguity function. This leads to a further exploration of the ambiguity function and of how system parameters, such as signal bandwidth and angular spread of the MIMO elements, determine the shape of this ambiguity function.

The reader is asked to note, that in this chapter the total transmit power is again not normalized by the number of transmit elements in contrast to Chapters 2 and 3.

5.1 Signal Model and Ambiguity Function

To illustrate the potential of high resolution approaches in MIMO-radar, this Chapter explores first the accuracy, with which a single scatter can be located by a coherent array consisting of extremely widely separated elements, similar to [43, 44]. The single point scatter is assumed to reflect isotropically all impinging waves to all receive elements, thus allowing the coherent processing among the elements. However, the reflection coefficient of the scatter is assumed to be unknown. For simplicity a two dimensional scenario is assumed. The location of the scatter is to be determined within a limited area, which may be determined by a previously *non-coherent* detection mode, as described in Chapters 3 and 4 or [29]. It is convenient to introduce a coordinate system with the origin at the center of the area and to estimate the scatter location $\vec{X} = [x, y]^T$ relative to this origin. Figure 5.1 illustrates this scenario. The k-th transmit and l-th receive elements are located at angles θ_k^t and θ_l^r with respect to the origin as illustrated in Figure 5.1. It is assumed that the monitored area to be small compared to the distances from the origin to all transmitters and receivers, such that if the origin would be moved to any point in the monitored area, the anglesθ_k^t and θ_l^r, would not change for all k, l. In this chapter, it is focused on scenarios in which the elements surround the scatter partly, thus, e.g., $|\theta| \leq 90°$.

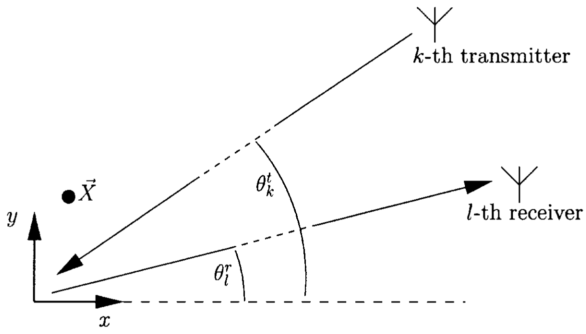

Figure 5.1 Overview of system layout.

Moreover, the following discussion is simplified by assuming that the phases and the time references at the transmit and receive elements are calibrated to a hypothetical scatter location at the origin of above mentioned coordinate system. Under the given assumptions, the signal attenuation due to the distance from the transmitter or receiver to the target scatter is approximately constant, which can thus be neglected in time delay calculations. Furthermore, a single snapshot or pulse scenario is considered. The waveform transmitted by the k-th transmitter, reflected by a scatter located at $\vec{X}$, leads to a signal component at the l-th receiver of the following form

$$r_{k,l}(t) = as_k(t - \tau_{k,l}(\vec{X})) + n_{k,l}(t), \tag{5.1}$$

where a contains the reflectivity of the scatter, $n_{k,l}(t)$ is the white Gaussian noise, and $\tau_{k,l}(\vec{X})$ is the delay for the k, l transmit–receive–pair introduced by the scatter location $\vec{X}$,

$$\tau_{k,l}(\vec{X}) = -\frac{x}{c}(\cos\theta_k^t + \cos\theta_l^r) - \frac{y}{c}(\sin\theta_k^t + \sin\theta_l^r). \tag{5.2}$$

Hereinafter, the explicit dependency of $\tau_{k,l}$ on $\vec{X}$ is omitted for conciseness. The above signals are bandpass signals of the form $r_{k,l}(t) = r_{k,l}^b(t)e^{j2\pi f_c t}$ and $s_k(t) = s_k^b(t)e^{j2\pi f_c t}$. Assuming that the baseband waveforms maintain approximate orthogonality even for different mutual delays, $\int s_k^b(t)s_{k'}^{b*}(t - \tau)dt \approx 0 \ \forall\tau, k \neq k'$, the receiver elements can separate the signals from different transmitters. The received signals over the complete system may then be represented by a $MN \times 1$ vector function $\mathbf{r}(t) = [r_{1,1}(t), \ldots, r_{M,N}(t)]^T$. The noise components are assumed to be i.i.d. Gaussian. Therefore, the pdf of the received signal vector given a scatter at $\vec{X}$ with reflectivity a can readily be expressed as

$$\begin{aligned}
&f(\mathbf{r}(t)|\vec{X}, a) \\
&\propto \exp\left\{-\frac{1}{\sigma^2}\sum_{k=1}^{M}\sum_{l=1}^{N}\int |r_{k,l}(t) - as_k(t - \tau_{k,l})|^2 dt\right\} \\
&= \exp\left\{-\frac{1}{\sigma^2}\left(\sum_{k=1}^{M}\sum_{l=1}^{N}\int |r_{k,l}(t)|^2 + |a|^2|s_k(t - \tau_{k,l})|^2 dt\right.\right. \\
&\qquad \left.\left.-2\Re\left\{a\sum_{k=1}^{M}\sum_{l=1}^{N}\int r_{k,l}^*(t)s_k(t - \tau_{k,l})dt\right\}\right)\right\}.
\end{aligned} \tag{5.3}$$

It is noted that the only term depending on the actual scatter position in (5.3) is the third summand. Assuming unit norm waveforms, the second summand can be expressed as $\sum_{k=1}^{M}\sum_{l=1}^{N}\int |a|^2|s_k(t - \tau_{k,l})|^2 dt = MN|a|^2$. The maximum likelihood esteimate of the parameter a, which is

$$\hat{a} = \frac{1}{MN} \sum_{k=1}^{M} \sum_{l=1}^{N} \int r_{k,l}(t) s_k^*(t - \tau_{k,l}) dt, \tag{5.4}$$

is used to eliminate a in 5.3. Then the logarithm of the pdf of the received signal is given as

$$\begin{aligned} \ln f(\mathbf{r}(t)|\vec{X}) &= c' \left| \sum_{k=1}^{M} \sum_{l=1}^{N} \int r_{k,l}^*(t) s_k(t - \tau_{k,l}) dt \right|^2 + c'' \\ &= c' \left| \sum_{k=1}^{M} \sum_{l=1}^{N} e^{-j2\pi f_c \tau_{k,l}} \int r_{k,l}^{b*}(t) s_k^b(t - \tau_{k,l}) dt \right|^2 + c'', \end{aligned} \tag{5.5}$$

where c' and c'' denote constants independent of the scatter location. The second expression separates between the phase shifts due to the carrier frequency and the baseband correlation processes. Note, these phase shifts can only be observed in a coherent processing mode accross all elements. The Maximum Likelihood estimate of the scatter location, $\hat{\vec{X}}$, is then given as

$$\max_{\vec{X}} \ln f(\mathbf{r}(t)|\vec{X}) = \ln f(\mathbf{r}(t)|\hat{\vec{X}}). \tag{5.6}$$

In the next section, this estimate's empirical variance is found using Monte Carlo simulations and this variance is compared to the Cramer Rao lower bound.

An intuitive way to illustrate high resolution location estimation is to introduce the *ambiguity function*, $A(\vec{X})$. The notion of an ambiguity function has long been used in the context of location estimates in radar, e.g. [6]."Placing" a scatter at the origin of the coordinate system, which implies $r_{k,l}(t) = s_k(t)$, the ambiguity function may be defined as a scaled version likelihood expression given in (5.5),

$$\begin{aligned} A(\vec{X}) &= d' \ln f(\mathbf{r}(t)|\vec{X}) + d'' \\ &= \frac{1}{M^2N^2} \left| \sum_{k=1}^{M} \sum_{l=1}^{N} \int s_k^*(t) s_k(t-\tau_{k,l}) dt \right|^2 \\ &= \frac{1}{M^2N^2} \left| \sum_{k=1}^{M} \sum_{l=1}^{N} e^{-j2\pi f_c \tau_{k,l}} \int s_k^{b*}(t) s_k^b(t-\tau_{k,l}) dt \right|^2 . \end{aligned} \tag{5.7}$$

The constants d' and d'' scale the ambiguity in such a manner, that $0 \le A(\vec{X}) \le 1$ is ensured.

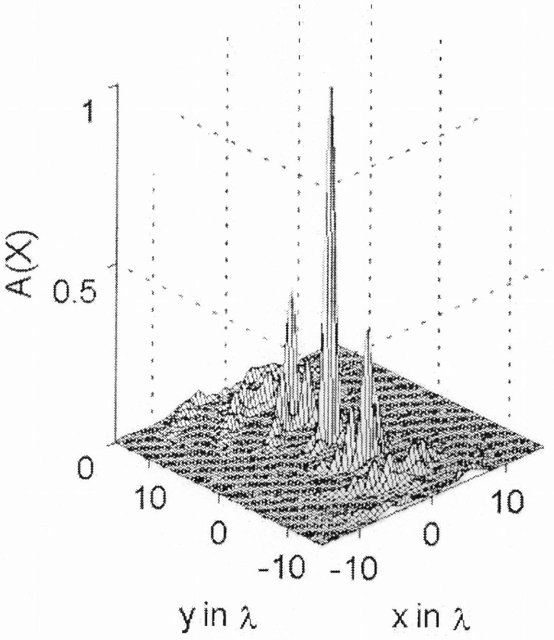

Figure 5.2 Ambiguity Function for a 9×9 MIMO-radar.

Figure 5.2 contains a plot of a ambiguity function for a 9×9 MIMO system with the transmitter elements distributed evenly over $-45° \le \theta \le 45°$. The receiver elements are similarly distributed. A x and y cut of this ambiguity function can be found in Figure 5.6. The transmitted signals $s_k(t)$ are assumed to have a rectangular frequency response with bandwidth Δf. The ratio of this bandwidth to the carrier frequency is set to one tenth, $\frac{\Delta f}{f_c} = 0.1$. The impact of this value is discussed in the following sections. The x and y coordinates are given in multiples of the used wavelength λ. The very narrow mainlobe around the origin reflects the great capabilities of coherent processing in MIMO-radar.

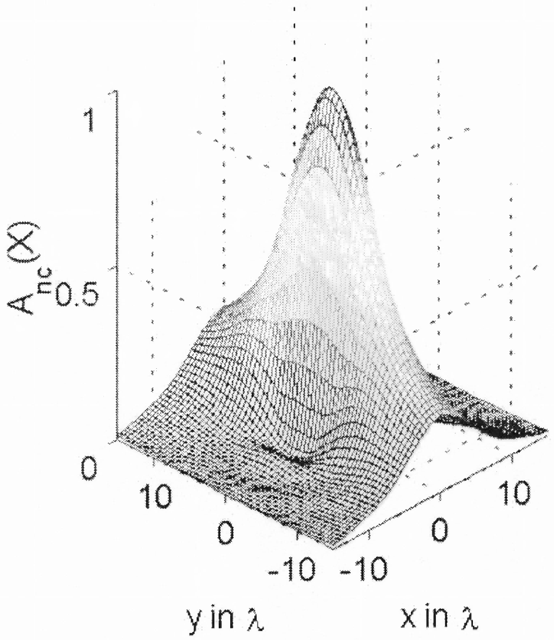

Figure 5.3 Non–coherent Ambiguity Function for a 9×9 MIMO-radar.

The integrals in the sums of the last line of (5.7) are the autocorrelation functions of the used waveforms $\int s_k^{b*}(t) s_k^b(t-\tau) = \varphi_{s_k^b}(\tau)$. Accordingly the ambiguity function can be rewritten as

$$A(\vec{X}) = \frac{1}{M^2 N^2} \left| \sum_{k=1}^{M} \sum_{l=1}^{N} e^{-j2\pi f_c \tau_{k,l}} \varphi_{s_k^b}(\tau_{k,l}) \right|^2 , \qquad (5.8)$$

which further illustrates the role of the phase shifts across the transmitter–receiver–pairs in the coherent processing. The impact of these phase shifts is further illuminated by introducing the *non–coherent* ambiguity function, $A_{nc}(\vec{X})$, which serves as an upper bound for the coherent ambiguity function,

$$A(\vec{X}) \leq A_{nc}(\vec{X}) = \frac{1}{M^2N^2}\left(\sum_{k=1}^{M}\sum_{l=1}^{N}|\varphi_{s_k^b}(\tau_{k,l})|\right)^2 . \tag{5.9}$$

This function illustrates the location accuracy possible for a MIMO system in non–coherent operation. The location estimate is then solely based on the bandwidth of the used signals. It is plotted in Figure 5.3 for the same example system as before. A x and y cut of this non–coherent ambiguity function can be found in Figure 5.8.

By comparing the two plots, it becomes obvious how the coherent processing greatly enhances the accuracy by narrowing the mainlobe of the ambiguity function substantially.

This section is concluded by demonstrating the ability of a MIMO–radar system to resolve several closely spaced scatter. Figure 5.4 features the ambiguity function for four equal return point scatters at locations $[0,0]^T$, $[0,6]^T$, $[6,0]^T$ and $[6,6]^T$. The coordinate system is again in multiples of λ.

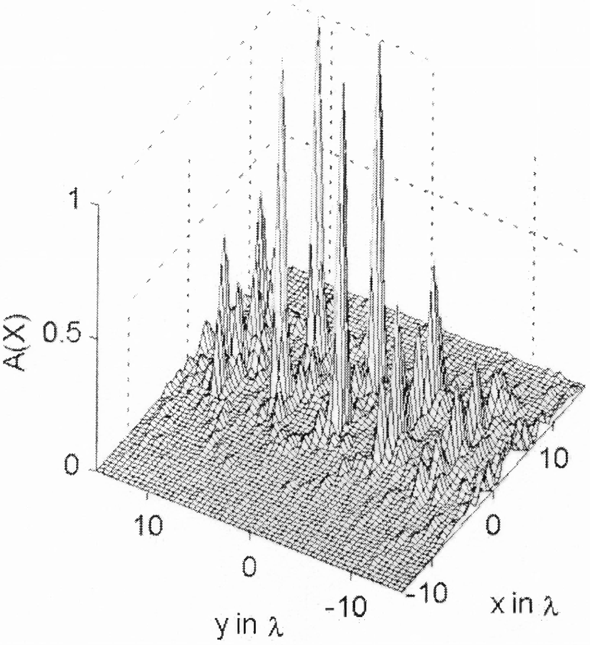

Figure 5.4 Ambiguity Function for four scatters in close proximity and a 9×9 MIMO-radar.

Comparing this plot to the non coherent one in Figure 5.3, it is obvious, that a coherent operating MIMO–radar can accurately resolve several close scatters, which a non–coherent MIMO–radar could not distinguish. These scatters might either constitute a single target with a fluctuating RCS or represent separate small targets.

5.2 Cramer Rao Bound

As discussed in [27], the Cramer Rao Bound (CRB) for a parameter vector, $\boldsymbol{\psi}$ to be estimated is given as

$$E\left\{(\hat{\boldsymbol{\psi}} - \boldsymbol{\psi})(\hat{\boldsymbol{\psi}} - \boldsymbol{\psi})^H\right\} \geq \mathbf{C}_{CRB}(\boldsymbol{\psi}) = \mathbf{J}^{-1}(\boldsymbol{\psi}), \tag{5.10}$$

where the inequality implies that the difference between the first and the second matrix is a positive definite matrix. Therefore, the CRB provides a lower bound for the Mean Square Error (MSE) of any unbiased estimator, which may be expressed as [45]

$$\text{var}\{\hat{\boldsymbol{\psi}}_i\} \geq \left[\mathbf{J}^{-1}(\boldsymbol{\psi})\right]_{i,i}. \tag{5.11}$$

In the here discussed scenario, the parameter vector contains the x and y coordinates of the scatter and the real and imaginary part of the common amplitude of the reflected signal, a_r and a_i, $\boldsymbol{\psi} = [x, y, a_r, a_i]^T$. In both equations $\mathbf{J}(\boldsymbol{\psi})$ refers to the Fisher information matrix, which is defined as

$$\begin{aligned}\mathbf{J}(\boldsymbol{\psi}) &= E\left\{\nabla_{\boldsymbol{\psi}} \ln f(\mathbf{r}(t)) \left(\nabla_{\boldsymbol{\psi}} \ln f(\mathbf{r}(t))\right)^H\right\} \\ &= -E\left\{\nabla_{\boldsymbol{\psi}} \left(\nabla_{\boldsymbol{\psi}} \ln f(\mathbf{r}(t))\right)^H\right\}.\end{aligned} \tag{5.12}$$

Introducing an alternative parameter vector, $\boldsymbol{\vartheta}$, the chain rule can be used with the first equality of (5.12), [46],

$$\begin{aligned}\mathbf{J}(\boldsymbol{\psi}) &= \nabla_{\boldsymbol{\psi}} \boldsymbol{\vartheta}^H E\left\{\nabla_{\boldsymbol{\vartheta}} \ln f(\mathbf{r}) \left(\nabla_{\boldsymbol{\vartheta}} \ln f(\mathbf{r})\right)^H\right\} \left(\nabla_{\boldsymbol{\psi}} \boldsymbol{\vartheta}^H\right)^H \\ &= \boldsymbol{\mathcal{G}} \mathbf{J}(\boldsymbol{\vartheta}) \boldsymbol{\mathcal{G}}^H.\end{aligned} \tag{5.13}$$

Consider a particular $\boldsymbol{\vartheta}$, that contains the $M \cdot N$ time delays $\tau_{k,l}$ and the complex amplitude pair a_r and a_i such that

$$\boldsymbol{\vartheta} = \left[\tau_{1,1} \ldots, \tau_{k,l}, \ldots, \tau_{M,N} a_r, a_i\right]^T . \tag{5.14}$$

The $4 \times (M \cdot N + 2)$ matrix $\boldsymbol{\mathcal{G}}$ mainly describes the geometric setting and has according to the previously described signal model (5.2) the form

$$\boldsymbol{\mathcal{G}} = \begin{pmatrix} -\frac{1}{c}\left(\cos\theta_1^t + \cos\theta_1^r\right) & \ldots & -\frac{1}{c}\left(\cos\theta_M^t + \cos\theta_N^r\right) & 0 & 0 \\ -\frac{1}{c}\left(\sin\theta_1^t + \sin\theta_1^r\right) & \ldots & -\frac{1}{c}\left(\sin\theta_M^t + \sin\theta_N^r\right) & 0 & 0 \\ 0 & \ldots & 0 & 1 & 0 \\ 0 & \ldots & 0 & 0 & 1 \end{pmatrix} \tag{5.15}$$

Given the density of the received signal (5.3), $\mathbf{J}(\boldsymbol{\vartheta})$ is evaluated subsequently. First,

$$\begin{aligned} \frac{\delta \ln f(\mathbf{r})}{\delta \tau_{k,l}} = & \frac{-1}{\sigma^2} \int \left(r_{k,l}(t) - a s_k(t - \tau_{k,l})\right) a^* \dot{s}_k^*(t - \tau_{k,l}) \\ & + \left(r_{k,l}(t) - a s_k(t - \tau_{k,l})\right)^* a \dot{s}_k(t - \tau_{k,l}) dt, \end{aligned} \tag{5.16}$$

with $\dot{s}_k(t) = \frac{\delta}{\delta t} s_t(t)$. This readily leads to

$$E\left\{\frac{\delta^2 \ln f(\mathbf{r})}{\delta \tau_{k,l} \delta \tau_{k',l'}}\right\} = 0 \qquad \forall l \neq l' \text{ or } k \neq k'. \tag{5.17}$$

On the contrary, one finds for the $M \cdot N$ diagonal elements of $\mathbf{J}(\boldsymbol{\vartheta})$

$$E\left\{\frac{\delta^2 \ln f(\mathbf{r})}{\delta \tau_{k,l}^2}\right\} = \frac{-2|a|^2}{\sigma^2} \int \dot{s}_k(t - \tau_{k,l}) \dot{s}_k^*(t - \tau_{k,l}) dt, \tag{5.18}$$

where $E\left\{\int (r(t) - a s_k(t - \tau_{k,l}) \ddot{s}_k^*(t - \tau_{k,l}) dt\right\} = 0$ is used. This equality furthermore is used to derive the following two terms,

$$E\left\{\frac{\delta^2 \ln f(\mathbf{r})}{\delta \tau_{k,l} \delta a_r}\right\} = \frac{2}{\sigma^2} \mathfrak{Re}\left\{a \int \dot{s}_k(t - \tau_{k,l}) s_k^*(t - \tau_{k,l}) dt\right\}, \tag{5.19}$$

$$E\left\{\frac{\delta^2 \ln f(\mathbf{r})}{\delta \tau_{k,l} \delta a_i}\right\} = \frac{2}{\sigma^2} \mathfrak{Im}\left\{a \int \dot{s}_k(t - \tau_{k,l}) s_k^*(t - \tau_{k,l}) dt\right\}. \tag{5.20}$$

It is easy to verify the following three equalities:

$$E\left\{\frac{\delta^2 \ln f(\mathbf{r})}{\delta a_r^2}\right\} = \frac{-2}{\sigma^2}\sum_{k=1}^{M}\sum_{l=1}^{N}\int |s_k(t-\tau_{k,l})|^2 dt, \tag{5.21}$$

$$E\left\{\frac{\delta^2 \ln f(\mathbf{r})}{\delta a_i^2}\right\} = \frac{-2}{\sigma^2}\sum_{k=1}^{M}\sum_{l=1}^{N}\int |s_k(t-\tau_{k,l})|^2 dt, \tag{5.22}$$

$$E\left\{\frac{\delta^2 \ln f(\mathbf{r})}{\delta a_i \delta a_r}\right\} = 0. \tag{5.23}$$

The previously occurring integrals containing the transmitted signals are evaluated by replacing $s_k(t)$ with $s_k^b(t) \cdot e^{j2\pi f_c t}$. For (5.18) this leads to

$$\begin{aligned} &\int \dot{s}_k(t-\tau_{k,l})\dot{s}_k^*(t-\tau_{k,l})dt = \\ &4\pi^2\left(f_c^2\int |S_k^b(f)|^2 df + \int f^2|S_k^b(f)|^2 df\right) \end{aligned} \tag{5.24}$$

and for (5.19) and (5.20) to

$$\int \dot{s}_k(t-\tau_{k,l})s_k^*(t-\tau_{k,l})dt = j2\pi f_c \int |S_k^b(f)|^2 df. \tag{5.25}$$

Using $\sigma^2 = N_0 \int |S_k^b(f)|^2 df$ and the effective bandwidth β, defined as

$$\beta^2 = \frac{\int f^2 |S_k^b(f)|^2 df}{\int |S_k^b(f)|^2 df}, \tag{5.26}$$

the first MN diagonal elements of $\mathbf{J}(\boldsymbol{\vartheta})$ (compare to (5.18)) are given as

$$[\mathbf{J}(\boldsymbol{\vartheta})]_{i,i} = \frac{8\pi^2|a|^2}{N_0}(f_c^2+\beta^2) \qquad i = 1,\ldots,MN. \tag{5.27}$$

It is noted that the off-diagonal elements of the upper left $MN \times MN$ submatrix of $\mathbf{J}(\boldsymbol{\vartheta})$ are zero according to (5.17). The elements of the lower left $2 \times MN$ submatrix of $\mathbf{J}(\boldsymbol{\vartheta})$ are found via (5.19) and (5.20), respectively, as

$$[\mathbf{J}(\boldsymbol{\vartheta})]_{MN+1,i} = \frac{4\pi f_c a_i}{N_0} \qquad i = 1,\ldots,MN, \tag{5.28}$$

$$[\mathbf{J}(\boldsymbol{\vartheta})]_{MN+2,i} = -\frac{4\pi f_c a_r}{N_0} \qquad i = 1, \ldots, MN. \tag{5.29}$$

Furthermore, the diagonal elements of the 2×2 lower right submatrix of $\mathbf{J}(\boldsymbol{\vartheta})$ are found according to (5.21) and (5.22) as

$$[\mathbf{J}(\boldsymbol{\vartheta})]_{i,i} = \frac{2MN}{N_0} \qquad i = MN+1, MN+2. \tag{5.30}$$

According to (5.13), $\mathbf{J}(\boldsymbol{\psi})$ can now be calculated and is provided in (5.31), where for conciseness $\mathcal{X}_{k,l} = \cos\theta_k^t + \cos\theta_l^r$ and $\mathcal{Y}_{k,l} = \sin\theta_k^t + \sin\theta_l^r$ is used. The lower bounds for the variance of the x and y estimates are the $(1,1)$ and $(2,2)$ elements of $\mathbf{J}(\boldsymbol{\psi})^{-1}$. It is noted, that these elements do not depend on the real or imaginary part of the signal amplitude, a_r or a_i, specifically, but on the square signal energy $|a|^2 = a_r^2 + a_i^2$. The bounds derived in the above manner allow to predict performance of a location estimate for a single scatter. Therefore, they can be used to judge the high resolution potential of coherent MIMO–radar systems as described in the previous section and [29]. They also allow to derive accuracy limits of approaches similar to the ones presented in [43, 44]. Furthermore, important conclusions about the influence of system–parameters on the accuracy of the parameter estimation can be derived from $\mathbf{J}(\boldsymbol{\psi})$. Assuming a rectangular frequency response, $S_k^b(f)$, $f \in [-\frac{\Delta f}{2}, \frac{\Delta f}{2}]$, the square of the effective bandwidth is found as $\beta^2 = \frac{\Delta f^2}{12}$. Therefore, even for relatively high bandwidth to carrier ratios, e.g. $\frac{\Delta f}{f_c} = 0.1$, the contribution of the signal bandwidth to the CRB is negligible as $\frac{\beta^2}{f_c^2} \ll 1$ and thus $(1 + \frac{\beta^2}{f_c^2}) \approx 1$ in the upper left submatrix of (5.31). However, it is noted, that by replacing $(1 + \frac{\beta^2}{f_c^2})$ with $\frac{\beta^2}{f_c^2}$ the upper left matrix in (5.31) becomes the Fisher information matrix, one would attain in a purely Time Of Arrival (TOA) and thus non–coherent scheme, as described in [46]. Furthermore, it is possible to conclude from (5.31) that the CRB's for the x and y estimates are proportional to λ^2 [1] and the inverse of SNR. The proportionality

---

[1] Assuming a constant $\frac{\Delta f}{f_c}$.

to λ^2 and equivalently $\frac{1}{f_c^2}$ is due the fact, that the coherent MIMO–system makes use of the phase information accross different paths, as, for example, equation 5.5 illustrates.

$$\mathbf{J}(\boldsymbol{\psi}) =$$

$$\begin{pmatrix} \frac{8\pi^2|a|^2}{\lambda^2 N_0}(1+\frac{\beta^2}{f_c^2})\sum_{k=1}^{M}\sum_{l=1}^{N}\mathcal{X}_{k,l}^2 & \frac{8\pi^2|a|^2}{\lambda^2 N_0}(1+\frac{\beta^2}{f_c^2})\sum_{k=1}^{M}\sum_{l=1}^{N}\mathcal{X}_{k,l}\mathcal{Y}_{k,l} & \frac{-4\pi a_i}{\lambda N_0}\sum_{k=1}^{M}\sum_{l=1}^{N}\mathcal{X}_{k,l} & \frac{4\pi a_r}{\lambda N_0}\sum_{k=1}^{M}\sum_{l=1}^{N}\mathcal{X}_{k,l} \\ \frac{8\pi^2|a|^2}{\lambda^2 N_0}(1+\frac{\beta^2}{f_c^2})\sum_{k=1}^{M}\sum_{l=1}^{N}\mathcal{X}_{k,l}\mathcal{Y}_{k,l} & \frac{8\pi^2|a|^2}{\lambda^2 N_0}(1+\frac{\beta^2}{f_c^2})\sum_{k=1}^{M}\sum_{l=1}^{N}\mathcal{Y}_{k,l}^2 & \frac{-4\pi a_i}{N_0}\sum_{k=1}^{M}\sum_{l=1}^{N}\mathcal{Y}_{k,l} & \frac{4\pi a_r}{N_0}\sum_{k=1}^{M}\sum_{l=1}^{N}\mathcal{Y}_{k,l} \\ \frac{-4\pi a_i}{\lambda N_0}\sum_{k=1}^{M}\sum_{l=1}^{N}\mathcal{X}_{k,l} & \frac{-4\pi a_i}{\lambda N_0}\sum_{k=1}^{M}\sum_{l=1}^{N}\mathcal{Y}_{k,l} & \frac{2MN}{N_0} & 0 \\ \frac{4\pi a_r}{\lambda N_0}\sum_{k=1}^{M}\sum_{l=1}^{N}\mathcal{X}_{k,l} & \frac{4\pi a_r}{\lambda N_0}\sum_{k=1}^{M}\sum_{l=1}^{N}\mathcal{Y}_{k,l} & 0 & \frac{2MN}{N_0} \end{pmatrix} \qquad (5.31)$$

In Figure 5.5 the bounds and the MSE of the x and y estimates based upon the Maximum Likelihood estimation described in (5.6) are plotted. Note, that the ordinate is given in multiples of λ^2. The underlying scenario is the 9×9 system introduced in the previous section. The MSE is obtained from Monte Carlo simulations with 2000 iterations per SNR value. The empirical MSE and the theoretical bounds are in excellent agreement for high SNR values. For low SNR the classical *threshold* effect, well known in time of arrival and angle estimates, is observed. Further, it is observed that the precision of the x and y estimates differ. This is due to the geometry of the considered scenario and is discussed in the next section.

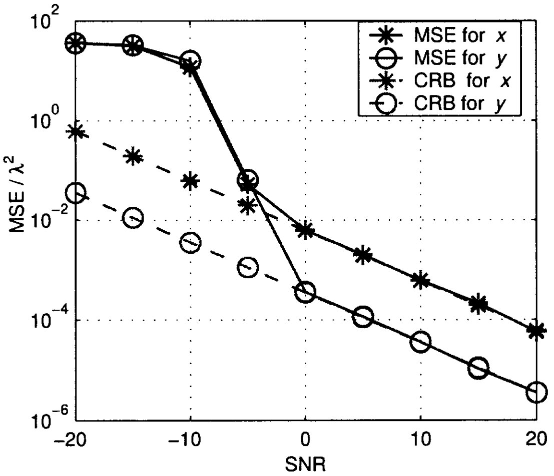

Figure 5.5 MSE of ML estimate and CRB for a 9×9 high resolution MIMO radar.

5.3 Ambiguity Function Revisited

In the previous section, it has been noted that the accuracy of the location estimate differs for the x and y coordinates due to the geometry of the scenario. Indeed, this observation is supported by the shape of the mainlobe of the ambiguity function. Figure 5.6 features an x and y cut of the ambiguity function shown in Figure 5.2. The dashed line represents the cut in x direction and the solid one the cut in y direction. The plots clearly show that the

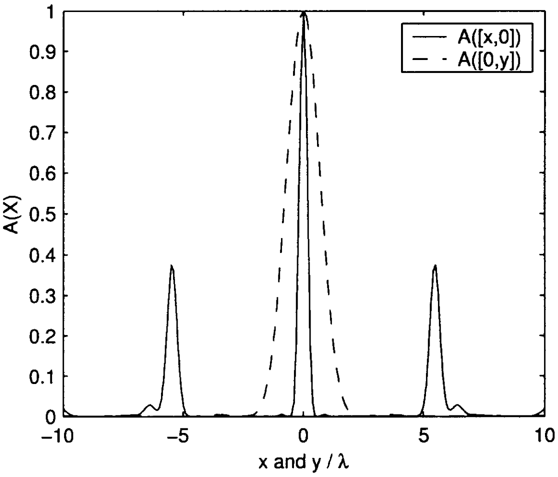

Figure 5.6 x and y cuts of the Ambiguity Function.

mainlobe is much more narrow in the y direction than in the x direction, allowing higher accuracy and resulting in a lower MSE for the y coordinate.

It is possible to derive some idea of the shape of the mainlobe by calculating the 3-dB width in the x and y directions of the ambiguity function. This is equivalent to solving $A([\Delta_x/2, 0]^T) = \frac{1}{2}$ and $A([0, \Delta_y/2]^T) = \frac{1}{2}$ for Δ_x and Δ_y, respectively, which is a rather tedious endeavor. Instead, some simple approximations based on geometric observations are used here. From here on it is assumed, without loss of generality, that the coordinate system is chosen in such a manner, that the x-axis separates the transmit–receive–aperture in two parts of the same size. Thus, the antenna elements are distributed over $[-\theta_{\max}, \theta_{\max}]$. For estimating the width of the mainlobe, the $\varphi_{s_k}(\tau)$ components in (5.8) can be ignored, as the discussion in Section 5.2 revealed that the bandwidth has a very limited impact. By representing the set of transmitter–receiver–pairs by two pairs, that together provide the highest accuracy in the considered direction, the mainlobe widths can be approximated. As the transmitter and receiver elements are handled in pairs and, thus, a pair the same angles towards the monitored area, $\theta_i^t = \theta_i^r$, we denote with θ_i the common angle of the i-th transmitter–receiver pair ($\theta_i^t = \theta_i^r = \theta_i$ $i = 1, 2$). The ambiguity function in x–direction only can be evaluated according to (5.7) and (5.2) as

$$\begin{aligned} &A([x,0]^T) \\ &= \frac{1}{16}\left|e^{\frac{j4\pi x}{\lambda}\cos\theta_1} + e^{\frac{j2\pi x}{\lambda}(\cos\theta_1+\cos\theta_2)} + e^{\frac{j4\pi x}{\lambda}\cos\theta_2}\right|^2 \\ &= \left|\cos\left(\frac{\pi x}{\lambda}\underbrace{(\cos\theta_1 - \cos\theta_2)}_{\text{I}}\right)\right|^4 . \end{aligned} \tag{5.32}$$

The width of the mainlobe can be minimized by maximizing the term denoted by I in (5.32). This is achieved by choosing $\theta_1 = 0$ and $\theta_2 = \theta_{\max}$, where θ_max is the largest possible angle of a sensor pair. Solving $A([\Delta_x/2, 0]^T) = \frac{1}{2}$ for Δ_x leads to

$$\Delta_x = \arccos\left(\frac{1}{\sqrt[4]{2}}\right)\frac{2\lambda}{\pi(1-\cos\theta_{\max})}. \tag{5.33}$$

$$\tag{5.34}$$

Similarly, the ambiguity function in y-direction only may be found as

$$A([0,y]^T) = \left|\cos\left(\frac{\pi y}{\lambda}(\sin\theta_1 - \sin\theta_2)\right)\right|^4 . \tag{5.35}$$

Minimizing the width leads here to $\theta_1 = \theta_{\max}$ and $\theta_2 = -\theta_{\max}$. Therefore, the width in y direction is found as

$$\Delta_y = \arccos\left(\frac{1}{\sqrt[4]{2}}\right)\frac{\lambda}{\pi\sin\theta_{\max}}. \tag{5.36}$$

For $\theta_{\max} = 45°$, these approximations are $\Delta_x = 1.24\lambda$ and $\Delta_y = 0.26\lambda$. The x and y cuts in Figure 5.2 are based on the 9×9 system described in Section 5.1 with elements spread over $[-45°, 45°]$. Apparently, the approximations fit the widths of the mainlobes in Figure 5.2 well. Further, the above introduced approximations imply that high resolution requires a large angular spread or, equivalently, a large $\theta_{\max}$. Finally, it can be noted that for small $\theta_{\max}$ one may expect the "sparse" system to behave as a regular array. Accordingly the width in y direction should relate to the conventional beamwidth Δ_ϕ. Let R denote the distance between the scatter and the array and D the size of the array. By using $\Delta_y = \Delta_\phi \cdot R$ and $\sin\theta_{max} = \frac{D}{2R}$, (5.36) leads to the well known relation $\Delta_\phi \simeq \frac{\lambda}{D}$, which further validates the above approximations.

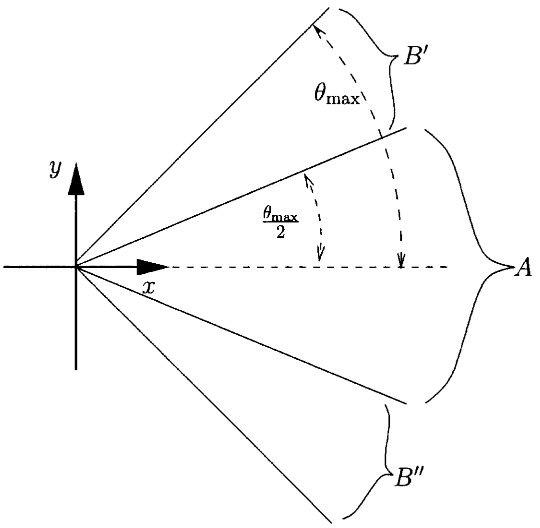

Figure 5.7 Explanation for the non–coherent 3-dB widths.

The discussion in the previous and current section established that the employed signal bandwidth has a very limited impact on the best possible accuracy at high SNR and the shape of the mainlobe. However, the bandwidth limits the amount of significant sidelobes the ambiguity function may feature. Note, that Figures 5.2 and 5.6 clearly show two significant sidelobes. Due to the extremely sparse nature of the proposed systems, very high sidelobes can occur if the bandwidth is chosen too small. The bandwidth of the signals effectively limits the area in which significant sidelobes can appear, as per the non–coherent ambiguity function given in (5.9) (see the example plotted in Figure 5.3) illustrated. The area, over which significant sidelobes may appear, can be approximated as, say, the 3dB width of the non–coherent ambiguity function's mainlobe. To derive an approximation of the width of the non–coherent mainlobe, it is noted first that the i-th non–coherent operating transmitter–receiver pair by itself has a squared sinc function as an individual ambiguity function in the θ_i direction, the direction from which the pair observes the monitored area). This is similar to a conventional non–coherent range estimation with a bandwidth Δf. The first zero of this ambiguity function due to the signal bandwidth is at $d_{\theta_i} = \frac{c}{2\Delta f}$ in the θ_i direction. Projecting the individual ambiguity function of the i-th transmitter–receiver pair on the x and y axis, respectively, leads to zeros located at $d_x(i) = \frac{c}{\Delta f 2 \cos\theta_i}$ and $d_y(i) = \frac{c}{2\Delta f \cos\theta_i}$ on the x and y axis. According to Figure 5.7, one finds that for evenly distributed transmitter and receiver pairs half of them are within the interval denoted as A and half of them within B' and B''. The ones within A feature ambiguity functions in x direction with zeros at $d_x(i) \leq \frac{c}{\Delta f \cos(\theta_{\max}/2)}$. Further, the pairs within B' and B'' feature ambiguity functions in y direction with zeros at $d_y(i) \leq \frac{c}{\Delta f \sin(\theta_{\max}/2)}$. Therefore, one can use the following rough approximations for the 3-dB widths

$$\Delta_x^{nc} = \frac{c}{\Delta f \cos\frac{\theta_{\max}}{2}}, \tag{5.37}$$

$$\text{and } \Delta_y^{nc} = \frac{c}{\Delta f \sin\frac{\theta_{\max}}{2}}, \tag{5.38}$$

as half of the individual ambiguity functions have a zero in the x direction before Δ_x^{nc} and the other half have a zero in the y direction before Δ_y^{nc}. It is noted, that these are rough approximations as bistatic pairs with $\theta_k^t \neq \theta_l^r$ are neglected.

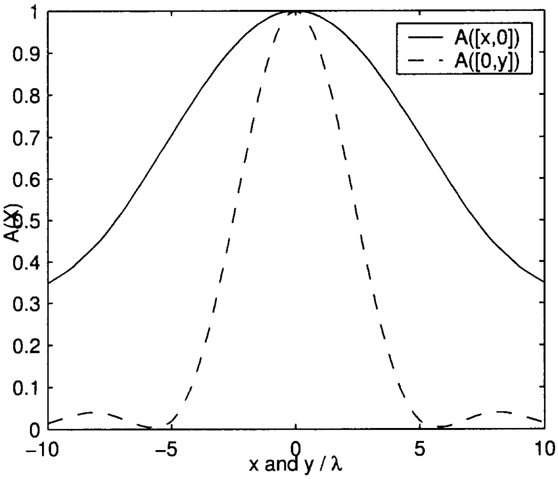

Figure 5.8 x and y cuts of the non–coherent Ambiguity Function.

For $\theta_{\max}$ and $\frac{\Delta f}{f_c} = 0.1$, this approximations are $\Delta_x^{nc} = 10.9\lambda$ and $\Delta_y^{nc} = 26.2\lambda$. Figure 5.8 shows the x and y cuts of the non–coherent ambiguity function of Figure

5.9 of 9×9 system described in Section 5.1. Again, the dashed line represents the cut in x direction and the solid one the cut in y direction. The approximations are indeed rather rough. However, they predict the ratio between the widths in x and y direction and also that the possible accuracy in the x-direction is better than the one in the y direction, which is in contrast to the coherent case. However, for the following considerations, the important observation is that the non–coherent mainlobe width is inversely proportional to the employed bandwidth, Δf.

As stated before, with the approximations in (5.38) the size of the area, in which significant sidelobes can appear, can be approximated as $\Delta_x^{nc} \cdot \Delta_y^{nc}$. Further, the size of the mainlobe and the sidelobes is given by Δ_x and Δ_y. This and some assumptions allow to incorporate the results of Steinberg et al., [47, 48] and, in particular, [49]. In the following, random transmitter and receiver locations are considered. The angles, at which elements can be located, are again limited to the $[-\theta_{\max}, \theta_{\max}]$ interval. It is assumed that the mainlobe widths of the coherent and non–coherent ambiguity function are not affected by the random element locations as long as this interval is kept constant. Further, it is assumed that the widths of the "coherent" sidelobes is similar to the ones of the "coherent" mainlobe. However, the magnitude of the sidelobes are random variables, e.g. [47]. A sidelobe of the ambiguity function, which is sufficiently separated from the coherent mainlobe ($|x| > \Delta_x/2$ and $|y| > \Delta_y/2$), but within the non–coherent mainlobe ($|x| < \Delta_x^{nc}/2$ and $|y| < \Delta_y^{nc}/2$), is considered. Within the non–coherent mainlobe the impact of the $\varphi_{s_k^b}(\tau)$ terms in (5.8) may be neglected. Thus, one can write for the ambiguity function

$$A(\vec{X}) = \frac{1}{M^2 N^2} \left| \underbrace{\sum_{k=1}^{M} \sum_{l=1}^{N} e^{-j 2\pi f_c \tau_{k,l}}}_{\mathrm{II}} \right|^2 . \tag{5.39}$$

For random transmitter and receiver locations and a sufficient number of transmitters and receivers, the term denoted as II is a complex Gaussian random variable with zero mean and variance $\frac{MN}{2}$ per complex dimension due to the central limit theorem, [49]. Accordingly, $A(\vec{X})$ is an exponential distributed random variable with the mean $E\{A(\vec{X})\} = \frac{1}{MN}$. The reader is remembered in this context, that the mainlobe of the coherent ambiguity function has a height of 1.

The realizations of $A(\vec{X})$ roughly decorrelate over distances bigger than Δ_x and Δ_y. In other words, the area of the non–coherent mainlobe is filled with sidelobes of the size $\Delta_x \cdot \Delta_y$. Accordingly one expects to find

$$n = c' \cdot \frac{\Delta_x^{nc}}{\Delta_x} \frac{\Delta_x^{nc}}{\Delta_x} = c'' \cdot \left(\frac{f_c}{\Delta f} \right)^2 \tag{5.40}$$

independent sidelobes within the non–coherent mainlobe. c' and c'' denote some constants, which are not of particular interest here. The number n is referred to as the "array parameter" in [49]. The magnitudes of these sidelobes are independent random variables with an exponential distribution according to the previous discussion. The probability p that all of these sidelobes are smaller than a given maximum value $A_{\max}$ is then found as

$$p = \left(1 - \exp\{-A_{\max} MN\}\right)^n . \tag{5.41}$$

Using $1 - p^{1/n} \simeq -\frac{1}{n} \ln p$ for $p^{1/n} \approx 1$, the equation (5.41) can be solved for $A_{\max}$ resulting in

$$A_{\max} = \frac{1}{MN} \left(\ln \left(c'' \left(\frac{f_c}{\Delta f} \right)^2 \right) - \ln \ln p^{-1} \right) . \tag{5.42}$$

Thus, with a given probability p all sidelobes, including the peak sidelobe, are smaller than $A_{\max}$.

It is noted that, as the height of the mainlobe is 1, the maximum sidelobe value is also the Peak Sidelobe Ratio (PSLR). Therefore, important conclusions can be derived from the analysis of the random element location scheme. First, increasing the ratio of signal bandwidth to carrier frequency reduces logarithmically the height of the peak sidelobe for a given p. Second, the product of the number of transmit and receive elements is inversely proportional to the PSLR. This reveals the important advantage of the MIMO approach compared to a possible Single Input Multiple Output (SIMO) approach, as the later would require $M \cdot N$ receive elements to achieve the same sidelobe statistics as the MIMO approach with M transmit and N receive elements. The beginning of this section linked the angular spread of the system with the width of the coherent mainlobe, which defines the location accuracy discussed in the previous section. The presented discussion is based on extrapolating the results of Steinberg et al. to a two dimensional position estimation problem. Further research is necessary to validate the description of the statistical properties of random ambiguity functions.

However, this section is concluded by illustrating the impact of the used signal bandwidth on the amount and height of potential sidelobes. Therefore, with the previously discussed 9×9 system with deterministic element positions is used as an example. Figure 5.9 features x and y cuts of the coherent and non–coherent ambiguity functions. The first ones are plotted as solid lines and the latter as dashed lines. Part (a) and (b) of the figure show again the ambiguity function for $\frac{\Delta f}{f_c} = 0.1$ similar to Figure 5.6 and 5.8. In contrast, parts (c) and (d) feature the cuts for $\frac{\Delta f}{f_c} = 0.01$. As expected the mainlobe width of the non–coherent ambiguity function increases by a factor of ten whereas the one of the coherent ambiguity function stays constant. However, the number and the height of significant sidelobes increases when reducing the signal bandwidth as the discussion in this section explained.

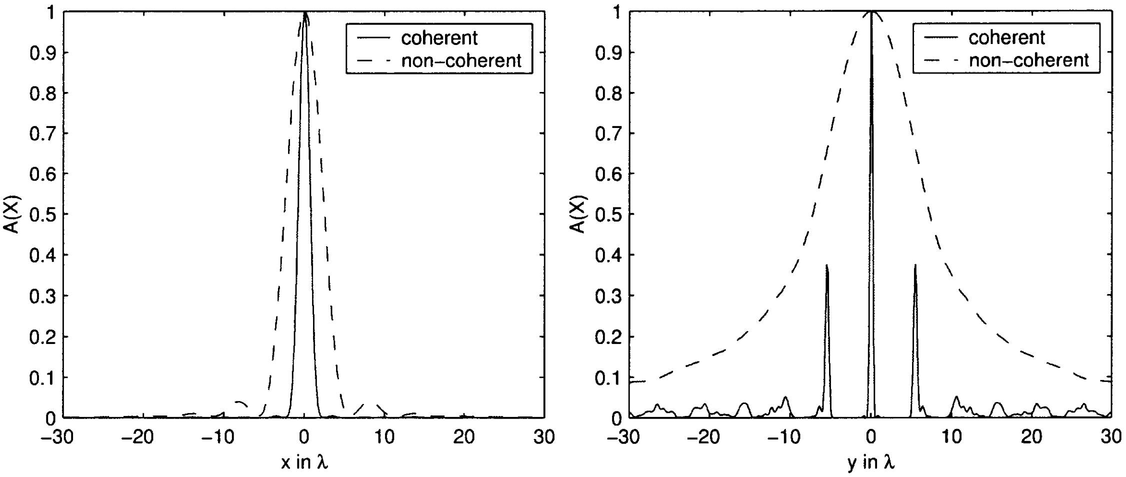

(a) x-cuts, $\Delta f/f_c = 0.1$ (b) y-cuts, $\Delta f/f_c = 0.1$

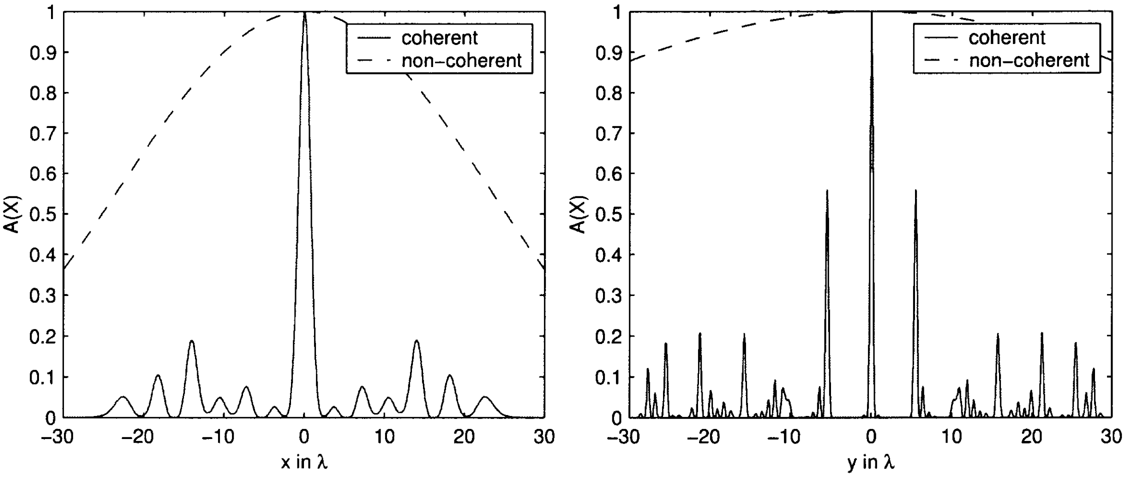

(c) x-cuts, $\Delta f/f_c = 0.01$ (d) y-cuts, $\Delta f/f_c = 0.01$

Figure 5.9 x and y cuts of the coherent and non–coherent ambiguity functions for different $\frac{\Delta f}{f_c}$ ratios.

CHAPTER 6

CONCLUSION AND FUTURE RESEARCH

In Chapter 2, it has been shown that tremendous gains can be achieved with transmit diversity in a direction finding scenario, as the diversity helps to overcome the target fluctuations. Average and outage Cramer Rao bounds have been developed and used to explore the diversity effects.

In Chapter 3, the MIMO radar approach has been compared to conventional phased array systems for target detection in white noise. It has been illustrated that MIMO radar systems still benefit from diversity even when the diversity branches are subject to different propagation attenuations. Further, the trade-offs between coherent and non-coherent processing, the first resulting in a coherent processing gain and the later in diversity, have been explored.

Both, Chapter 2 and 3, include simulation results for correlated target aspects. It has been illustrated that for moderate correlation coefficients between target the responses for each aspect and high SNR a MIMO with diversity still outperforms a conventional radar system. Both chapters reveal the great potential of MIMO systems enjoying diversity in radar.

In Chapter 4, the diversity discussion has been extended to include moving targets and clutter returns. It has been demonstrated that an arbitrary movement direction by itself impairs the detection performance of Doppler processing based phased array radar in a similar manner as the RCS fluctuations do. A spatial MIMO radar observing the target from several perspectives is not subject to this impairment. Further, the chapter analyzes the effect of the strictly joint processing across all sensors for a MIMO system by comparing it to what would commonly be treated as a multi–static system. Finally, an a adaptive MIMO moving target detector is introduced with a constant false alarm rate. This chapter has shown that the diversity enjoyed by a MIMO system is not only advantageous in respect to RCS fluctuations and thus provides further evidence for the MIMO radar superiority.

In Chapter 5, the MIMO radar discussion has been carried beyond diversity. For diversity in radar non–coherent processing is used. Assuming isotropic reflecting scatterers, the different phase shifts of the reflections across the system elements can be used in a coherent processing system to locate a single scatterer with very high accuracy or to resolve several scatterers. By the means of Cramer Rao bounds and 2-dimensional ambiguity functions, the high resolution capabilities of coherent MIMO radar have been illustrated. The effect of different system parameters such as a signal bandwidth is analyzed. The analysis of the high resolution capabilities gives raise to great expectations for the usage of MIMO systems in target recognition and similar applications.

Because of the significant diversity gains of MIMO radar in respect to fading targets or targets with arbitrary movement directions and its high resolution abilities, this dissertation concludes that MIMO systems have the potential to change the way radar is normally considered.

However, this dissertation can naturally only serve as an initial study. Many topics of future research can be found in the MIMO radar context and without attempting completeness several shall be mentioned briefly subsequently. The trade–offs between diversity and coherent processing gain as discussed in Chapter 3 should be explored in more detail. The reader should note in this context that Li et al. explore also in [12] systems which are referred to in this dissertation as hybrid systems. However, the degree at which diversity or coherent processing gains have to utilized is not discussed. Further, tracking systems that in MIMO radar can observe the true velocity vector and not only the radial component are a promising field of research. Moreover, MIMO radar with moving sensor platforms is a topic of great practical interest. Furthermore, more practical issues such as the synchronization and communication links between the system elements need to be addressed in the future.

APPENDIX A

DERIVATION OF THE CRB

Though derivations for the general angle of arrival estimation CRB can be found in [27] and [26], in this appendix the CRB is derived for the specific problem considered in Chapter 2. The textbook derivations are for general, multiple parameter estimation CRB and are rather involved.

The CRB for the parameter vector ψ is given by, [27]:

$$\mathrm{CRB}(\psi) = \mathbf{J}_{\mathrm{r}}(\psi)^{-1} = -E_{\mathrm{r}}\left\{\frac{\delta^2 \ln f(\mathbf{r}|\psi)}{\delta\psi\delta\psi^H}\right\}^{-1} \tag{A.1}$$

Where $\mathbf{J}(\psi)$ is the so called Fisher information matrix. In this appendix it is shown that the problem decouples. Let θ be the first element of ψ. Decoupling implies then that the $[1,1]$ element of $\mathbf{J}^{-1}$ is given as $\mathbf{J}_{1,1}^{-1} = \frac{1}{\mathbf{J}_{1,1}}$. The $[2,1]$ and $[3,1]$ elements of $\mathbf{J}$ have to be zero therefore. Here, it is first demonstrated that this is the case and then $\mathbf{J}_{1,1}$ is evaluated.

In the following the CRB for one snapshot is considered. Each snapshot received vector r is a N dimensional complex Gaussian variable. Therefore, the $[i,j]$ element of the corresponding Fisher matrix can be written as:

$$\mathbf{J}_{i,j} = E_{\mathrm{r}}\left\{\frac{\delta^2}{\delta\psi_i\delta\psi_j}\ln\pi^N\det\{\mathbf{C}_{\mathrm{r}}\}\right\} + E_{\mathrm{r}}\left\{\frac{\delta^2}{\delta\psi_i\delta\psi_j}\mathbf{r}^H\mathbf{C}_{\mathrm{r}}{}^{-1}\mathbf{r}\right\} \tag{A.2}$$

$\mathbf{C}_{\mathrm{r}}$ is the correlation matrix of the received vector. Based on the signal model defined in (2.19) and as mentioned in Section 2.2.1, the correlation is given by $\mathbf{C}_{\mathrm{r}} = (2M)^{-1}||\alpha||^2\mathbf{a}(\theta)\mathbf{a}^H(\theta) + 2\sigma^2 \cdot \mathbf{I}_N$. $\mathbf{a}(\theta)$ is the steering vector, as defined in Section 2.1. For conciseness, the received signal power, $(2M)^{-1}||\alpha||^2$, is denoted p_s in this derivation. The correlation matrix is then $\mathbf{C}_{\mathrm{r}} = p_s\mathbf{a}(\theta)\mathbf{a}^H(\theta) + 2\sigma^2 \cdot \mathbf{I}_N$.

The determinant of the correlation matrix can be evaluated by considering its eigenvalues. One eigenvector is $\mathbf{a}(\theta)$ and the corresponding eigenvalue is $p_s||\mathbf{a}(\theta)||^2 + 2\sigma^2$.

The other $N-1$ eigenvectors can be chosen as any set of pairwise mutual orthogonal vectors orthogonal to $\mathbf{a}(\theta)$. The corresponding eigenvalues are $2\sigma^2$. Thus, the determinant in (A.2) is $\det\{\mathbf{C_r}\} = (p_s\|\mathbf{a}(\theta)\|^2 + 2\sigma^2)\cdot(2\sigma^2)^{N-1}$. As $\|\mathbf{a}(\theta)\|^2$ is constantly N the determinant is independent of the value of θ. Therefore, the first summand in (A.2) is zero if either i or j is 1. To prepare for the evaluation of the second terms in (A.2) it necessary to note, that the inverse of the correlation matrix can be found with the matrix inversion lemma, e.g. [50]. Its derivatives in respect to θ can be evaluated accordingly [1]:

$$\begin{aligned}
\mathbf{C_r}^{-1} &= \frac{1}{2\sigma^2}\mathbf{I}_N - \frac{1}{2\sigma^2}\frac{\mathbf{a}(\theta)\mathbf{a}^H(\theta)}{\frac{2\sigma^2}{p_s} + \|\mathbf{a}(\theta)\|^2} \\
\frac{\delta}{\delta\theta}\mathbf{C_r}^{-1} &= -\frac{1}{2\sigma^2}\frac{\dot{\mathbf{a}}(\theta)\mathbf{a}^H(\theta) + \mathbf{a}(\theta)\dot{\mathbf{a}}^H(\theta)}{\frac{2\sigma^2}{p_s} + N} \\
\frac{\delta^2}{\delta\theta^2}\mathbf{C_r}^{-1} &= -\frac{1}{2\sigma^2}\frac{\ddot{\mathbf{a}}(\theta)\mathbf{a}^H(\theta) + 2\dot{\mathbf{a}}(\theta)\dot{\mathbf{a}}^H(\theta) + \mathbf{a}(\theta)\ddot{\mathbf{a}}^H(\theta)}{\frac{2\sigma^2}{p_s} + N}
\end{aligned} \tag{A.3}$$

The first derivative of $\mathbf{C_r}^{-1}$ in respect to θ is of the form $c\cdot\left(\dot{\mathbf{a}}\mathbf{a}^H + \mathbf{a}\dot{\mathbf{a}}^H\right)$ [2], where c is a scalar depending on p_s and σ^2. Thus, the $[2,1]$ and $[3,1]$ element of $\mathbf{J}$ can be found

$$\frac{\delta^2}{\delta\psi_i\delta\theta}\mathbf{C_r}^{-1} = c'\cdot(\dot{\mathbf{a}}\mathbf{a}^H + \mathbf{a}\dot{\mathbf{a}}^H), \tag{A.4}$$

where c' is another scalar given by $\frac{\delta}{\delta\psi_i}c$. Using the linearity of the expectation and trace operators allows to rewrite the second summand in (A.2) as[3]:

$$\begin{aligned}
E_\mathbf{r}\{\mathbf{r}^H\frac{\delta^2\mathbf{C_r}^{-1}}{\delta\psi_i\delta\theta}\mathbf{r}\} &= E_\mathbf{r}\{\mathrm{trace}\{\mathbf{r}^H\frac{\delta^2\mathbf{C_r}^{-1}}{\delta\psi_i\delta\theta}\mathbf{r}\}\} = E_\mathbf{r}\{\mathrm{trace}\{\frac{\delta^2\mathbf{C_r}^{-1}}{\delta\psi_i\delta\theta}\mathbf{r}\mathbf{r}^H\}\} \\
&= \mathrm{trace}\{\frac{\delta^2\mathbf{C_r}^{-1}}{\delta\psi_i\delta\theta}E_\mathbf{r}\{\mathbf{r}\mathbf{r}^H\}\} = \mathrm{trace}\{\frac{\delta^2\mathbf{C_r}^{-1}}{\delta\psi_i\delta\theta}\mathbf{C_r}\} \\
&= c'\cdot\left(p_s\cdot\left(\mathbf{a}^H\dot{\mathbf{a}}\mathbf{a}^H\mathbf{a} + \mathbf{a}^H\mathbf{a}\dot{\mathbf{a}}^H\mathbf{a}\right) + 2\sigma^2\cdot\left(\mathbf{a}^H\dot{\mathbf{a}} + \dot{\mathbf{a}}^H\mathbf{a}\right)\right)
\end{aligned} \tag{A.5}$$

To evaluate (A.5) the elements of the vector $\mathbf{a}$, which is specified in (2.4), and their derivatives with respect to θ are listed subsequently; the second derivative is needed in

---

[1] $\dot{\mathbf{a}}(\theta)$ denotes the derivative of $\mathbf{a}(\theta)$ in respect to θ.

[2] For conciseness, the explicit dependency of the vector $\mathbf{a}$ on θ is omitted.

[3] Equality $\mathrm{trace}\{\mathbf{AB}\} = \mathrm{trace}\{\mathbf{BA}\}$ is used in this evaluation, [51].

the later course of this derivation.

$$\begin{aligned}
[\mathbf{a}]_k &= e^{j\pi k \sin\theta} \\
[\dot{\mathbf{a}}]_k &= j\pi k \cos\theta e^{j\pi k \sin\theta} \\
[\ddot{\mathbf{a}}]_k &= (-\pi^2 k^2 \cos^2\theta - j\pi k \sin\theta) e^{j\pi k \sin\theta}
\end{aligned} \tag{A.6}$$

By evaluating (A.5) with the first and second expression of (A.6) it may be found that $E_{\mathbf{r}}\{\mathbf{r}^H \frac{\delta^2 \mathbf{C_r}^{-1}}{\delta \boldsymbol{\psi}_i \delta\theta} \mathbf{r}\}$ is zero for $i = 2, 3$, as $\mathbf{a}^H \dot{\mathbf{a}} + \dot{\mathbf{a}}^H \mathbf{a} = 0$. Thus, the problem decouples and it can be continued to evaluate the $[1, 1]$ element of $\mathbf{J}$. As stated before the derivative of the determinant of $\mathbf{C_r}$ in respect to θ is zero. Using the linearity of the expectation and trace operator similarly to (A.5) one can evaluate the second summand of (A.2) for $i, j = 1$:

$$E_{\mathbf{r}}\{\mathbf{r}^H \frac{\delta^2 \mathbf{C_r}^{-1}}{\delta\theta^2} \mathbf{r}\} = \mathrm{trace}\{\frac{\delta^2 \mathbf{C_r}^{-1}}{\delta\theta^2} \mathbf{C_r}\} \tag{A.7}$$

Using the last line of (A.3) in (A.7) one finds:

$$\begin{aligned}
\mathrm{trace}\{\frac{\delta^2 \mathbf{C_r}^{-1}}{\delta\theta^2} \mathbf{C_r}\} = -\frac{1}{2\sigma^2(\frac{2\sigma^2}{p_s} + N)} \Big(& p_s \big(\mathbf{a}^H \ddot{\mathbf{a}} \mathbf{a}^H \mathbf{a} + 2\mathbf{a}^H \dot{\mathbf{a}} \dot{\mathbf{a}}^H \mathbf{a} + \mathbf{a}^H \mathbf{a} \ddot{\mathbf{a}}^H \mathbf{a} \big) \\
& + 2\sigma^2 \big(\mathbf{a}^{\mathbf{H}} \ddot{\mathbf{a}} + 2\dot{\mathbf{a}}^H \dot{\mathbf{a}} + \ddot{\mathbf{a}}^H \mathbf{a} \big) \Big)
\end{aligned} \tag{A.8}$$

The two parts of (A.8) can be evaluated with the expressions given in (A.6):

$$\begin{aligned}
\mathbf{a}^H \ddot{\mathbf{a}} \mathbf{a}^H \mathbf{a} + \mathbf{a}^H \mathbf{a} \ddot{\mathbf{a}}^H \mathbf{a} + 2\mathbf{a}^H \dot{\mathbf{a}} \dot{\mathbf{a}}^H \mathbf{a} &= 2\pi^2 \cos^2\theta \left(-N \sum_{k=0}^{N-1} k^2 + \Big(\sum_{k=0}^{N-1} k \Big)^2 \right) \\
&= -\pi^2 \cos^2\theta \frac{(N^2 - 1)N^2}{6} \\
\mathbf{a}^{\mathbf{H}} \ddot{\mathbf{a}} + \ddot{\mathbf{a}}^H \mathbf{a} + 2\dot{\mathbf{a}}^H \dot{\mathbf{a}} &= 2 \left(-\pi^2 \cos^2\theta \sum_{k=0}^{N-1} k^2 + \pi^2 \cos^2\theta \sum_{k=0}^{N-1} k^2 \right) \\
&= 0
\end{aligned} \tag{A.9}$$

Thus, the $[1,1]$ element of the Fisher information matrix for a single snapshot is:

$$\begin{aligned}\mathbf{J}_{1,1} &= \operatorname{trace}\{\frac{\delta^2 \mathbf{C_r}^{-1}}{\delta\theta^2}\mathbf{C_r}\} \\ &= \frac{1}{2\sigma^2(\frac{2\sigma^2}{p_s}+N)}p_s\left(\pi^2\cos^2\theta\frac{(N^2-1)N^2}{6}\right)\end{aligned} \tag{A.10}$$

As the Fisher information of multiple snapshots is the sum of the single snapshot Fisher information and as the problem decouples, the $[1,1]$ element of the Cramer Rao Bound matrix, which is called $CRB(\theta|p_s)$, is found as:

$$CRB(\theta|p_s) = \frac{1}{L\cdot\mathbf{J}_{1,1}} = \frac{6}{L\pi^2\cos^2\theta(N^2-1)}\left(\left(\frac{2\sigma^2}{p_sN}\right)^2+\frac{2\sigma^2}{p_sN}\right) \tag{A.11}$$

Expressing the dependency on the fading coefficients given by $\boldsymbol{\alpha}$ explicitly by re-substituting the signal power p_s with $(2M)^{-1}||\boldsymbol{\alpha}||^2$, one finds:

$$\mathrm{CRB}(\theta|\boldsymbol{\alpha}) = \frac{6}{L\pi^2\cos^2\theta(N^2-1)}\left(\frac{2\sigma^2 2M}{N||\boldsymbol{\alpha}||^2}+\frac{(2\sigma^2)^2 4M^2}{N^2||\boldsymbol{\alpha}||^4}\right) \tag{A.12}$$

APPENDIX B

DERIVATION OF THE TEST STATISTIC

In this appendix the test statistic for non-equal pathlosses is developed. The pdf of the received signal under the H_1 hypothesis is given as:

$$
\begin{aligned}
f(\mathbf{r}|H_1) &= \int_{\boldsymbol{\alpha}} f(\mathbf{r}|\boldsymbol{\alpha}, H_1) f(\boldsymbol{\alpha}) d\boldsymbol{\alpha} \\
&= \int_{\boldsymbol{\alpha}} \frac{1}{(\pi\sigma^2)^{MN}} e^{-\frac{1}{\sigma^2}\left(\mathbf{r}-\sqrt{\frac{E}{M}}\mathbf{L}\boldsymbol{\alpha}\right)^H\left(\mathbf{r}-\sqrt{\frac{E}{M}}\mathbf{L}\boldsymbol{\alpha}\right)} \frac{1}{\pi^{MN}} e^{-|\boldsymbol{\alpha}|^2} d\boldsymbol{\alpha} \\
&= c \int_{\boldsymbol{\alpha}} e^{-\frac{1}{\sigma^2}|\mathbf{r}|^2+\frac{1}{\sigma^2}\sqrt{\frac{E}{M}}\boldsymbol{\alpha}^H\mathbf{L}^H\mathbf{r}+\frac{1}{\sigma^2}\sqrt{\frac{E}{M}}\mathbf{r}^H\mathbf{L}\boldsymbol{\alpha}-\frac{1}{\sigma^2}\frac{E}{M}\boldsymbol{\alpha}^H\mathbf{L}^H\mathbf{L}\boldsymbol{\alpha}-\boldsymbol{\alpha}^H\boldsymbol{\alpha}} d\boldsymbol{\alpha} \\
&= c e^{-\frac{1}{\sigma^2}|\mathbf{r}|^2} \int_{\boldsymbol{\alpha}} e^{-\boldsymbol{\alpha}^H\left(\frac{1}{\sigma^2}\frac{E}{M}\mathbf{L}^H\mathbf{L}+\mathbf{I}\right)\boldsymbol{\alpha}+\frac{1}{\sigma^2}\sqrt{\frac{E}{M}}\boldsymbol{\alpha}^H\mathbf{L}^H\mathbf{r}+\frac{1}{\sigma^2}\sqrt{\frac{E}{M}}\mathbf{r}^H\mathbf{L}\boldsymbol{\alpha}} d\boldsymbol{\alpha} \\
&= c e^{-\frac{1}{\sigma^2}|\mathbf{r}|^2} \int_{\boldsymbol{\alpha}} e^{-\boldsymbol{\alpha}^H\left(\frac{1}{\sigma^2}\frac{E}{M}\mathbf{L}^H\mathbf{L}+\mathbf{I}\right)\boldsymbol{\alpha}} \\
&\quad \cdot e^{\boldsymbol{\alpha}^H\left(\frac{1}{\sigma^2}\frac{E}{M}\mathbf{L}^H\mathbf{L}+\mathbf{I}\right)\left(\frac{1}{\sigma^2}\frac{E}{M}\mathbf{L}^H\mathbf{L}+\mathbf{I}\right)^{-1}\frac{1}{\sigma^2}\sqrt{\frac{E}{M}}\mathbf{L}^H\mathbf{r}+\frac{1}{\sigma^2}\sqrt{\frac{E}{M}}\mathbf{r}^H\mathbf{L}\left(\frac{1}{\sigma^2}\frac{E}{M}\mathbf{L}^H\mathbf{L}+\mathbf{I}\right)\left(\frac{1}{\sigma^2}\frac{E}{M}\mathbf{L}^H\mathbf{L}+\mathbf{I}\right)^{-1}\boldsymbol{\alpha}} \\
&\quad \cdot e^{-\frac{1}{\sigma^2}\sqrt{\frac{E}{M}}\mathbf{r}^H\mathbf{L}\left(\frac{1}{\sigma^2}\frac{E}{M}\mathbf{L}^H\mathbf{L}+\mathbf{I}\right)^{-1}\frac{1}{\sigma^2}\sqrt{\frac{E}{M}}\mathbf{L}^H\mathbf{r}+\frac{1}{\sigma^2}\sqrt{\frac{E}{M}}\mathbf{r}^H\mathbf{L}\left(\frac{1}{\sigma^2}\frac{E}{M}\mathbf{L}^H\mathbf{L}+\mathbf{I}\right)^{-1}\frac{1}{\sigma^2}\sqrt{\frac{E}{M}}\mathbf{L}^H\mathbf{r}} d\boldsymbol{\alpha} \\
&= c e^{-\frac{1}{\sigma^2}|\mathbf{r}|^2} \cdot e^{\frac{1}{\sigma^2}\sqrt{\frac{E}{M}}\mathbf{r}^H\mathbf{L}\left(\frac{1}{\sigma^2}\frac{E}{M}\mathbf{L}^H\mathbf{L}+\mathbf{I}\right)^{-1}\frac{1}{\sigma^2}\sqrt{\frac{E}{M}}\mathbf{L}^H\mathbf{r}} \\
&\quad \cdot \int_{\boldsymbol{\alpha}} e^{-\left(\boldsymbol{\alpha}-\left(\frac{1}{\sigma^2}\frac{E}{M}\mathbf{L}^H\mathbf{L}+\mathbf{I}\right)^{-1}\frac{1}{\sigma^2}\sqrt{\frac{E}{M}}\mathbf{L}^H\mathbf{r}\right)^H\left(\frac{1}{\sigma^2}\frac{E}{M}\mathbf{L}^H\mathbf{L}+\mathbf{I}\right)\left(\boldsymbol{\alpha}-\left(\frac{1}{\sigma^2}\frac{E}{M}\mathbf{L}^H\mathbf{L}+\mathbf{I}\right)^{-1}\frac{1}{\sigma^2}\sqrt{\frac{E}{M}}\mathbf{L}^H\mathbf{r}\right)} d\boldsymbol{\alpha} \\
&= c' e^{-\frac{1}{\sigma^2}|\mathbf{r}|^2} \cdot e^{\frac{1}{\sigma^4}\frac{E}{M}\mathbf{r}^H\mathbf{L}\left(\frac{1}{\sigma^2}\frac{E}{M}\mathbf{L}^H\mathbf{L}+\mathbf{I}\right)^{-1}\mathbf{L}^H\mathbf{r}} \qquad \text{(B.1)}
\end{aligned}
$$

The pdf of the received signal under H_0 hypothesis is given as:

$$
f(\mathbf{r}|H_0) = \frac{1}{(\pi\sigma^2)^{MN}} e^{-\frac{1}{\sigma^2}|\mathbf{r}|^2} \qquad \text{(B.2)}
$$

Evaluating the logarithmic likelihood ratio test the test statistic is found as

$$
\eta = \ln\frac{f(\mathbf{r}|H_1)}{f(\mathbf{r}|H_0)} = c'' \cdot \frac{1}{\sigma^4}\frac{E}{M}\mathbf{r}^H\mathbf{L}\left(\frac{1}{\sigma^2}\frac{E}{M}\mathbf{L}^H\mathbf{L}+\mathbf{I}\right)^{-1}\mathbf{L}^H\mathbf{r}. \qquad \text{(B.3)}
$$

Taking into account, that L is a real diagonal matrix, (3.5), and denoting with $L(i)$ its i-th diagonal element, the test statistic can be rewritten as

$$\eta = \sum_{i=0}^{MN-1} \frac{\frac{E}{M}\frac{1}{\sigma^4}L(i)^2}{1+\frac{E}{M}\frac{1}{\sigma^2}L(i)^2}|r(i)|^2 \underset{H_0}{\overset{H_1}{\gtrless}} \gamma. \tag{B.4}$$

APPENDIX C

CFAR PROPERTIES OF THE MIMO MTD

In this appendix, the CFAR properties of the MIMO moving target detector are explored. The way this is done is similar to [38]. The adaptive MIMO moving target detector decision statistic has the form

$$\xi = \max_{v_x,v_y} \sum_{k=1}^{M} \sum_{l=1}^{N} \frac{\left|\mathbf{d}^H_{k,l}(v_x,v_y)\hat{\mathbf{C}}^{-1}_{k,l}\mathbf{r}_{k,l}\right|^2}{\mathbf{d}^H_{k,l}(v_x,v_y)\hat{\mathbf{C}}^{-1}_{k,l}\mathbf{d}_{k,l}(v_x,v_y)} \underset{H_0}{\overset{H_1}{\gtrless}} \gamma, \tag{C.1}$$

where $\hat{\mathbf{C}}_{k,l}$ is an estimate of the covariance matrix of the clutter observed by the k,l transmitter–receiver–pair based on L secondary sample vectors. It is focused now on a single term of the sum in the test statistic. By substituting $\mathbf{d}_{k,l}(v_x,v_y)$ with $\mathbf{C}^{1/2}_{k,l}\mathbf{d}'_{k,l}(v_x,v_y)$ and $\mathbf{r}'_{k,l}$ with $\mathbf{C}^{1/2}_{k,l}\mathbf{r}'_{k,l}$ each term given as

$$\frac{\left|\mathbf{d}'^H_{k,l}(v_x,v_y)\mathbf{C}^{1/2}_{k,l}\hat{\mathbf{C}}^{-1}_{k,l}\mathbf{C}^{1/2}_{k,l}\mathbf{r}'_{k,l}\right|^2}{\mathbf{d}'^H_{k,l}(v_x,v_y)\mathbf{C}^{1/2}_{k,l}\hat{\mathbf{C}}^{-1}_{k,l}\mathbf{C}^{1/2}_{k,l}\mathbf{d}'_{k,l}(v_x,v_y)} = \frac{\left|\mathbf{d}'^H_{k,l}(v_x,v_y)\hat{\mathbf{C}}'^{-1}_{k,l}\mathbf{r}'_{k,l}\right|^2}{\mathbf{d}'^H_{k,l}(v_x,v_y)\hat{\mathbf{C}}'^{-1}_{k,l}\mathbf{d}'_{k,l}(v_x,v_y)}. \tag{C.2}$$

It is noted, that $\hat{\mathbf{C}}'_{k,l} = \mathbf{C}^{-1/2}_{k,l}\hat{\mathbf{C}}_{k,l}\mathbf{C}^{-1/2}_{k,l}$ follows a complex Wishart distribution, $\mathcal{CW}(L,K,\mathbf{I})$ with mean $\mathbf{I}$ and thus its distribution of the actual clutter covariance $\mathbf{C}$. Further, $\mathbf{r}'_{k,l}$ is under H_0 a complex Gaussian vector with zero mean and covariance matrix $\mathbf{I}$, $\mathcal{CN}(\mathbf{0},\mathbf{I})$. Moreover, for any $\mathbf{d}'_{k,l}(v_x,v_y)$ a unitary matrix $\mathbf{U}$ can be found that rotates it onto the first elementary vector, $c\mathbf{e} = \mathbf{U}^H\mathbf{d}'_{k,l}(v_x,v_y)$. With $\mathbf{r}''_{k,l} = \mathbf{U}^H\mathbf{r}'_{k,l}$ and $\hat{\mathbf{C}}''_{k,l} = \mathbf{U}^H\hat{\mathbf{C}}'_{k,l}\mathbf{U}$ expression (C.2) becomes

$$\frac{\left|c\mathbf{e}^H(v_x,v_y)\hat{\mathbf{C}}''^{-1}_{k,l}\mathbf{r}''_{k,l}\right|^2}{|c|^2\mathbf{e}^H\hat{\mathbf{C}}''^{-1}_{k,l}\mathbf{e}^H} = \frac{\left|\mathbf{e}^H(v_x,v_y)\hat{\mathbf{C}}''^{-1}_{k,l}\mathbf{r}''_{k,l}\right|^2}{\mathbf{e}^H\hat{\mathbf{C}}''^{-1}_{k,l}\mathbf{e}^H}. \tag{C.3}$$

Note, that $\mathbf{r}''_{k,l}$ and $\hat{\mathbf{C}}''_{k,l}$ follow the same distributions as $\mathbf{r}'_{k,l}$ and $\hat{\mathbf{C}}'_{k,l}$, respectively, and are thus independent on the actual $\mathbf{C}_{k,l}$. Therefore, the term in expression (C.3) is for any

v_x, v_y and any k, l independent from the respective $\mathbf{C}_{k,l}$. Then the double sum in respect to k and l over the terms in (C.2) or (C.3) for any v_x, v_y has to be independent of the eventual different $\mathbf{C}_{k,l}$. As the double sum is independent of $\mathbf{C}_{k,l}$ for *any* v_x, v_y, the maximum in respect to v_x and v_y is independent on the actual clutter covariance matrices for each transmitter–receiver–pair, $\mathbf{C}_{k,l}$, too. Accordingly, the decision statistic in (C.1) leads under H_0 to constant false alarm rates.

REFERENCES

[1] V. Tarokh, N. Seshadri, and A. Calderbank, "Space-time codes for high data rate wireless communication: Performance criterion and code construction," *IEEE Trans. on Info. Theory*, vol. 44, no. 2, pp. 744–765, March 1998.

[2] H. Bölcskei and A. J. Paulraj, *The Communications Handbook*, 2nd ed. CRC Press, 2002, ch. Multiple-input multiple-output (MIMO) wireless systems, pp. 90.1 – 90.14.

[3] G. J. Foschini and M. J. Gans, "On Limits of Wireless Communications in a Fading Environment When Using Multiple Antennas," *Wireless Personal Communications*, vol. 6, no. 3, pp. 311–318, March 1998.

[4] D. Tse and P. Viswanath, *Fundamentals of Wireless Communications*. Cambridge, UK: Cambridge University Press, 2005.

[5] M. Skolnik, *Introduction to Radar Systems*, 2nd ed. McGraw-Hill, 1980.

[6] N. Levanon, *Radar Principles*. John Wiley & Sons, 1988.

[7] E. Fishler, A. Haimovich, R. Blum, D. Chizhik, L. Cimini, and R. Valenzuela, "MIMO radar: An idea whose time has come," in *Proc. of the IEEE Int. Conf. on Radar*, April 2004.

[8] E. Fishler, A. H. Haimovich, R. S. Blum, L. Cimini, D. Chizhik, and R. Valenzuela, "Spatial diversity in radars - models and detection performance," *IEEE Trans. on Signal Processing*, vol. 54, no. 3, pp. 823–838, March 2006.

[9] D. Rabideau and P. Parker, "Ubiquitous MIMO multifunction digital array radar," in 37^{th} *Asilomar Conference on Signals, Systems and Computers*, November 2003.

[10] F. C. Robey, S. Coutts, D. Weikle, J. C. McHarg, and K. Cuomo, "MIMO radar theory and experimental results," in 38^{th} *Asilomar Conference on Signals, Systems and Computers*, November 2004, pp. 300–304.

[11] N. Lehman, E. Fishler, A. M. Haimovich, R. S. Blum, L. Cimini, and R. Valenzuela, "Evaluation of Transmit Diversity in MIMO-radar Direction Finding," *accepted by IEEE Trans. on Signal Processing*, 2006.

[12] J. Li and L. Xu, "Iterative Generalized Likelihood Ratio Test (iGLRT) for MIMO Radar," *IEEE Transactions on Signal Processing (accepted)*, 2006.

[13] V. S. Chernyak, *Fundamentals of Multisite Radar Systems*, 1st ed. Gordon and Breach Science Publishers, 1998.

[14] C. B. I. Papoutsis and H. Griffiths, "Fundamental Performance Limitations of Radar Networks," in *Proc. of the* 1^{st} *EMRS DTC Technincal Conference, Edingburgh*, 2004.

[15] L. Mozzone, S. Bongi, and F. Filocca, “Diversity in multistatic active sonar,” in *Riding the Crest into the* 21^{st} *Century, OCEANS ’99, IEEE/MTS*, September 1999.

[16] T. Johnsen, K. Olsen, S. Johnsrud, and S. R., “Simultaneous use of multiple pseudo random noise codes in multistatic CW radar,” in *Proc. of the IEEE Int. Conf. on Radar*, April 2004.

[17] T. A. Seliga and F. J. Coyne, “Multistatic radar as a means of dealing with the detection of multipath false targets by airport surface detection equipment radars,” in *Proc. of the IEEE Int. Conf. on Radar*, May 2003.

[18] A. Dogandzic and A. Nehorai, “Cramer-Rrao bounds for estimating range, velocity, and direction with an active array,” *IEEE Transaction on Signal Processing*, vol. 49, no. 6, pp. 1122–1137, June 2001.

[19] S. Pasupathy and A. N. Venetsanopoulos, “Optimum active array processing structure and space-time factorability,” *IEEE Trans. Aerosp. Electron. Syst.*, vol. 10, pp. 770–778, 1974.

[20] L. Swindelehurst and P. Stoica, “Maximum likelihood methods in radar array signal processing,” *Proc. of the IEEE*, vol. 86, no. 2, pp. 421–441, Feb. 1998.

[21] S. Haykin, J. Litva, and T. J. Shepherd, *Radar Array Processing*, 1st ed. New York: Springer - Verlag, 1993.

[22] J. Ward, “Cramer-Rao bounds for target angle and Doppler estimation with space-time adaptive processing radar,” in *Proc.* 29^{th} *Asilomar Conf. Signals, Syst. Comput.*, Nov. 1995, pp. 1198–1202.

[23] F. Gesbert, H. B. D. A. Gore, and A. J. Paulraj, “Outdoor MIMO wireless channels: Models and Performance Prediction,” *IEEE Trans. on Commun.*, vol. 50, no. 12, pp. 1926–1934, December 2002.

[24] P. E. Howland, “Target tracking using television-based bistatic radar,” *IEE Proc., Radar Sonar Navig.*, vol. 146, no. 3, pp. 166–174, June 1999.

[25] ——, “Passive Tracking of Airborne Targets using only Doppler and DOA Information,” *IEE Colloquium on Alg. for Target Tracking*, pp. 37–39, May 1995.

[26] P. Stoica, E. G. Larsson, and A. B. Gershman, “The Stochastic CRB for Array Processing: Textbook Derivation,” *IEEE Signal Processing Letters*, vol. 8, no. 5, pp. 148–150, May 2001.

[27] H. L. V. Trees, *Optimum Array Processing*, 1st ed. John Wiley, 2003.

[28] A. Papoulis, *Probability, Random Variables and Stochastic Processes*, 3rd ed. Mc Graw Hill, 1991.

[29] R. S. Blum, L. Cimini, and A. H. Haimovich, “MIMO-Radar: Part 1 – Concepts and Applications,” *IEEE Signal Processing Magazine (in preparation)*, 2006.

[30] F. Gini, A. Farina, and M. Greco, "Selected list of references on radar signal processing," *IEEE International Radar Conference*, vol. 37, no. 1, pp. 329–259, January 2001.

[31] A. R. E. Fuste and A. P. Broquetas-Ibars, "Constant False Alarm Rate for a Radar Data Fusion Center with N Parallel Distributed Cell Averaging Receivers," *IEEE International Radar Conference*, pp. 507–510, May 1990.

[32] W. Liu, Y. Lu, and J. S. Fu, "A novel method for CFAR data fusion," *Neural Networks for Signal Processing, IEEE Signal Processing Society Workshop*, vol. 2, pp. 711–720, December 2000.

[33] T. Tsao, M. Slamani, P. Varshney, D. Weiner, H. Schwarzlander, and S. Borek, "Ambiguity Function for a Bistatic Radar," *IEEE Transactions on Aerospace and Electronic Systems*, vol. 33, no. 3, pp. 1041–1051, July 1997.

[34] G. L. Stüber, *Principles of Mobile Communications*, 1st ed. Kluwer Academic Publishers, 1996.

[35] F. E. Nathanson, *Radar Design Principles*, 2nd ed. McGraw-Hill, 1990.

[36] S. M. Kay, *Fundamentals of Statistical Signal Processing: Detection Theory*, 1st ed. Prentice Hall PTR, 1993, vol. 2.

[37] W. L. Melvin, "A STAP Overview," *IEEE Aerospace and Electronic Systems Magazine*, vol. 19, no. 1, January 2004.

[38] E. J. K. Frank C. Robey, Daniel R. Fuhrman and R. Nitzberg, "A CFAR Adaptive Matched Filter Detector," *IEEE Trans. on Aerospace and Electronic Systems*, vol. 28, no. 1, January 1992.

[39] M. Barkat and P. K. Varshney, "Decentralized CFAR Signal Detection," *IEEE Transactions on Aerospace and Electronic Systems*, vol. 25, no. 2, pp. 141–149, March 1989.

[40] R. Srinivasan, "Designing distributed detection systems," *IEE Proceedings-F, Radar and Signal Processing*, vol. 140, no. 3, pp. 191–197, June 1993.

[41] R. Viswanathan and P.K.Varshney, "Distributed Detection with Multiple Sensors: Part I – Fundamentals," *Proceedings of the IEEE,*, vol. 85, no. 1, pp. 54–63, January 1997.

[42] R. S. Blum, S. A. Kassam, and H. Poor, "Distributed Detection with Multiple Sensors: Part II – Advanced Topics," *Proceedings of the IEEE,*, vol. 85, no. 1, pp. 64–79, January 1997.

[43] D. R. Kirk, J. S. Bergin, P. M. Techau, and J. E. Don Carlos, "Multi-Static Coherent Sparse Aperture Approach to Precision Target Detection and Engagement," *IEEE International Radar Conference*, pp. 579–584, May 2005.

[44] J. E. Don Carlos, D. R. Kirk, J. S. Bergin, P. M. Techau, and J. D. Halsey, "Detecting system having a coherent sparse aperture," U.S. Patent 6,724,340, April 20, 2004.

[45] S. M. Kay, *Fundamentals of Statistical Signal Processing: Estimation Theory*, 1st ed. Prentice Hall PTR, 1993, vol. 1.

[46] Y. Qi, H. Kobayashi, and H. Suda, "Analysis of Wireless geolocation in a Non-Line-of-Sight Environment," *IEEE Trans. on Wireless Communications*, vol. 5, no. 3, pp. 672–681, March 2006.

[47] B. D. Steinberg and E. H. Attia, "Sidelobe Reduction of Random Arrays by Element Position and Frequency Diversity," *IEEE Transactions on Antennas and Propagation*, vol. AP-31, no. 6, pp. 922–930, November 1983.

[48] B. D. Steinberg, *Principles of aperture and array system design.* John Wiley & Sons, 1976.

[49] ——, "The Peak Sidelobe of the Phased Array Having Randomly Located Elements," *IEEE Transactions on Antennas and Propagation*, vol. AP-20, no. 2, pp. 129–136, March 1972.

[50] S. Haykin, *Adaptive Filter Theory*, 4th ed. Prentice Hall, 2002.

[51] J. N. Franklin, *Matrix Theory*. Mineola, NY: Dover Publications Inc., 2000.